STRONG CORRELATIONS AND TOPOLOGICAL ORDER IN ONE-DIMENSIONAL SYSTEMS

BY

WADE WELLS DE GOTTARDI

DISSERTATION

Submitted in partial fulfillment of the requirements
for the degree of Doctor of Philosophy in Physics
in the Graduate College of the
University of Illinois at Urbana-Champaign, 2012

Urbana, Illinois

Doctoral Committee:

Professor Nadya Mason, Chair
Professor Smitha Vishveshwara, Director of Research
Professor José Mestre
Professor Mike Stone

Abstract

This thesis presents theoretical studies of strongly correlated systems as well as topologically ordered systems in 1D. Non-Fermi liquid behavior characteristic of interacting 1D electron systems is investigated with an emphasis on experimentally relevant setups and observables. The existence of end Majorana fermions in a 1D p-wave superconductor subject to periodic, incommensurate and disordered potentials is studied.

The Tomonaga-Luttinger liquid (TLL), a model of interacting electrons in one spatial dimension, is considered in the context of two systems of experimental interest. First, a study of the electronic properties of single-walled armchair carbon nanotubes in the presence of transverse electric and magnetic fields is presented. As a result of their effect on the band structure and electron wave functions, fields alter the nature of the (effective) Coulomb interaction in tubes. In particular, it is found that fields couple to nanotube bands (or valleys), a quantum degree of freedom inherited from the underlying graphene lattice. As revealed by a detailed TLL calculation, it is predicted that fields induce electrons to disperse into their spin, band, and charge components. Fields also provide a means of tuning the shell-filling behavior associated with short tubes.

The phenomenon of charge fractionalization is investigated in a one-dimensional ring. TLL theory predicts that momentum-resolved electrons injected into the ring will fractionalize into clockwise- and counterclockwise-moving quasiparticles. As a complement to transport measurements in quantum wires connected to leads, non-invasive measures involving the magnetic field profiles around the ring are proposed.

Topological aspects of 1D p-wave superconductors are explored. The intimate connection

between non-trivial topology (fermions) and spontaneous symmetry breaking (spins) in one-dimension is investigated. Building on this connection, a spin ladder system endowed with vortex degrees of freedom is proposed in order to study the effects that inhomogeneous potentials have on the topological phase diagram. Periodic vortex patterns yield a rich parameter space for tuning into a topologically non-trivial phase. This analysis hinges on the development of a topological invariant based on the wave function of Majorana fermions which inhabit the ends of the system and are robust to disorder. The method is generalized to aperiodic and disordered potentials. The topological phase diagram of such systems is studied; numerical and analytic results are found to be in close agreement.

To Mom, Quinn, and the memory of my Dad.

Acknowledgments

Grad school represents a long deferred dream. Getting to this point took the love, support, and patience of a great number of friends and family.

First, I would like to thank my family. In particular, thanks go to my Mom. Her unwavering support and her emphasis on education made all this possible. Sharing grad school war stories with my sister Quinn (who is about to complete her own Ph.D.) has been critical in helping me stay sane when the going got tough. I would also like to thank John and Dian who have made Gonzales my home away from home.

There are many friends that I must thank – for the friendship, laughter, and mixed drinks. In particular, it's a pleasure to thank fellow grad students Sarang Gopalakrishnan, Tomoki Ozawa, Philip Powell, Stephanie Law, John Nichol, Jitong Yu, Xianhao Xin, Ry Ely, Jeremy and Jenny McMinis (Jenny holds honorary grad student status). Special thanks to my academic siblings Keui Sun and Qinglei Meng. They are great officemates, collaborators, and friends.

The physics department here in Urbana has to be one of the friendliest places on earth and I would like to thank the following members of the faculty and staff for their great teaching, warm mentoring, and endless assistance: Mike Stone, Nadya Mason, José Mestre, Gordon Baym, Philip Phillips, Paul Goldbart, John Stack, Wendy Wimmer, Becky McDuffee, Sue Lynn Herdle, and Mel Schweighart. I would also like to thank Matthew Grayson at Northwestern for all our live and electronic discussions.

As the old saying goes, it takes a village to raise a grad student. I am extremely thankful for having had the following mentors who took a great deal of effort to train me. Additionally,

it must be said that as a result of our collaborations, much of their own work appears in this thesis. Thanks to Tzu-Chieh Wei who worked very closely with me in the summer of 2007 on the carbon nanotube project. It's a pleasure to thank Siddhartha Lal who was extremely giving of his time while he was postdoc here in Urbana. From these two friends I learned a great deal about how to extract a physical picture from all the math. It is such a pleasure to acknowledge my dear friend Diptiman Sen. Diptiman was my host while I was a visitor at the Indian Institute of Science Bangalore in the summer of 2011. This trip was certainly a highlight of my time in graduate school. I'm so thankful for the energy and hospitality that he showed me while I was there.

Grad school has been the best and most productive time of my life. The one person in particular who has made this success possible is my advisor, Smitha Vishveshwara. I have been the beneficiary of Smitha's warmth, patience, and energy for the last five years. She has taught me how to think physically and communicate clearly and moreover, this instruction and mentoring always seemed to be her first priority. Smitha has also made me feel like a part of her family. For that, and for all that she has done for me, I will always be thankful.

Table of Contents

List of Abbreviations

TLL	Tomonaga-Luttinger liquid
SWNT	single-walled carbon nanotube
RG	renormalization group
T-DOS	tunneling density of states
S-C sep.	spin-charge separation
RHS	right-hand side
LHS	left-hand side
IQHE	integer quantum Hall effect
FQHE	fractional quantum Hall effect
RG	renormalization group
SQUID	superconducting quantum interference device
CWLM	weak continuous linear measurement
CW	clockwise
CCW	counterclockwise
TI	topological invariant

Chapter 1

Introduction

This thesis explores aspects of the collective behavior exhibited by one-dimensional electronic systems. The interplay between strong correlations and reduced dimensionality has a profound impact: these systems exhibit behavior not ascribable to individual electrons which compose them. The systems and phenomena investigated include field-effects in metallic carbon nanotubes, charge fractionalization in mesoscopic rings, and topological phase transitions in p-wave superconductors. Despite the apparent diversity of the systems considered, each provides a direct manifestation of strongly-correlated physics: they exhibit modes or quasiparticles which are not in one-to-one correspondence with individual electrons.

Tomonaga-Luttinger liquid

The Tomonaga-Luttinger liquid (TLL) is a model of 1D fermions interacting via a short-range potential. This model predicts a variety of phenomena which represent spectacular demonstrations of the collectivization which takes place in 1D. Two such phenomena – *spin-charge separation* and *charge fractionalization* – will be investigated in this thesis.

Luttinger liquids exhibit properties which depend continuously on the strength of the interactions, a fact intimately related to the inability of 1D systems to order. In the language of the renormalization group (RG), TLLs are described by a line of fixed points. This non-universal behavior suggests that a TLL with tunable parameters would represent a powerful tool for probing a wide range of physics. This was the primary motivation for our study of transverse field effects in single-walled carbon nanotubes (SWNT). Given that ultra-clean nanotubes are readily synthesized, they make ideal candidates for such a study. Fields

alter the group velocity of electrons propagating down the tube. By virtue of their effect on the circumferential electronic wave functions, fields fundamentally alter the nature of the effective 1D interactions in the system. Specifically, we find that the simultaneous application of electric and magnetic fields gives rise to different Fermi velocities for left- and right-movers. SWNT are endowed with an additional conducting channel which derives from the lattice plus basis structure of the underlying honeycomb lattice. Fields generate a coupling between this band degree of freedom and the charge sector, giving rise to three distinct plasmon velocities. These velocities are a signal that fields extend the phenomenon of charge-spin separation to the band degree of freedom. The tuning of these interactions has a profound effect on the relative dominance between spin density and charge density wave ordering. Additionally, we find that fields allow for exquisite control over the shell-filling structure of quantum dots formed from isolated short tubes.

Like spin-charge separation, charge fractionalization offers a window on the strong correlations of the TLL. Although there are several instances in which TLLs are predicted to exhibit fractionally charged quasiparticles, of interest here is the theoretical prediction that a right-moving electron injected into a TLL will give rise to right- and left-moving fractionally charged quasiparticles. One of the practical and conceptual challenges in testing this prediction is the fact that any transport measurement is necessarily an electron-in-electron-out experiment. In other words, the fractionalization process is convolved with the extraction of electrons from the fractionally charged quasiparticles which inhabit the TLL.

Given this challenge, we consider a geometry in which the fractionally charged quasiparticles are never extracted from the TLL: a mesoscopic ring. The challenge now is to probe the effects of fractionalization in a non-invasive way. A natural candidate is the magnetic field measured at points proximate to the ring. For example, we find that the induced power in a pickup loop can yield quantitative signatures of fractionalization. These measurements also provide a means of distinguishing fractionalization from single-particle phenomena which can mimic certain aspects of fractionalization, such as quantum superpositions or probabilistic

tunneling into the ring.

1D p-wave superconductor

Although the integer quantum Hall effect (IQHE) has been understood as a topological phenomena for two decades [1], the variety of topologically ordered materials predicted theoretically in the last five years has revolutionized condensed matter physics [2]. Kitaev's model of a 1D p-wave superconductor plays a central role in this thesis. This model possesses a topologically non-trivial phase which hosts end Majorana fermions. Notably, a Majorana fermion is its own antiparticle. Given that spatially separated Majoranas may share quantum information robust to decoherence, they have attracted a great deal of attention for potential quantum computation applications [3]. The well-established connection between 1D fermionic systems and spin chains motivates us to consider how topological order is manifest in the language of spin physics. We establish a direct connection between the presence of isolated Majorana modes (in the fermionic system) and spontaneous breaking (in the spin system).

Given the abstract nature of topological phases, model building represents an important theoretical approach to their study. A celebrated example is Kitaev's honeycomb model. We considered a spin-ladder system which, conceived to be a 1D version of the honeycomb model, maps to a 1D p-wave superconductor. This 'Kitaev ladder' is notable in that it possesses a $\mathbb{Z}_2$-vortex degree of freedom at each plaquette. In fermionic language, this vortex encodes the sign of an on-site chemical potential. Periodic patterns of vortices display a rich and diverse set of conditions for non-trivial topology. The uniform case, the subject of almost all previous work on the subject, is found to display vis-à-vis other periodic sectors an unusual phase diagram in that it is independent of the superconducting pairing strength. In contrast, the sector in which the vortex degree of freedom alternates in sign exhibits a topological phase as long as there is a critical amount of superconductivity pairing and non-zero hopping.

The study of the interplay between topology and periodic potentials sets the stage for

a more general investigation of the topology of inhomogeneous 1D systems. Such a study is timely; a theoretical proposal [4] has recently been experimentally realized and claims of an apparent detection of a Majorana mode have garnered a great deal of attention [5]. It is crucial that theory address non-ideal aspects encountered in an experimental setting. Given that isolated Majorana fermions necessarily live at (or near) zero energy, it is natural to expect that their properties (and even existence) may be particularly sensitive to disorder. Previous theoretical and numerical work has been primarily limited to slowly-varying and weak disorder.

This thesis explores disorder beyond this regime. Kitaev's model of a 1D p-wave superconductor subject to a disordered (on-site, à la the Anderson model [6]) chemical potential is explored. It is found that disorder qualitatively changes the topological phase diagram; this is not surprising considering the diversity of behavior exhibited by various periodic potentials. The keystone of our theoretical work is a direct link between the zero energy localization length of the normal state and the superconducting pairing strength required to drive the system into a topological phase. This link allows the leveraging of the considerable scholarship on 1D disordered systems to the problem at hand. This gives a good theoretical understanding of the phase diagram of various types of disorder, features which are well confirmed by numerical simulation. The physical picture which this mathematical analysis provides is revealing; the topological phase diagrams of disordered systems reflect the competition between disorder and superconducting pairing. The former tends to localize a Dirac fermionic state while the latter tends to spatially separate the state into its constituent Majoranas.

Organization of thesis

The organization of this thesis is as follows. Chapter 2 presents a theoretical introduction to degenerate 1D Fermi systems, focusing on non-Fermi liquid behavior predicted by the TLL model. In Chapter 3, a detailed band structure calculation of field-dependent effects

in SWNTs is derived. Using this field-dependent band structure as input, a TLL model is constructed in Chapter 4 which reveals a rich range of field-tunable TLL physics. Chapter 5 is a presentation of our analysis of charge fractionalization in a ring geometry. Chapter 6 provides a segue to studies of topological superconducting order in 1D systems with a focus on connections to spin physics. In Chapter 7 we study topological aspects of a spin ladder system and its vortex degrees of freedom. Chapter 8 extends the analysis of the previous chapter to p-wave superconductors subject to incommensurate and disordered potentials.

Chapter 2

Degenerate 1D Fermi systems

This chapter provides an introduction to the Tomonaga-Luttinger model (TLL). This model describes electrons constrained to move in 1D. One-dimensional fermionic systems are pathological in the sense that Landau's widely applicable Fermi liquid theory fails to apply. Fermi liquid theory is an extremely robust theory of interacting electrons in three dimensions [7]. Landau's theory explains why certain strongly interacting electron fluids are well described by models based on a non-interacting electron gas. Landau's essential idea was to imagine that interactions are 'turned on' adiabatically. The system evolves from a state involving non-interacting electrons to one composed of weakly interacting *quasiparticles* which, by definition, describe the fundamental excitations of the system. Roughly, these quasiparticles are electrons dressed by *local* distortions of electronic density. This screening renders the quasiparticles weakly interacting. Thus, many of the features of the noninteracting gas will persist in the interacting case.

As suggested by classical intuition, the restriction of particle motion to one dimension dramatically alters the character of many-body effects. The motion of a particle in 1D requires the 'cooperation' of its neighbors: the assumption of individual electron behavior breaks down. Such collectivization suggests that the these excitations will bear little resemblance to an individual electron [8]. The idea of describing the excitations in a one-dimensional electron system by plasma oscillations was first introduced by Tomonaga and was subsequently refined by Luttinger [9]. Though the model that we currently refer to as the TLL was first codified by Luttinger, it was Mattis-Lieb who corrected a subtle error in Luttinger's approach and first solved the model [10]. It is one of a small set of field theories

which admits an exact solution.

This chapter is organized as follows. Quantum degenerate gases in several (2.1) dimensions and one (2.2) dimension are examined. In 2.3, a formal description of the TLL is presented. The method of bosonization is then described in 2.4. Experimental signatures of the TLL model are then discussed in 2.5. Finally, a summary and outlook is presented in 2.6.

2.1 Quantum Degenerate gases and Landau Fermi Liquid Theory

Perhaps the greatest triumph of quantum theory is the connection it forges between the spin of an individual particle and the statistics obeyed by a collection of such particles. Fermions, particles with half-integer spin (i.e., $\frac{1}{2}\hbar, \frac{3}{2}\hbar, ...$), are described by a many-body wavefunction Ψ which is anti-symmetric under the interchange of any two identical fermions. The Pauli exclusion principle, which states that no two electrons may occupy the same quantum mechanical state, immediately follows from this antisymmetry. If two electrons did occupy the same quantum mechanical state, antisymmetry requires $\Psi = -\Psi$, and thus $\Psi = 0$. This result is of profound significance; it is the central organizing principle in atomic, nuclear, and condensed matter systems.

For cases in which the number of accessible states is much greater than the number of particles, the restriction offered by the Pauli principle does not dramatically alter the thermodynamic properties of the system. In cases in which the number of accessible states is comparable to the number of particles, however, the (so-called) degeneracy effects can be dramatic. What is the condition for a system to be degenerate? Consider a gas (in 3D) of N weakly interacting particles of mass m at a temperature T. A counting of the accessible

states yields the condition for degeneracy

$$\left(\frac{N}{V}\right)^{1/3} \gtrsim \frac{h}{\sqrt{2\pi m k_B T}}, \tag{2.1}$$

where V is the volume of the system [11]. This condition may also be read a different way. Analogous to the breakdown of geometric optics, quantum corrections to classical mechanics begin to play a role when the interparticle spacing becomes smaller than the thermal de Broglie wavelength. At room temperature $T \sim 300$ K, the thermal de Broglie wavelength of an electron is approximately 4.3 nm. Thus, if we consider a material in which each atom contributes one (essentially) free electron (with typical atoms being separated by 1 or 2 Å from each other), then the electrons will be strongly degenerate.

In the limit of extreme degeneracy, the electrons fill states up to a particular energy (known as the Fermi energy, E_F). Low energy excitations of the system are dominated by excitations near the surface of this 'Fermi sea'. In the presence of interactions, electrons will scatter into different unoccupied states. We might expect that this Fermi sea description will be useful only if the strength of the interactions is in some sense small. But consider the alkali metal potassium. Back of the envelope estimates of the average kinetic and Coulomb energies per particle yields $E_{pot}/E_{kin} \approx 3/2$[1]. Here, the potential energy *exceeds* the kinetic energy. Yet, there is excellent evidence that lithium is well described by an independent electron approximation, as revealed by Shubnikov-de Hass oscillations (which show a nearly nearly spherical Fermi surface).

How can we understand the robustness of the Fermi liquid picture? A modern renormalization group (RG) analysis provides the most complete theoretical understanding of such behavior [12]. However, the crucial role that the exclusion principle plays can be seen from the following argument which is at the heart of Landau's Fermi liquid theory [7]. Consider an electron with crystal momentum $\mathbf{k}$ and energy $\xi_{\mathbf{k}} = E(\mathbf{k}) - E_F$. Suppose that this elec-

[1]This approximation is obtained as follows. Potassium has $r_s = 3.25$ [10] (r_s is defined implicitly by $4\pi r_s^3 N/3V = 1$). In terms of r_s, $E_{kin}/N = 2.21/r_s^2$ Ry whereas $E_{coul} \sim e^2/r_e \sim 1/r_s$ Ry.

tron and another electron which is at or below the Fermi surface scatter into states $\mathbf{p}$ and $\mathbf{p}'$. Conservation of energy requires that $\xi_{\mathbf{p}} + \xi_{\mathbf{p}'} \leq \xi_{\mathbf{k}}$ whereas Pauli exclusion dictates that $\xi_{\mathbf{p}} + \xi_{\mathbf{p}'} > 0$ (since all states with $\xi < 0$ are filled). Such phase space considerations lead us to conclude that the scattering rate should go as $\Gamma_{\mathbf{k}} \sim \xi_{\mathbf{k}}^2$ and thus vanishes as we approach the Fermi surface [7]. In this context, the Heisenberg uncertainty principle $\Delta E \Delta t > \hbar$ suggests that a state is well-defined as long as $\Gamma_{\mathbf{k}} \ll \xi_{\mathbf{k}}/\hbar$, a condition met by particles which are close enough to the Fermi surface. The longevity of quasiparticles 'protects' the existence of the Fermi surface and ultimately is the central justification of Fermi liquid theory [13].

2.2 Electrons in 1D: Schrödinger + Pauli ≈ Dirac

We now turn to the fate of interacting fermions in 1D. A one-dimensional description is appropriate for any system in which the cost of exciting transverse modes is much greater than that required to excite longitudinal modes: the transverse modes are effectively 'frozen out'. This description is relevant to a wide variety of physical situations (Table 2.1 gives a list of several 1D systems). Of interest here are systems in which geometric confinement (as in the case of carbon nanotubes) engenders effectively 1D behavior.

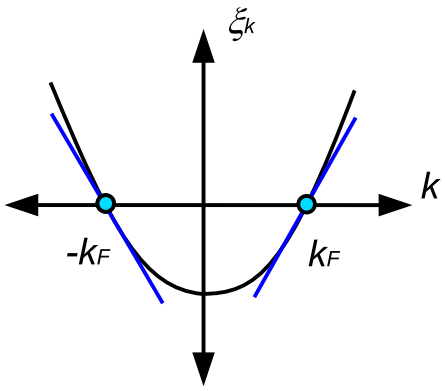

Figure 2.1: Linearization of 1D dispersion, as given in Eq. 2.2.

For concreteness, consider a large number of identical fermions confined to a 1D system

of length L. The kinetic energy of an electron of momentum p and mass m is described by a dispersion of the form $E(p) = p^2/2m$. The tight-binding predicts that for a lattice with spacing a, the dispersion is $E(k) = -2t \cos ka$ (where $k = p/\hbar$ is the crystal momentum and t is the hopping integral) [10]. We imagine adding fermions to the system one by one, up to momenta $k = \pm k_F$. The Fermi momentum k_F is related to the number density of fermions ($\rho = k_F/\pi$ for 'spinless' electrons). In contrast to the 2D and 3D cases, 1D fermionic systems have a Fermi 'surface' consisting of two points (known as Dirac points). Near these points, the dispersion takes the approximate form

$$\xi_{\mathbf{k}} = E(k) - E_F \approx r\hbar v_F \left(k - rk_F\right) + \mathcal{O}(k^2), \tag{2.2}$$

where $v_F = \frac{1}{\hbar}\partial E/\partial k$ is the Fermi velocity and the index r denotes right-moving ($r = R, +$) or left-moving ($r = L, -$) electrons. This linearization is depicted in Fig. 2.1. This is the dispersion of ultra-relativistic or massless particles, a feature which arises as a many-body effect; i.e., due to the existence of the Fermi sea. As shown in Appendix B, this is the dispersion of the massless Dirac equation.

We saw in the previous section that Pauli exclusion protects the existence of the Fermi surface. Dimensionality played a crucial role in this argument. In 1D, for an electron moving in a given direction, its energy uniquely specifies its momentum; this gives rise to a scattering rate $\Gamma_{\mathbf{k}} \sim \xi_{\mathbf{k}}$ [14]. Thus, as we approach the Fermi surface, the lifetime of the state increases more slowly than in higher dimensions. This may not seem too bad, however matters are even worse when this calculation is extended to higher order. It is found that the so-called self-energy receives a singular contribution. This singularity, known in quantum electrodynamics as the infra-red catastrophe, occurs because of the 'locking' between energy and momentum in 1D [14].

A natural question arises: what are the long-lived excitations in 1D? A clue is provided by returning to the scattering example of the previous section. There, it was found that the

Table 2.1: Examples of systems predicted to exhibit TLL behavior.

System	Features	Reference
FQHE edge state	chiral	[16]
QSH edge states	helical	[17]
cold atomic traps	neutral atoms	[18]
polaritons	coupled photons/matter	[19]
carbon nanotubes	Fermi point degree of freedom	[20]
spin-orbit split wire	'spiral'	[21, 22]

scattering of an excited electron was always accompanied by the creation of a particle-hole pair. For the case of 1D *intra*-branch scattering, it's clear that the generated particle-hole pair travel at approximately the same speed and, by virtue of the Coulomb attraction, are closely bound. This rough argument may be made more precise by considering density-density correlation functions [15]. In 1D this quantity possesses well defined poles, a clear indication that particle-hole excitations (plasmons) are stable excitations of the system.

2.3 Tomonaga-Luttinger liquid

The TLL model describes electrons in 1D interacting via a short-range potential. As shown in Table 2.1, the TLL model has been applied to a wide variety of systems. In this section and the next, we focus on the case of a spinless TLL. The spinful case will be discussed in 2.5. The model is rendered solvable by taking the dispersion to be exactly linear [8]: the kinetic energy takes the form

$$H_0 = -i\hbar v_F \int dx \left(\psi_R^\dagger \partial_x \psi_R - \psi_L^\dagger \partial_x \psi_L \right), \tag{2.3}$$

where the operator $\psi_r(x)$ annihilates a r-moving electron at point x. This Hamiltonian can be derived from the Dirac Lagrangian (see Appendix B)[2]. The quantity $\rho(x) = \sum_{r=\pm} \rho_r(x)$

[2]In what follows, we will generally set $\hbar = 1$.

is the (dimensionless) charge density at x, where $\rho_r = \psi_r^\dagger \psi_r$. Similarly, $j = \sum_r r\rho_r$ is the dimensionless current.

We now consider interactions of the form $V(x)$ with Fourier transform $\tilde{V}(q)$. Specifically,

$$\begin{aligned} H_{int} &= \frac{1}{2}\int dqdkdk' \ \psi^\dagger(k-q)\psi^\dagger(k'+q)\tilde{V}(q)\psi(k')\psi(k), \\ &= \frac{1}{2}\int dx \left[2g_2\rho_R(x)\rho_L(x) + g_4\left(\rho_R(x)^2 + \rho_L(x)^2\right)\right], \end{aligned} \tag{2.4}$$

where $g_2 = \tilde{V}(0) - \tilde{V}(2k_F)$ and $g_4 = \tilde{V}(0)$ [23]. For the case in which $\tilde{V}(0)$ dominates, this expression reduces to

$$H_{int} = \frac{\tilde{V}(0)}{2}\int dx \left(\rho_R(x) + \rho_L(x)\right)^2. \tag{2.5}$$

A bare Coulomb interaction has 'infinite range'; this is manifest as a logarithmic divergence of $\tilde{V}(k)$ as $k \to 0$ [8]. For the physical systems considered in this thesis, it is appropriate to invoke a long-distance cutoff $k \sim 1/L$, where L is the length of the system. We will thus take $V \equiv \tilde{V}(0) \approx \tilde{V}(k \approx 1/L)$ (see Chapter 4). However, this assumption must be carefully considered for a given experimental setup; the gating of the system may render the screening length to be much less than L [24].

2.4 Bosonization

Bosonization is a mapping between fermions and bosons. The magic of the method is that (certain four fermion) interactions become quadratic in the bosonic language. Although other methods for solving the TLL exist [8], bosonization has a number of extra perquisites; for example, it provides a straightforward means of calculating the scaling dimension of any fermionic operator.

The mapping between bosons and fermions takes the form of the celebrated Jordan-

Table 2.2: Dictionary relating fermionic and bosonic operators in 1D [9, 8]

Fermions	Bosons
$\psi_r(x)$	$\psi_r = \frac{1}{\sqrt{2\pi a}}\eta_r e^{irk_F x}e^{i\sqrt{\pi}\varphi_r}$
$\psi_R^\dagger\psi_R$	$\frac{1}{\sqrt{2\pi}}\partial_x\varphi_R$
$\psi_L^\dagger\psi_L$	$-\frac{1}{\sqrt{2\pi}}\partial_x\varphi_L$
$\psi_R^\dagger\psi_L + \psi_L^\dagger\psi_R$	$\frac{1}{\pi a}\cos\left(\sqrt{\pi}\theta\right)$

Wigner transformation

$$\psi_r = \frac{1}{\sqrt{2\pi a}}\eta_r e^{irk_F x}e^{i\sqrt{\pi}\varphi_r}, \tag{2.6}$$

where a is a short-distance cutoff of the theory and the chiral bosonic fields φ_r satisfy the algebra

$$[\varphi_r(x), \varphi_{r'}(x')] = -i\pi r\delta_{rr'}\mathrm{sgn}(x - x'). \tag{2.7}$$

The operator η_r is known as a Klein factor [8, 9, 10]. It is a ladder operator which acts on the (fermionic) Fock space (i.e., $\eta_+^\dagger|n_+, n_-\rangle = |n_+ + 1, n_-\rangle$) and also enforces anticommutation between the $r = +, -$ sectors (see Eq. 4.8). The $n_\pm$ are the number of excess electrons residing at each of the Fermi points $k = \pm k_F$ (see below). The bosonization identity may be derived via highly non-trivial but direct manipulations of the operators [9]. Here we will verify that for special cases, the correlation functions obtained in either the fermionic or bosonic representation are the same. Table 2.2 is a dictionary relating fermionic operators to their bosonic counterparts.

Before demonstrating this connection, we give the bosonic Hamiltonian. It is convenient to introduce achiral bosonic fields θ, ϕ where $\varphi_r = r\theta - \phi$. The bosonization prescription reveals the bosonic equivalent of Eq. 2.3 to be

$$\begin{aligned} H_0 &= \frac{v_F}{4}\int dx\left[(\partial_x\varphi_R)^2 + (\partial_x\varphi_L)^2\right], \\ &= \frac{v_F}{2}\int dx\left[(\partial_x\theta)^2 + (\partial_x\phi)^2\right]. \end{aligned} \tag{2.8}$$

From Table 2.2, we have

$$\rho_r = \frac{k_F}{2\pi} + \frac{1}{\sqrt{2\pi}} r \partial_x \varphi_r \tag{2.9}$$

and thus Eq. 2.5 becomes

$$H_{int} = V \int dx\ \rho(x)^2 = \frac{V}{\pi} \int dx\, (\partial_x \theta)^2 \,. \tag{2.10}$$

Remarkably, the 4-fermion interaction becomes quadratic in bosonic language. It is customary to combine H_0 and H_{int} giving

$$H_{TLL} = H_0 + H_{int} = \frac{u}{2} \int dx \left[\left(\partial_x \tilde{\theta} \right)^2 + \left(\partial_x \tilde{\phi} \right)^2 \right], \tag{2.11}$$

where we have made the transformation $\tilde{\theta} = \theta/\sqrt{g}$, $\tilde{\phi} = \sqrt{g}\phi$, with $g = 1/\sqrt{1 + 2V/\pi v_F}$ and $u = v_F/g$. This transformation preserves the commutation relations obeyed by θ and ϕ. Notably, the Hamiltonian remains free but (repulsive) interactions tend to 'stiffen' the bosonic modes.

2.4.1 Correlation Functions

Correlation functions represent the primary means of connecting a theory to its experimental predictions. The correlation functions given here will be used at several points in this thesis. Additionally, correlation functions provide a straightforward means of confirming the bosonization approach. We begin by recalling that the free fermions described by H_0 have correlation functions

$$\mathcal{G}_r(x,t) = \langle T \psi_r(x,t) \psi^\dagger_{r'}(0,0) \rangle = \frac{1}{2\pi} \frac{1}{x - r v_F t} \delta_{rr'}, \tag{2.12}$$

where T is the time ordering operator. This correlation function stems directly from the elegant mathematical relation

$$\partial_z \left(\frac{1}{\bar{z}}\right) = \partial_{\bar{z}} \left(\frac{1}{z}\right) = 2\pi\delta^2(x,y), \tag{2.13}$$

where $z = x + iv_F t$, $\bar{z} = x - iv_F t$, and $\delta^2(x,y)$ is the 2D delta function.

We should also obtain the same expression in the bosonic language. Using Eq. 2.6, we have

$$\langle T\psi_r(x,t)\psi^\dagger_{r'}(0,0)\rangle = \frac{1}{2\pi a}\langle e^{i\varphi_r(x,t)} e^{i\varphi_r(0,0)}\rangle. \tag{2.14}$$

The correlation function for chiral bosons has the form

$$\langle T\varphi_r(x,t)\varphi_r(0,0)\rangle = \frac{1}{2\pi}\ln\left[(x - rv_F t)^2 + a^2\right], \tag{2.15}$$

where a is a short distance cutoff of the theory. Taken together with the identity $\langle e^{i\phi}\rangle = e^{-\frac{1}{2}\langle\phi\rangle^2}$ valid for free Gaussian fields, these expressions reproduce Eq. 2.12 for $a \to 0$.

We now turn to the calculation of correlation functions in the interacting theory. A very convenient way to derive these is to write H_{TLL} in terms of the chiral fields φ_r. This gives

$$H_{TLL} = \frac{u}{8}\int dx \left[\left(g + \frac{1}{g} + 2\right)\left((\partial_x\varphi_R)^2 + (\partial_x\varphi_L)^2\right) + 2\left(g + \frac{1}{g} - 2\right)\partial_x\varphi_R\partial_x\varphi_L\right]. \tag{2.16}$$

This Hamiltonian may be diagonalized by a Bogoliubov transformation

$$\begin{pmatrix} \tilde{\varphi}_+ \\ \tilde{\varphi}_- \end{pmatrix} = \begin{pmatrix} \cosh u & \sinh u \\ \sinh u & \cosh u \end{pmatrix} \begin{pmatrix} \varphi_+ \\ \varphi_- \end{pmatrix}, \tag{2.17}$$

which preserves the commutation relations of the chiral bosons (Eq. 2.7). The cross terms disappear if

$$\tanh 2u = \frac{g - \frac{1}{g}}{g + \frac{1}{g}}. \tag{2.18}$$

This gives $\cosh u = \frac{1}{2}\left(\frac{1}{\sqrt{g}} + \sqrt{g}\right)$ and $\sinh u = \frac{1}{2}\left(\frac{1}{\sqrt{g}} - \sqrt{g}\right)$. Thus, we find

$$\mathcal{G}(x,t) = \langle T\psi_{R\sigma}(x,t)\psi^{\dagger}_{R\sigma}(0,0)\rangle \sim \left(\frac{1}{x-ut}\right)^{\frac{1}{4}(g+1/g+2)} \left(\frac{1}{x+ut}\right)^{\frac{1}{4}(g+1/g-2)}. \tag{2.19}$$

This quantity shows that in the TLL there is not a one-to-one correspondence between electrons and quasiparticles. Physically, right- and left-moving electrons are coupled and thus are not free degrees of freedom. A right-moving electron decays into right- and left-moving quasiparticles, a phenomenon known as *charge fractionalization* (see Fig. 2.2).

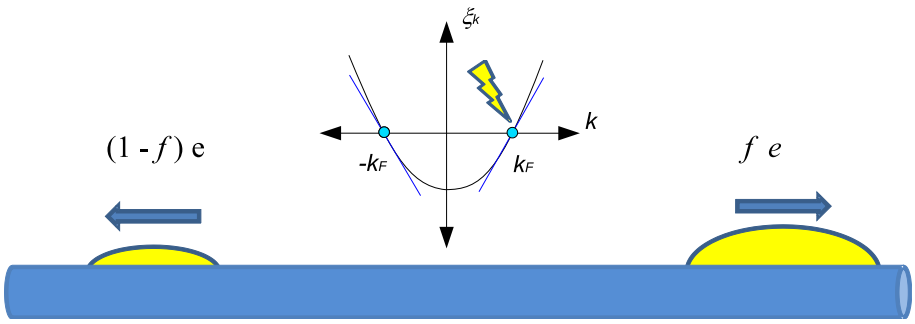

Figure 2.2: Charge fractionalization in a quantum wire. A right-moving electron decays into right- and left-moving quasiparticles of charge fe and $(1-f)e$, respectively. TLL theory predicts that $f = \frac{1+g}{2}$.

2.4.2 Finite Size Effects

We now address the properties of a TLL of finite size. To this end, we expand θ and ϕ in terms of zero and non-zero modes. The zero modes track boundary conditions and the number of excess electrons residing at each Fermi point (i.e., $n_{\pm}$), while the non-zero modes encode quasiparticle dynamics. Decomposing $\theta = \theta^0 + \bar{\theta}$ and $\phi = \phi^0 + \bar{\phi}$, we take the zero modes to be of the form

$$\begin{aligned} \theta^0(x) &= \theta_J + \sqrt{\pi}\,(N - N_0)\,x/L, \\ \phi^0(x) &= \phi_N + \sqrt{\pi} J x/L, \end{aligned} \tag{2.20}$$

where $[\theta_J, J] = [\phi_N, N] = i$. The mode expansion for the non-zero modes is given by

$$\begin{aligned}\bar{\theta}(x) &= \sum_{k\neq 0} \left|\frac{1}{2Lk}\right|^{1/2} e^{ikx}\left(b_k^\dagger + b_{-k}\right) \\ \bar{\phi}(x) &= \sum_{k\neq 0} \left|\frac{1}{2Lk}\right|^{1/2} \mathrm{sgn}(k) e^{ikx}\left(b_k^\dagger - b_{-k}\right).\end{aligned} \tag{2.21}$$

It is straightforward to show that the nonzero modes obey the commutation relations

$$\left[\partial_x \bar{\theta}(x), \bar{\phi}(x')\right] = i\delta_p(x-x') - \frac{i}{L}, \tag{2.22}$$

provided that the bosonic fields b_k obey the standard commutation relations

$$\left[b_k^\dagger, b_{k'}\right] = \delta_{kk'}. \tag{2.23}$$

In terms of the zero and non-zero modes, Eq. 2.11 becomes

$$H = \frac{\pi\hbar u}{2L}\left[\frac{1}{g}\left(N - N_0\right)^2 + gJ^2\right] + \hbar u \sum_{k\neq 0} |k| b_k^\dagger b_k. \tag{2.24}$$

For quantum wires with a no-current condition at the ends, $J = 0$. Non-zero J may arise in the context of persistent currents in rings (see Chapter 5).

The correlation functions in a finite size system are sensitive to the boundary conditions. In a ring geometry (described by periodic boundary conditions), we have

$$\mathcal{G}(x,t) \sim \left(\sin \pi \frac{x-ut}{L}\right)^{-\frac{1}{4}(g+1/g)^2} \left(\sin \pi \frac{x+ut}{L}\right)^{-\frac{1}{4}(g-1/g)^2}. \tag{2.25}$$

This expression is obtained by employing Eqs. 2.6, 2.21, 2.24 and the time ordered Green's functions for individual bosonic modes (see [25] for an explicit derivation).

2.4.3 Further Examples of fermionic-bosonic correspondence

Before proceeding, we give two more instances of the correspondence between the fermionic and bosonic descriptions.

In order for bosonization to make sense, there must be a one-to-one mapping between the states of the fermionic and bosonic Hilbert spaces. Here, we adapt more general techniques to demonstrate this mapping for a simple case (cf. [9]). In the non-interacting limit, the single-particle energy spacing for the fermionic system has the form $E = \pi\hbar v_F/L$, as derived in 3.5. The number of excited states of energy NE are, in accordance with the Pauli principle, given by the number of partitions $p(N)$ of the whole number N. This is the number of ways of writing N as $\lambda_1 + \lambda_2 + ...$ with $\lambda_1 \geq \lambda_2 \geq ...$). For example, for $N = 3$, $p(3) = 3$ since we can write $3 = 3$, $3 = 2 + 1$, and $3 = 1 + 1 + 1$.

The corresponding excitations in the bosonic system are given by the $k \neq 0$ terms of Eq. 2.24. The number of excited states of energy NE is given by the number of solutions of $N = 1 \times n_1 + 2 \times n_2 + ...$, where n_k is the occupation number of the k^{th} bosonic mode. Since any partition of N is uniquely specified by the number of times a given number appears in the sum, it immediately follows that the multiplicities of states for the fermionic and bosonic cases are equal. More formally, the equivalence of the Hilbert spaces may be seen by computing the partition functions in each language [9]. The proof of equivalence hinges on the identity

$$\sum_{n\geq 0} p(n)q^n = \prod_{k\geq 1} \frac{1}{(1-q^k)}, \tag{2.26}$$

where the LHS and RHS of this equation are the fermionic and bosonic partition functions, respectively [26].

As a second example, we show that the term $\frac{m}{\pi a}\cos\sqrt{\pi}\theta$ reproduces the correlation functions for a massive fermion in the limit $m \gg 1$. The $\cos\sqrt{\pi}\theta$ term tends to localize θ into one of the minima of the cosine which occur at $\theta = n\pi$, n odd. For $m \gg 1$, $\theta(x)$ must

be localized very near one such minima. Thus, we may replace

$$\frac{m}{\pi a}\cos\left(\sqrt{\pi}\theta\right) \to \frac{m}{2a}\theta^2, \tag{2.27}$$

where we have taken $\theta \to \theta - 1/\sqrt{\pi}$ and ignored an irrelevant constant. Using Eq. B.23 derived in Appendix B and Eq. 2.6, this suggests that for $m \to \infty$

$$\langle \psi_R(z_2)\psi_R^\dagger(z_1)\rangle \sim \frac{1}{\sqrt{|z|}} e^{-m|z_{12}|}, \tag{2.28}$$

where $z_{12} = |z_2 - z_1|$. In fermionic language, the system is free. Eq. B.13 gives

$$\langle \psi_R(z)\psi_R^\dagger(0)\rangle = -\frac{1}{\pi}\partial_z K_0(m|z_{12}|). \tag{2.29}$$

From Eq. 9.7.2 of [27], we have for $z \gg 1$

$$K_0(z) \sim \sqrt{\frac{\pi}{2z}} e^{-z}. \tag{2.30}$$

Combining Eqs. 2.29 and 2.30 gives a correlation function with the same asymptotic behavior as Eq. 2.28.

2.4.4 Spinful TLL

Inclusion of the spin sector is more naturally handled using non-Abelian bosonization [15], however, for the density-density interactions considered here Abelian bosonization suffices. Spin may be handled by the introduction of an index $\sigma = \uparrow\ (+), \downarrow\ (-)$; i.e., $\psi_r \to \psi_{r\sigma}$ and $\varphi_r \to \varphi_{r\sigma}$. Reintroducing the achiral fields,

$$\varphi_{r\sigma} = \frac{1}{\sqrt{2}}\left(\phi_s + \sigma\phi_s + r\theta_c + r\sigma\theta_s\right) \tag{2.31}$$

Table 2.3: Experimental systems displaying TLL behavior. Characteristic features of the system are given. Experimental claims of TLL phenomena (from the given references) are denoted by Frac. (electron fractionalization), S-C sep. (spin-charge separation), and T-DOS (tunneling density of states).

System	Features	Experiment	TLL parameter g	References
quantum wires	engineered device	Frac.	variable	[28]
Au chains	self-organized	T-DOS	0.26	[29]
1D $SrCuO_2$	cuprate material	S-C sep.	0.3-0.5	[30]
SWNTs	Dirac point index	T-DOS	0.2-0.3	[20]
FQHE edges	chiral	T-DOS	$0.25 - 1$	[31]

we obtain in direct analogy with the steps leading to Eq. 2.11

$$H_{TLL\sigma} = \sum_{a=c/s} \frac{u_a}{2} \int dx \left[\left(\partial_x \tilde{\theta}_a \right)^2 + \left(\partial_x \tilde{\phi}_a \right)^2 \right], \tag{2.32}$$

where c (s) denotes the charge (spin) sectors, with $u_a = v_F/g_a$. Since the interactions reside only in the charge sector (Eq. 2.5), $g_s = 1$. The spinful version of Eq. 2.19 is

$$\mathcal{G}(x,t) \equiv \langle T\psi_{R\sigma}(x,t)\psi^\dagger_{R\sigma}(0,0)\rangle \sim \prod_{a=\rho/\sigma} \left(\frac{1}{x - u_a t} \right)^{\frac{1}{4}(g_a + 1/g_a)^2} \left(\frac{1}{x + u_a t} \right)^{\frac{1}{4}(g_a - 1/g_a)^2}, \tag{2.33}$$

Clearly, the form of Eq. 2.33 signals a dramatic failure of Fermi liquid theory. Quasiparticles of a 1D electron system are not in one-to-one correspondence with the electrons of the free theory.

2.5 Luttinger liquid phenomenology

We now discuss a few of the TLL phenomena which have been observed experimentally. Table 2.3 provides a short list of experimental systems which exhibit TLL behavior. By virtue of the fact that $u_c \neq u_s$, spin and charge excitations propagate at different speeds. Aspects of spin-charge separation have been observed in experiments on quantum wires [32]

and photoemission studies of 1D copper-oxide chains [30]. These experiments probe the spectral density and reveal two propagating channels characterized by different speeds. The ratio of these speeds is g in the TLL framework, and can be corroborated by theoretical estimates or independent measures of g based on the tunneling density of states (see below). While these experiments provide excellent evidence for spin-charge separation, they should not be regarded as observations of this phenomena. In particular, these experiments do not address the *identity* of the propagating modes; i.e., the identification of the modes as charge- and spin- is a hypothesis based on theory.

Charge fractionalization is also manifest in Eq. 2.33. A right-moving electron injected into a TLL decays into right- and left-moving quasiparticles, another signal that Landau Fermi liquid theory does not apply in 1D. An exciting recent development is the reported observation of charge fractionalization in a quantum wire [28]. We study charge fractionalization in the context of a TLL ring in Chapter 5.

A common way of probing TLL behavior is through the bulk tunneling density of states (T-DOS). This quantity is intimately related to the Green's function (see Appendix A). Its low energy limit is a power law

$$\chi_{bulk}(E) \sim E^{\beta_{bulk}}, \tag{2.34}$$

where $\beta_{bulk} = (1/g_c + g_c - 2)/2$. Surprisingly, TLLs exhibit a different exponent for tunneling near the ends of the system or a strong impurity:

$$\beta_{end} = (1/g_c - 1). \tag{2.35}$$

These expressions are for spinless electrons. For an N channel Luttinger, the expressions become

$$\beta \to \frac{\beta}{N}. \tag{2.36}$$

Both exponents have been observed in single carbon nanotubes with plausible values of the

charged Luttinger parameter $g_{c+} \sim 0.2$ [20].

Finally, we examine the fate of the Fermi surface in a TLL with interactions. As calculated in Appendix A (see also [8]), we have that the occupation factor $n(k)$ has the form

$$n(k) \propto |k - k_F|^{\frac{g+1/g}{2}-1}, \tag{2.37}$$

for spinless electrons. The generalization to an N channel TLL is again given by Eq. 2.36 (with $\beta = (g+1/g)/2-1$). Here, instead of a discontinuity which signals that electrons near the Fermi surface are 'protected' from scattering events, the occupation factor *vanishes* at k_F in the TLL model. The vanishing of the T-DOS and the occupation factor at zero energy are manifestations of the so-called orthogonality catastrophe [8]. In the TLL, excitations bear little resemblance to electrons (i.e., they are 'orthogonal' to each other). This suppresses the ability of electrons to tunnel into our out of a TLL at low energies.

2.6 Outlook

In this chapter we have presented a short introduction to the TLL. It was found that the TLL model exhibits qualitatively different behavior from that of a Fermi liquid. This material will serve as an important reference for Chapters 4 and 5. More details of the formalism presented here may be found in Appendices A and B.

Chapter 3

Transverse Field Effects in Carbon Nanotubes: Band Structure

3.1 Introduction

The versatile bonding properties of carbon underlie its central importance as a building block of the macromolecules necessary for life on Earth. Allotropes of carbon arise in a diverse assortment of forms of various (effective) dimensionalities: fullerenes such as buckeyballs (0D), carbon nanotubes (1D), and graphene (2D). Anticipated theoretically [33], nanotubes were discovered by S. Iijima in the early 1990's [34]. The electronic properties of single-walled carbon nanotubes are exceptionally clean and exhibit ballistic conductances. Single-walled carbon nanotubes (SWNT) display remarkable band structure properties. Depending on the orientation of the tube's axis and the underlying graphene lattice, SWNTs may be either conducting or insulating[1]. That nanotubes may be produced relatively easily has lead to their use as a 'laboratory' in which to explore 1D physics.

In the present chapter we explore the effects of fields on the band structure of carbon nanotubes. It has been shown that a parallel magnetic field can have the striking effect of converting a metallic tube to a semiconducting one (and vice-versa) [35]. Here, instead of a parallel field, we discuss transverse field configurations (both electric and magnetic) and the conditions under which the spectrum remains gapless or a band gap opens up in armchair SWNTs. In the former case, we demonstrate, via band-structure calculations, simultaneous breaking of the valley degeneracy (of the two distinct Dirac points), the left-right-mover

[1]Given that we are interested in the quantum wire properties of SWNTs, we limit our discussion to so-called armchair nanotubes which are always conducting.

degeneracy, and the particle-hole symmetry. Moreover, the fields yield a non-negligible reduction in the Fermi velocity of conduction electrons traveling along the tube.

The above results are discussed in the case of an infinite system. For short tubes or finite length segments formed by tunnel barriers, boundary effects need to be taken into account. We find that applied fields influence multiple aspects of short nanotubes. Fields can alter the single-particle energy level spacing of the tube in two crucial ways. The linear dispersion of nanotubes is expected to give rise to a single particle energy spacing $E = \pi\hbar v_F/L$. In generalizing this expression to the case applied fields, careful accounting of the effect of left and right velocity asymmetry is required. Second, given that fields lift the Dirac point degeneracy described above, they can probe the extent of Dirac point scattering at tube ends.

Transverse field effects in carbon nanotubes have been studied before. The approach of this chapter differs from that of [36, 37, 38, 39] in that we derive the low energy spectrum directly from the tight-binding model rather than starting with the Dirac equation and its linear spectrum as an input. Hence our approach in calculating the band structure is similar to that presented in [33] in which the effects of a transverse magnetic field were examined. This more involved approach has the advantage of tracking the field-induced shift in Fermi momentum which turns out to have important implications for quantum dot physics. Our band structure calculation will then used as an input for a detailed Luttinger liquid calculation given in Chapter 4.

The organization of this chapter is as follows. In 3.2, the atomic structure of SWNTs is described. Their electronic structure is derived using a tight-binding calculation in 3.3. Field-dependent band structure is considered in 3.4 while 3.5 presents these effects in tubes of finite size. Finally, 3.6 summarizes our results.

3.2 Structure

A carbon nanotube can be visualized as tube of graphene which has been rolled up in a particular direction relative to the underlying honeycomb lattice. In graphene, carbon atoms reside at the vertices of a honeycomb lattice with a unit cell spanned by the vectors $\mathbf{a}_1$ and $\mathbf{a_2}$ (see Fig. 3.1). The honeycomb lattice is not a Bravais lattice: rather, it can be viewed as two inter-penetrating triangular lattices. We define the lattice vectors

$$\mathbf{a}_1 = \frac{a}{2}\left(\sqrt{3}, 1\right), \ \mathbf{a}_2 = \frac{a}{2}\left(\sqrt{3}, -1\right), \tag{3.1}$$

where $a \approx 1.42$ Å is the distance between nearest neighbor carbon atoms. The manner in which a tube can be thought to be rolled up is specified by graphene lattice vector $\mathbf{C} = (n, m) = n\mathbf{a}_1 + m\mathbf{a}_2$ which corresponds to the tube's circumference. We will focus primarily on the case of armchair nanotubes whose chiral vectors obey $n = m$.

In specifying the location of carbon atoms we imagine cutting the tube along its length and then flattening it onto the plane. We define the coordinates (x, s); the x-direction runs parallel to the tube's axis and s runs along the tube's circumference. Starting along the negative y-axis, increasing s indicates a direction that is counterclockwise as one looks along the positive x-axis. An atom of the A sublattice at a position $\mathbf{R} = (x, s)$ has three nearest-neighbors belonging to the B sublattice separated by a distance $a_c = 1.42$Å (which differs from the accepted graphene value due to curvature effects [33]). In particular, these nearest-neighbors reside at $\mathbf{R}_i$ $(i = 1, 2, 3)$ such that $\delta_i = \mathbf{R}_i - \mathbf{R}$ with

$$\delta_1 = \left(a/\sqrt{3}, 0\right), \ \delta_2 = \left(-a/2\sqrt{3}, a/2\right), \ \delta_3 = \left(-a/2\sqrt{3}, -a/2\right), \tag{3.2}$$

where $a = \sqrt{3}a_c$. The circumference of the tube is given by $L = \sqrt{3}na$.

3.3 Field-Free Electronic Structure

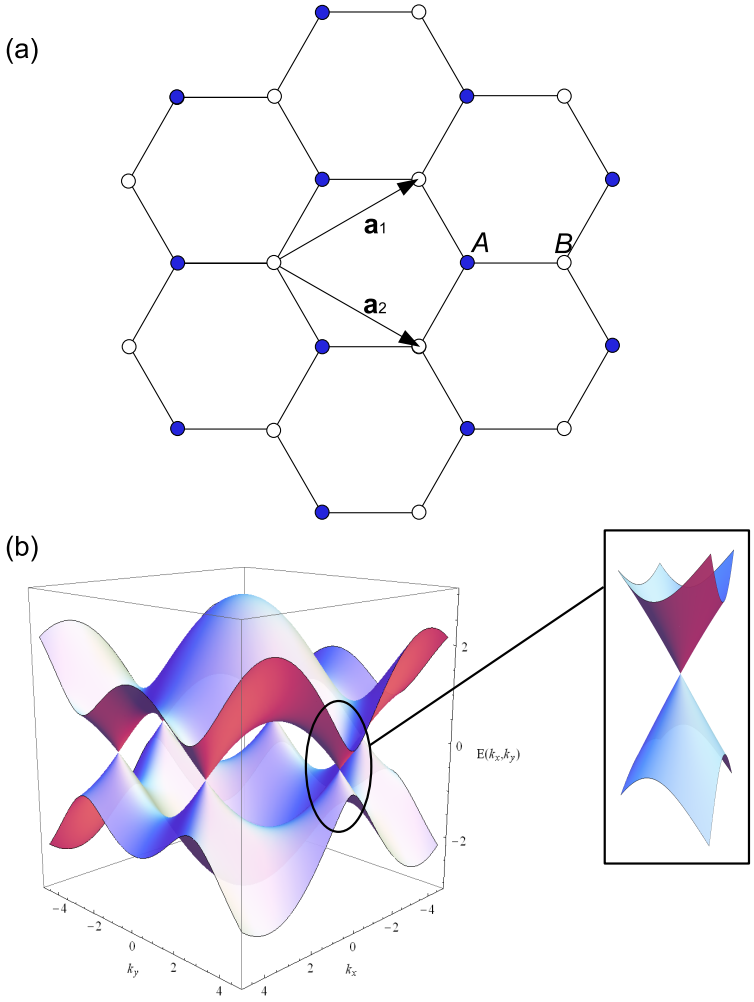

Figure 3.1: The (a) lattice structure and (b) electronic properties of graphene inform the salient properties of SWNTs.

The gross features of the band structure of graphene and carbon nanotubes are dictated by the underlying honeycomb lattice and its band structure 3.1. The band structure of graphene is well-captured by a tight-binding approximation. The carbon atoms in graphene are sp^2 hybridized. While the σ-bonded electrons remain tightly bound between the associated atoms, the unhybridized p-orbitals host electrons but these electrons can hop to nearest neighbors with an associated hopping integral $t \approx 3$ eV. The Hamiltonian describing this

motion is

$$H_0 = -t \sum_{\mathbf{R},\delta} |\mathbf{R} + \delta\rangle\langle\mathbf{R}|, \tag{3.3}$$

where $|\mathbf{R}\rangle$ is the state in which an electron is localized to the π-electronic state of the atom at $\mathbf{R}$ and the vector δ represents the displacement from $\mathbf{R}$ to any of its nearest-neighbors. Translational invariance of the Hamiltonian suggests the use of the Bloch wavefunctions of the form

$$|\Phi_{A/B}\rangle = \frac{1}{\sqrt{N}} \sum_{\mathbf{R}\in A/B} e^{i\mathbf{k}\cdot\mathbf{R}} |\mathbf{R}\rangle, \tag{3.4}$$

where $\mathbf{k}$ is the pseudomomentum and N is the number of atoms comprising the A (or B) sublattice.

Before presenting the full band structure, we would like to understand the low-energy physics. Neutral (undoped) graphene and SWNTs possess one electron on average, and are thus half-filled. The bipartite structure of the honeycomb lattice enforces particle-hole symmetry (i.e the dispersion is of the form $E(\mathbf{k}) = \pm |f(\mathbf{k})|$). Thus, half-filling corresponds to $E = 0$. We now identify those values of the pseudomomentum $\mathbf{K}$ in the first Brillouin zone which have $E(\mathbf{K}) = 0$. Applying Eqs. 3.3 and 3.4 reveals that $H|\Phi_A\rangle = 0$ if and only if

$$e^{i\mathbf{K}\cdot\delta_1} + e^{i\mathbf{K}\cdot\delta_2} + e^{i\mathbf{K}\cdot\delta_3} = 0. \tag{3.5}$$

The fact that these three quantities have unit modulus and sum to zero implies that they are symmetrically arranged around the unit circle. Hence, $e^{i\mathbf{K}\cdot(\delta_2-\delta_1)}$, $e^{i\mathbf{K}\cdot(\delta_3-\delta_2)}$, and $e^{i\mathbf{K}\cdot(\delta_3-\delta_1)}$ can only take the values $e^{i2\pi/3}$ or $e^{i4\pi/3}$. This gives rise to two inequivalent solutions

$$\mathbf{K} = \pm\frac{2\pi}{a}\left(\frac{1}{\sqrt{3}}, \frac{1}{3}\right). \tag{3.6}$$

All other solutions are equivalent to these up to the addition of a reciprocal lattice vector. The existence of the Dirac points assumes the equivalence of the A and B sublattices. For

example, if the two sublattices had different energies, the energy difference would open a gap [40].

The full band structure is given by

$$E_{\pm}(\mathbf{k}) = \pm t\sqrt{3 + 2\cos\left(k_y a\right) + 4\cos\left(k_y a/2\right)\cos\left(\sqrt{3}k_x a/2\right)}. \tag{3.7}$$

Expanding around the **K** points, we obtain a massless dispersion

$$E_{\pm}(\mathbf{q}) \approx \pm v_F|\mathbf{q}| + \mathcal{O}(q^2), \tag{3.8}$$

where $\mathbf{q} = \mathbf{q} \mp \mathbf{K}$ and v_F is the Fermi velocity, given by $\sqrt{3}ta/2 \approx 1 \times 10^6$ m/s [40].

The band structure of carbon nanotubes derives from the band structure of its underlying graphene lattice. Given that the chiral vector **C** connects equivalent points on the nanotube, single-valuedness of the electron wavefunction requires that

$$\mathbf{k} \cdot \mathbf{C} = 2\pi\ell, \tag{3.9}$$

where ℓ is an integer. We do not account for curvature effects other than to use a slightly smaller value of a_c, $a_c = 1.42$ Å [33].

The low-energy properties of a nanotube depend crucially on whether the points $\pm\mathbf{K}$ satisfy Eq. 3.9. It is straightforward to obtain that this is the case if and only if

$$n - m = 0 \bmod 3. \tag{3.10}$$

If this condition is met, a nanotube will inherit the linear dispersing modes of the Dirac point. If not, the tube will be gapped [33]. Interestingly, the application of a magnetic field parallel to the tube's axis can close this gap by shifting the position of the quantized momentum bands.

Our focus in the remainder of this work will be SWNTs with chiral vectors (n, n). These nanotubes, called armchair nanotubes because of the characteristic pattern the carbon-carbon bonds make as one circumnavigates the tube, are guaranteed to be metallic. In order to describe the response of armchair nanotubes to fields, we now set up the preliminary elements. We define

$$|\Phi^{\ell}_{A/B}\rangle = \frac{1}{\sqrt{N}} \sum_{\mathbf{R}\in A/B} e^{i\mathbf{k}\cdot\mathbf{R}} |\mathbf{R}\rangle, \tag{3.11}$$

where we now have $\mathbf{k} = (k_x, k_s)$, where $k_s = 0, 2\pi/L, ..., 2\pi(n-1)/L$. The Hamiltonian H_0 (Eq. 3.3) has matrix elements

$$\langle \Phi^{\ell'}_A | H | \Phi^{\ell}_B \rangle = -t \left(e^{i2\pi\ell a/\sqrt{3}L} + 2e^{-i2\pi\ell a/2\sqrt{3}L} \cos\frac{k_x a}{2} \right) \delta_{\ell,\ell'}. \tag{3.12}$$

The structure of H_0 is block diagonal. We obtain energies

$$E_{\ell,\pm}(k) = \pm t \sqrt{1 \pm 4\cos\left(\frac{\ell\pi}{n}\right)\cos\left(\frac{k_x a}{2}\right) + 4\cos^2\left(\frac{k_x a}{2}\right)}, \tag{3.13}$$

where the corresponding eigenstates $|\ell, \pm\rangle$ are linear combinations of the states $|\Phi^{\ell}_{A/B}\rangle$. As expected, the band structure reflects the fact that the armchair nanotube inherits the $\pm\mathbf{K}$ Dirac points of graphene. In particular, the states

$$|R\rangle \equiv |0, +\rangle = \frac{1}{\sqrt{2}} \left(|\Phi^0_A\rangle + |\Phi^0_B\rangle \right), |L\rangle \equiv |0, -\rangle = \frac{1}{\sqrt{2}} \left(|\Phi^0_A\rangle - |\Phi^0_B\rangle \right), \tag{3.14}$$

have dispersions

$$E_{\pm}(k) = \pm\hbar v_F |k - \alpha k_F|, \tag{3.15}$$

near zero energy in the vicinity of the Fermi points $k_F = 4\pi/3a$ which are indexed by $\alpha = \pm$ (see Fig. 3.2)[2] This band structure may be confirmed by probing the density of states of the tube [33].

[2]We will drop the x subscript on k_x.

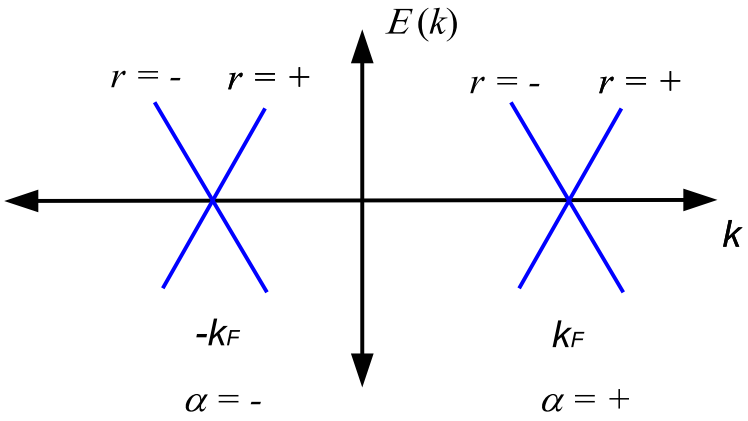

Figure 3.2: Schematic of the low-energy dispersion of an armchair nanotube described by Eq. 3.15. The indices r and α specify branches of the dispersion.

3.4 Field-Dependent Effects

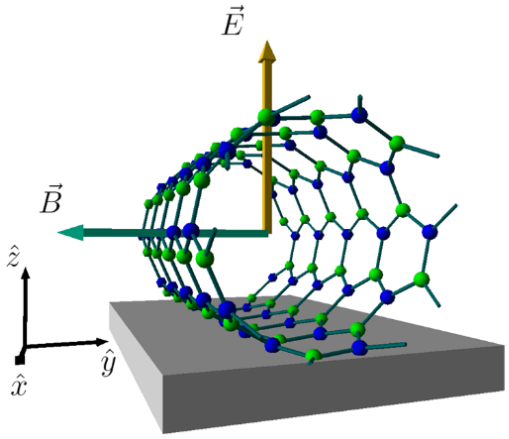

Figure 3.3: A (5,5) carbon nanotube in the presence of transverse magnetic (pointing in the $-\hat{y}$) and electric fields. The carbon atoms belonging to the A and B sublattices are indicated by dark (blue) and light (green) shading, respectively.

We now turn to the central question of this chapter: what effect do transverse electric and magnetic fields have on the band structure of a SWNT? The setup of interest is shown in Fig. 3.3. Semiclassically, the presence of an electric or magnetic field generically gives rise to a torque on the particle with respect to the tube's axis and thus angular momomentum is

not conserved. This motion thus tends to reduce the forward speed of the electron. Quantum mechanically, we find that the angular momentum of an electron around the tube ($\hbar\ell$) ceases to be a good quantum number: fields couple states belonging to different ℓ-subspaces. The effect of this coupling is to reduce the Fermi velocity near the Dirac points. This reduction of Fermi velocity has been derived by several authors [36, 37, 38]. A central aspect of the field response are the perturbed wavefunctions which are dervied in Appendix C.

We also investigate the effects of the simultaneous application of a magnetic and electric field. The case of mutually orthogonal fields is reminiscent of a classical velocity selector. For a classical charged particle moving in the presence of **E** and **B** fields, a particle moving at the speed $v = E/B$ will be undeflected if the electric and magnetic forces are antiparallel (i.e., the particle moves parallel to $\mathbf{E}\times\mathbf{B}$ [41]). Our quantum mechanical results reflect these expectations. Working in the regime $E/B \approx v_F$, the linear dispersion becomes asymmetric, with right- and left-movers travelling at different speeds ($v_R \neq v_L$). Indeed, we find that for the field configuration shown in Fig. 3.3, $v_R > v_L$.

The presence of two fields also breaks time-reversal and particle-hole symmetry. The breaking of these symmetries is maximal for $\chi = \pi/2$. As the fields are tuned away from mutual orthogonality, we find that a gap develops. The opening of this gap is related to the fact that fields engender an energy difference on the two sublattices.

3.4.1 Tight-binding model

For concreteness, we consider an external magnetic field that is applied in the negative y-direction; an applied electric field makes an angle χ with the magnetic field and is transverse to the tube's axis. These fields give rise to scalar and vector potentials

$$U(s) = |e|ER\cos\left(\frac{s}{R} - \chi\right), \tag{3.16}$$

$$\mathbf{A} = -Bz\hat{x}, \tag{3.17}$$

respectively, where E and B are the electric and magnetic field strengths ($R = L/2\pi$).

The scalar potential gives rise to an on-site potential described by the matrix element

$$\langle \Phi_A^{\ell'} | H | \Phi_A^{\ell} \rangle = \langle \Phi_B^{\ell'} | H | \Phi_B^{\ell} \rangle = \frac{tU}{2} e^{\pm i\chi}, \tag{3.18}$$

for $\ell' = \ell \mp 1 \mod n$ where $U = |e|ER/t$. The electric field strength is related to U by $E = Ut/|e|R \approx 42\ U/n$ V/nm. Accordingly, Eq. 3.12 becomes

$$\langle \Phi_A^{\ell'} | H | \Phi_B^{\ell} \rangle = -\frac{t}{2n} \sum_{\mathbf{R} \in B, \mathbf{R}' \in A} e^{i(k \cdot \mathbf{R} - k' \cdot \mathbf{R}') + \frac{ie}{\hbar}(G_j - G_i)}, \tag{3.19}$$

where the sum runs over nearest neighbors $\mathbf{R}$, $\mathbf{R}'$ and

$$G_j - G_i \approx \int_0^1 d\lambda\ (\mathbf{R}_i - \mathbf{R}_j) \cdot \vec{A}\,(\vec{r} + \lambda(\mathbf{R}_i - \mathbf{R}_j)) \tag{3.20}$$

is the Aharonov-Bohm phase associated with the magnetic field [42]. The full form of Eq. 3.19 is given in Appendix C (Eq. C.2). We have assumed that the hopping integral t is independent of the electric field. The dimensionless parameter b is given by $b = B\frac{\sqrt{3}|e|L^2}{4\pi^2\hbar}$. Numerically, for an (n, n) nanotube, the magnetic field in Teslas is related to the dimensionless parameter b via $B \approx 8.1 \times 10^4 \times b/n^2$ T. As advertised, the effect of the fields is to mix states of different angular momentum.

Given that experimentally accessible field strengths are such that $U, b \ll 1$, we apply perturbation theory to study the low-energy physics. While standard perturbation theory may be applied to the given problem, the fact that the states $|\Phi_A^0\rangle$ and $|\Phi_B^0\rangle$ are nearly degenerate requires that such a calculation be done with care. To this end, we apply the so-called *effective Hamiltonian method* which is equivalent to a Schrieffer-Wolff transformation [43, 44]. The method involves performing unitary transformations which eliminate couplings outside of the nearly degenerate subspace. To second order, the resultant effective

Hamiltonian takes the form

$$\langle r|H_{eff}|r'\rangle = \langle r|H|r'\rangle + \frac{1}{2}\sum_{\ell\neq 0,\zeta=\pm}\left(\frac{\langle r|H|\ell,\zeta\rangle\langle\ell,\zeta|H|r'\rangle}{E_r(k)-E_{\ell,\zeta}(k)} + \frac{\langle r|H|\ell,\zeta\rangle\langle\ell,\zeta|H|r'\rangle}{E_{r'}(k)-E_{\ell,\zeta}(k)}\right), \quad (3.21)$$

where the $|r\rangle, |r'\rangle = |R\rangle, |L\rangle$ as defined in Eq. 3.14. A generic expression for the effective Hamiltonian containing higher order terms is given in Appendix B of [44].

We now present an overview of the results of the band structure calculation. A more complete account is given in Appendix C.

3.4.2 Case of $E = 0$ or $B = 0$

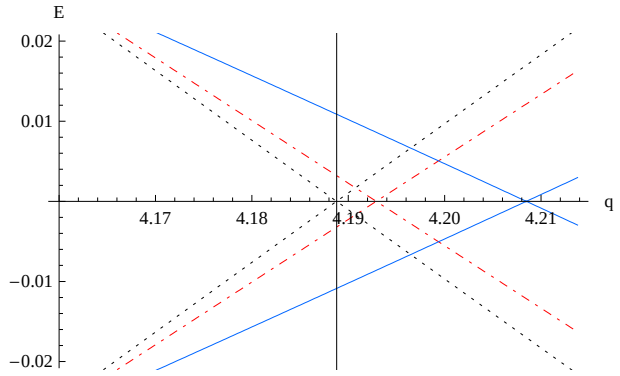

Figure 3.4: Spectrum of a $(5, 5)$ carbon nanotube near the $\alpha = +$ Dirac Fermi point (field-free value $k_F = \alpha 4\pi/3a$ indicated by the vertical line) in the presence of an external transverse electric field with $U_0/t = 0$ (black dotted), 0.2 (red dot-dashed), 0.4 (blue solid) as the crossing moves to the right. The horizontal axis indicates the value of q, where $q = ka$; the vertical axis is given in units of t, the hopping integral ($t \approx 3$ eV).

In the presence of a single electric or magnetic field, the low-energy dispersion remains gapless but there exists a reduction in the Fermi velocity and a shift in the Fermi momentum. For a magnetic field, the Fermi velocity is given by

$$\tilde{v}_F = v_F\left(1 - \Delta v_1 b^2\right), \quad (3.22)$$

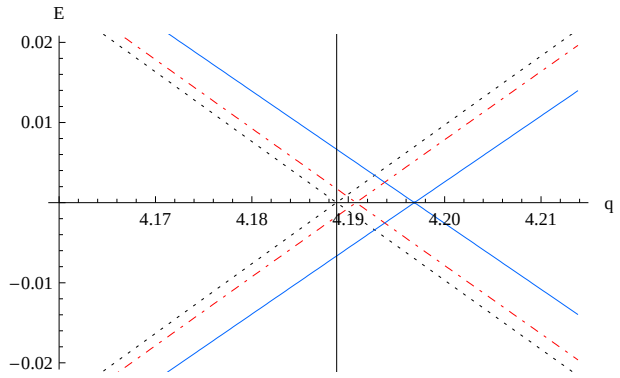

Figure 3.5: Spectrum of a $(5, 5)$ carbon nanotube near the $\alpha = +$ Dirac Fermi point (field-free value $k_F = \alpha 4\pi/3a$ indicated by the vertical line) in the presence of a magnetic field $b = 0$ (black dotted), 0.2 (red dot-dashed), 0.4 (blue solid) (as the crossings move to the right). The horizontal axis indicates the value of q, where $q = ka$; the vertical axis is given in units of t, the hopping integral ($t \approx 3$ eV). While the shift in Fermi point is clear, the change in the slope (see Eq. 3.23) is small and difficult to discern.

where Δv_1 is a function of n and is given by Eq. C.6b. For large tubes $\Delta v_1 \approx 1/3$. For the case of an electric field we have

$$\tilde{v}_F = v_F \left(1 - \Delta v_2 U^2\right) \tag{3.23}$$

where $\Delta v_2 \approx n^2/\pi^2$. For $n = 10$, a field strength of 0.1 V/nm gives rise to a 10% reduction of the Fermi velocity.

Single electric or magnetic fields will shift the Fermi points. That is, the nanotube still has the same low-energy spectrum but with renormalized values of k_F (see Eq. C.7). The band structure of a $(5, 5)$ tube in the presence of electric and magnetic fields of various strengths is shown in Figs. 3.4 and 3.5. As mentioned above, the reduction in Fermi velocity has been noted by several authors. In [36], the nanotube was modeled as a smooth cylinder and a low-energy Dirac spectrum was put in by hand. Our results are in agreement with this work in the limit of small fields and large n.

3.4.3 Case E ⊥ B

This is the case of primary interest for the work presented in the next chapter. In this case, the band structure remains gapless but both time-reversal and particle-hole symmetries of the band structure are broken. Left- and right-movers now travel at different speeds. For a magnetic field in the negative y-direction and an electric field in the positive z direction we have

$$\tilde{v}_r = v_F \left(1 - \Delta v_1 b^2 - \Delta v_2 U^2 \pm \Delta v_3 b U\right), \tag{3.24}$$

where $r = +/-$ for right-/left-movers, respectively. The quantity Δv_3 is given by Eq. C.6d and for large tubes is $\Delta v_3 \approx n/\pi$. For the fields we consider, E/B is roughly the same order of magnitude as v_F. The reduction in Fermi velocity mimics the effects of a classical velocity selector. For tubes of diameter $d = 6.78$ nm ($n = 50$) and experimentally accessible field strengths $B = 6.4$ T and $E = 0.02$ V/nm, we find $v_R = 0.89 v_F$ and $v_L = 0.77 v_F$, yielding a pronounced asymmetry in right- and left-moving velocities [45].

Near the two Dirac points corresponding to $\alpha = \pm$ ($\alpha k_F \approx \pm\frac{4\pi}{3a}$) we have

$$E_{r\alpha}(k) = \hbar r \tilde{v}_r \left(k - \alpha \tilde{k}_F\right) + \alpha t \Delta s + \mathcal{O}(\Delta k^2). \tag{3.25}$$

By definition, $\tilde{k}_F$ is the momentum for which the left and right moving bands for a given Fermi point are degenerate and again is generally different from $4\pi/3a$ in the presence of fields. The precise forms of k_F and Δs are given by Eqs. (C.7) and (C.8), respectively. The solid (blue) lines in Figs. 3.6 (for $\alpha = +$) indicate low-energy dispersion of a $(5, 5)$ nanotube in the presence of crossed electric ($v = 0.2$) and magnetic ($b = 0.4$) field.

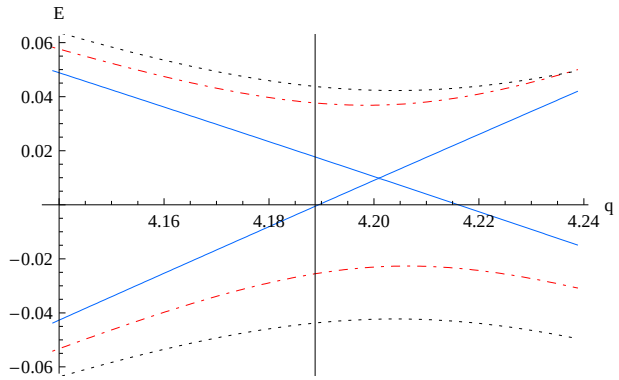

Figure 3.6: Spectrum of a $(5,5)$ carbon nanotube near $\alpha = +$ Dirac Fermi point (field-free value $\alpha k_F = 4\pi/3a$ by the vertical line) in the presence of transverse electric and magnetic field ($U/t = 0.2$ and $b = 0.4$). The angle between $\vec{E}$ and $\vec{B}$ being 0 (black dotted), $\pi/4$ (red dot-dashed), $\pi/2$ (blue solid) (from outer to inner). The horizontal axis indicates the value of q, where $q = ka$; the vertical axis is given in units of t, the hopping integral ($t \approx 3$ eV).

3.4.4 Case $\chi \neq \pi/2$

In this case, the effective Hamiltonian develops off-diagonal elements and thus a gap arises (see Fig. 3.6). The magnitude of this gap is

$$\epsilon_{gap} \approx tbU \frac{2\sqrt{3}\cos\frac{\pi}{3n}}{1+2\cos\frac{\pi}{3n}} \left|\cos\chi\right| . \tag{3.26}$$

For example, a (15,15) tube parallel electric and magnetic fields 1 V/nm and 10 T respectively gives $\epsilon_{gap} \approx 4$ meV. For electric and magnetic fields which are not parallel, this gap is weakly indirect. Given that fields open gaps as well as shift the energy of the Fermi points (Eq. 3.25), they may be used to tune the conductance of the tube to values $G = 0$, $2e^2/h$, or $4e^2/h$.

3.5 Finite size effects

As is well known, finiteness of the tube length leads to a quantized single particle spectrum which depends on the boundary conditions associated with the tube's ends. We assume that the wavefunctions at a given end are related by $\psi_{R\alpha\sigma} = \sum_{\alpha'\sigma'} M_{\alpha\alpha'\sigma\sigma'}\psi_{L\alpha'\sigma'}$ where M is a

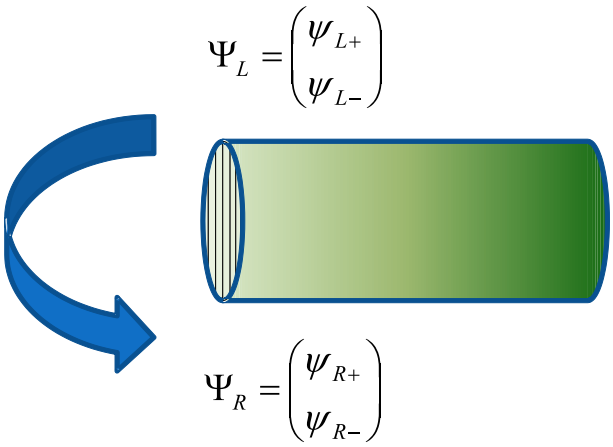

Figure 3.7: Scattering process described by Eq. 3.29. A left-moving electron described by the spinor Ψ (shown in the Fermi-point (α) basis is incident at a tube end. The details of how the tube is terminated will affect the scattering matrix $S_{\alpha,\alpha'}$.

matrix which depends on the the microscopic details of the tube end but is assumed to be energy independent (see Fig. 3.7). We specialize to the case that the boundary conditions do not affect spin; that is we take $M_{\alpha\alpha\sigma\sigma'} = S_{\alpha\alpha'}\delta_{\sigma\sigma'}$, where $\delta_{\sigma\sigma'}$ is the Kronecker delta function. We thus assume that any magnetic impurities at the tube ends are negligibly weak.

In order to obtain the appropriate boundary conditions for the case of an asymmetric dispersion, we demand that the first quantized kinetic energy operator $\hat{H}_0 = -i\hbar \sum_{r\alpha} r v_r \partial_x$ together with the boundary conditions is self-adjoint [46]. This treatment does not account for the effect of interactions on the boundary conditions which would be more naturally discussed in terms of the bosonic fields (this analysis is performed in the next chapter). Such an analysis shows that there is an additional term in the current proportional to $g_2 - g_4$ which vanishes for the density-density interaction considered here [47, 48]. By definition,

$$\langle \Psi, \hat{H}_0 \Psi \rangle = -i\hbar \sum_{r\alpha} \int dx \; r v_r \psi^\dagger_{r\alpha} \partial_x \psi_{r\alpha}. \tag{3.27}$$

Since the boundary effects are assumed to be independent of spin, we have dropped the

spin index. For an arbitrary spinor Ψ with $\Psi = (\psi_R\ \psi_L)^T$ where ψ_R and ψ_L are both two-component spinors in the Fermi point basis ($\psi_r = (\psi_{r+}\ \psi_{r-})^T$), self-adjointness gives

$$\langle \Psi, \hat{H}_0 \Psi \rangle = \langle \hat{H}_0 \Psi, \Psi \rangle. \tag{3.28}$$

Integrating the left-hand side of this equation by parts gives

$$\begin{aligned} \langle \Psi, \hat{H}_0 \Psi \rangle &= -i \sum_{\alpha=\pm} \int dx \, (v_R \psi^*_{R\alpha} \partial_x \psi_{R\alpha} - v_L \psi^*_{L\alpha} \partial_x \psi_{L\alpha}) \\ &= -i \sum_{\alpha=\pm} \Big[v_R \psi^*_{R\alpha} \psi_{R\alpha} - v_L \psi^*_{L\alpha} \psi_{L\alpha} \Big]_{x=0,L} \\ &\quad + \langle \hat{H}_0 \Psi, \Psi \rangle. \end{aligned}$$

Self-adjointness is satisfied as long as the boundary terms vanish, and this leads to

$$\psi_{R\alpha} = S_{\alpha\alpha'} \psi_{L\alpha'}, \tag{3.29}$$

with $\sqrt{v_R/v_L}\, S$ unitary.

The details of the S-matrix can vary for each experimental set-up and depend on physical attributes such as the substrate, the hardness of the confining potential offered by the leads and the orientation of the tube's sublattices with respect to the leads. These parameters can be incorporated as variables in the boundary conditions which can then be utilized to obtain the single-particle spectrum. The most general version of these boundary conditions are outlined in Ref. [49] via an effective-mass model.

For a given S-matrix the spectrum of single particle states can be determined by applying the condition of Eq. (3.29) at both ends and demanding that both the left and right movers have the same energy. The two Fermi points give rise to two sets of bands. The energy between two adjacent states in the *same* band is equal to $\pi \hbar v_H / L$ where v_H is the harmonic

mean,

$$v_H = \frac{2v_R v_L}{v_R + v_L}. \tag{3.30}$$

However, the energy offset of the bands from the Fermi energy depends on the details of the S-matrix. In general, the two Fermi points will give rise to two sets of energy states given by $\pi n\hbar v_H/L + \Delta_1$ and $\pi n\hbar v_H/L + \Delta_2$ where $n \in \mathbb{Z}$.

The energy difference between bands is defined as $\Delta_{band} = \Delta_1 - \Delta_2$ (and for convenience we define Δ_{band} such that $|\Delta_{band}| < \pi\hbar v_H/L$). We examine two special cases for the S-matrix; deriving the Δ_{band} for the most general scattering matrix would be a straightforward extension. First, consider the case in which the tube ends do not mix the Fermi points, though we allow the phase shift the electron suffers at the tube end $\delta_\pm(x)$ to be different for the two Fermi points ($\alpha = \pm$) and the two tube ends ($x = 0, L$). In this case we have $S_{++}(x) = \sqrt{v_L/v_R}e^{i\delta_+(x)}$, $S_{--}(x) = \sqrt{v_L/v_R}e^{i\delta_-(x)}$ and $S_{-+}(x) = S_{+-}(x) = 0$. The energy offset between the bands takes the form

$$\Delta_{band} = \frac{\pi\hbar v_H}{L}\mathcal{F}\left[\frac{\tilde{\delta}_1}{2\pi} + \frac{2t\Delta s}{\hbar\pi v_H/L}\right], \tag{3.31}$$

where $\tilde{\delta}_1 = (\delta_+(L) - \delta_+(0)) - (\delta_-(L) - \delta_-(0))$ and $\mathcal{F}(x) = x - \lfloor x \rfloor$ and $\lfloor x \rfloor$ is the greatest integer less than or equal to x, and the quantity $t\Delta s$ is the field induced offset between the two Fermi points as givin in Eq. C.8.

Now, consider an electron that is completely scattered into the opposite Fermi point at both boundaries. For simplicity we take $S_{\alpha\alpha'}(x) = \sqrt{v_L/v_R}e^{i\delta(x)}\delta_{\alpha,-\alpha'}$. In this case, the splitting between bands takes the form

$$\Delta_{band} = \frac{\pi\hbar v_H}{L}\mathcal{F}\left[\frac{2}{\pi}k_F L + \frac{2t\Delta s}{\pi\hbar v_H/L}\left(\frac{v_R - v_L}{v_R + v_L}\right)\right]. \tag{3.32}$$

For the limiting case of no fields (this also means that $v_H = v_R = v_L \equiv v_F$), one expects the existence of sets of four single-particle states, namely two degenerate sets of spin states

and two sets of band states whose energy splitting depends on the various phase shifts and the extent to which modes at the two Fermi points mix. For no Fermi point mixing, the interband splitting is $\hbar v_F \tilde{\delta}_1/2L$ while for complete Fermi point mixing, the splitting is $\frac{\pi\hbar v_F}{L}\mathcal{F}[2Lk_F/\pi]$. Coulomb blockade experiments have shown an interband band splitting of about 10% [50] of the $\pi\hbar v_F/L$. Such a persistent approximate degeneracy in band energies for a range of tubes [51] suggests that the magnitude of Fermi point mixing in these samples is minimal.

As discussed above, the boundary conditions in a given experiment are not directly observable since Δ_{band} depends on several parameters. Fields provide a way of controlling Δ_{band} as well as studying its physical origin in a particular sample. By scanning through various field strengths, the variation of the band offset can reveal information about the nature of boundary scattering. For example, the extent to which a given tube interpolates between the two expressions given in Eqs. (3.31) and (3.32) can be used to determine the importance of (Fermi point) backscattering at the tube ends. In the case of a *natural* band degeneracy in a tube (that is, no Fermi point mixing at the ends of the tube and $\tilde{\delta}_1 = 0$), both electric and magnetic fields need to be applied to break the degeneracy; the magnitude of the subband splitting as a function of fields can be extracted from Eq. (3.31) by setting $\tilde{\delta}_1 = 0$. An alternative approach for breaking the subband degeneracy was explored by Ref. [52] in which a nonuniform external potential along the tube was applied. However, this approach becomes infeasible for the case of a diagonal scattering matrix since it relies on band curvature away from half-filling.

Thus combining electric and magnetic fields can provide a means of breaking and tuning the degeneracy of the quantum states of electrons inhabiting the nanotube quantum dot. Of the four possible states discussed above, where the direction of spin is defined with respect to the magnetic field, an extra electron would occupy the ground state, which can be chosen to be any of the four depending on the direction of the fields. The quantum state can be characterized by a superspin inhabiting a $SU(2) \otimes SU(2)$ band and spin space.

The enhanced control of the spectrum of nanotubes that fields offer would obviously have important implications for any potential quantum information applications (see [53]).

3.6 Summary and outlook

In this chapter, a detailed band structure calculation of transverse field effects in SWNTs was presented. A single electric or magnetic field alters the Fermi velocity. The simultaneous application of electric and magnetic fields breaks particle-hole symmetry, induces an asymmetry between left- and right-mover speeds, and opens a gap. This calculation will be used as input for a detailed TLL analysis in the next chapter.

Chapter 4

Carbon Nanotubes in Fields: A Tunable Tomonaga-Luttinger Liquid

A hallmark of the physics of carbon nanotubes is a persistent degeneracy associated with the Dirac point. This degeneracy derives from the equivalence of the A and B sublattices of the underlying graphene lattice and thus is extremely resilient. As seen in the last chapter, fields offer a controllable means of lifting this degeneracy. Given the rich variety of strongly correlated phenomena observed in carbon nanotubes including TLL physics [50], the Kondo effect [54], and Mott phases [55], the prospect of accessing this usually 'silent' degree of freedom would offer a new facet to each of these phenomena. As demonstrated in the last chapter, transverse fields also break the degeneracy of right- and left-mover speeds as well as particle-hole symmetry. Given that fields can tune the effective velocity of electrons on a tube, this shows that they are an excellent means of altering the ratio of interaction strength to the Fermi energy in SWNTs. This makes nanotubes potentially the only systems to date in which the associated TLL physics can be tuned in a controlled fashion. Fields also present a means of testing the range of validity of the TLL model in carbon nanotubes, moving beyond the one-sample-one-data-point paradigm.

Either an electric field [36] or a magnetic field [37, 38] alone suffices to change the value of the TLL parameter from its field-free value. The magnitude of the electric field required to bring about a significant change is well within current experimental reach [56]. That fields alter the TLL parameter has been predicted by several groups [36, 37, 38]. We extend this analysis by considering how fields alter the circumferential electronic wave functions. We show that fields give rise to a Luttinger-type interaction in the channel associated with the density differences between nanotube bands. Thus we predict that akin to spin-charge

separation, transverse fields can induce a spin-charge-band separation wherein the three degrees of freedom move at different velocities. We show that such a tuning of the TLL parameters can also mediate a transition from spin-density-wave (SDW) ordering to charge-density-wave (CDW) ordering. Additionally, naturally degenerate orders are distinguished by fields.

These effects have a profound effect on the shell-filling structure of Coulomb-blockaded nanotubes. In addition to the novel interaction effects described above, the no-current boundary condition at the end of such tubes is also affected by fields. In particular, the charge current operator does not take the form $J_{c+} = v_R \rho_{R,c+} - v_L \rho_{L,c-}$ as it would in the absence of interactions. For example, fields can give rise to shell-filling in which the electron is completely polarized to one Fermi point. This feature has implications for proposals which endeavor to use carbon nanotubes as a component for quantum memory [53].

The organization of this chapter is as follows. In 4.1, we derive an effective TLL model using the field effects of Chapter 3 and Appendix C as input. In 4.2, an RG analysis of the TLL phases is studied, demonstrating that the prominence of various ordering tendencies can be altered by fields. Coulomb-blockaded tubes in the presence of fields are considered in 4.3. Section 4.4 presents our conclusions.

4.1 Effective Luttinger Theory

Even in the presence of fields, electrons are locked into their lowest energy radial modes. We thus develop an effective 1D Luttinger theory which incorporates the field-induced effects uncovered by the band structure calculation presented in the previous chapter. The fermionic operator on the surface of the tube takes the form

$$\Psi_\sigma(x,s) = \sum_{p\alpha} \varphi_{p\alpha}(x,s)\psi_{p\alpha\sigma}(x), \tag{4.1}$$

where $\psi_{p\alpha\sigma}(x)$ is the (effective) one-dimensional field operator at the point x along the tube axis associated with the A and B sublattices ($p = A(+), B(-)$), Fermi points $\alpha k_F = \alpha 4\pi/3a$ ($\alpha = \pm$), and spin $\sigma = \uparrow (+), \downarrow (-)$. The Bloch wave functions $\varphi_{ps}(x, s)$ retain detailed information regarding the response of the electrons to the applied fields. The sublattice basis (p) and the left-/right-moving basis (r) are related via the transformation $\psi_{p\alpha\sigma} = \sum_r U_{pr}\psi_{r\alpha\sigma}$, where $U^\dagger \sigma_y U = \sigma_z$.

Using Eq. C.12 as input, we find a kinetic energy term

$$H_0 = -i\hbar \sum_{r\alpha\sigma} \int dx \; r v_r \psi^\dagger_{r\alpha\sigma} \partial_x \psi_{r\alpha\sigma}. \tag{4.2}$$

The shift of the Fermi points is described by the term

$$H_\Delta = \frac{1}{2} \sum_{r\alpha\sigma} \alpha t \Delta s \psi^\dagger_{r\alpha\sigma} \psi_{r\alpha\sigma}. \tag{4.3}$$

The interaction term takes the general form

$$H_{int} = \frac{1}{2} \int d\mathbf{r} \int d\mathbf{r}' \; \Psi^\dagger_\sigma(\mathbf{r}) \Psi^\dagger_{\sigma'}(\mathbf{r}') U(\mathbf{r} - \mathbf{r}') \Psi_{\sigma'}(\mathbf{r}') \Psi_\sigma(\mathbf{r}), \tag{4.4}$$

where $\Psi_\sigma(\mathbf{r})$ is the field in Eq. (4.1) describing low-energy electrons. Following [57], we employ the form of the Coulomb interaction on the surface of a cylinder given by

$$U(x - x', s - s') = \frac{e^2/\kappa}{\sqrt{(x - x')^2 + 4R^2 \sin^2\left(\frac{s - s'}{2R}\right) + a_z^2}}, \tag{4.5}$$

where R is the radius of the tube and x and s the coordinates defined in the previous section and $a_z \approx a$ is roughly the thickness of the graphene sheet [57]. The form of the interaction in Eq. (4.4) is explicitly given in terms of two-dimensional integrals. Effective 1D interaction terms can be obtained by expressing $\Psi_\sigma(\mathbf{r})$ in terms of the linear and circumferential fields as in Eq. (4.1) and integrating out the circumferential degrees of freedom from

Eq. (4.4). Details of this calculation are presented in Appendix C. Crucially, the integration over the circumferential degrees of freedom generates field-induced terms that give rise to novel physics and can be traced to the dependence of the ground state wave function on non-zero angular momentum states in the circumferential direction.

In order to derive this effective low-energy description involving interactions, we introduce a bosonic description of the fermions. We deviate slightly from the notation of Chapter 2 in order to accommodate the extra fermionic channel. Following [57], we rewrite Eq. 2.6 as

$$\psi_{r\alpha\sigma} = \frac{\eta_{r\alpha\sigma}}{\sqrt{2\pi a_c}} \exp\left[i\alpha k_F x + i\varphi_{r\alpha\sigma}\right], \tag{4.6}$$

where the bosonic fields φ satisfy the commutation relations

$$[\varphi_{r\alpha\sigma}(x), \varphi_{r'\alpha'\sigma'}(x')] = -i\pi r\delta_{rr'}\delta_{\alpha\alpha'}\delta_{\sigma\sigma'}\mathrm{sgn}(x-x'). \tag{4.7}$$

The Klein factors obey the commutation relations

$$\{\eta_{r\alpha\sigma}, \eta_{r'\alpha'\sigma'}\} = 2\delta_{rr'}\delta_{\alpha\alpha'}\delta_{\sigma\sigma'}. \tag{4.8}$$

The effective density in a given channel takes the form

$$\widetilde{\rho}_{r\alpha\sigma}(x) = \frac{r}{2\pi}\partial_x\varphi_{r\alpha\sigma}(x). \tag{4.9}$$

The kinetic energy associated with the linearly dispersing fermionic modes is quadratic in the bosonized fields and is given by

$$H_0 = \frac{1}{4\pi}\sum_{\alpha\sigma}\int dx\left[v_R\left(\partial_x\varphi_{R\alpha\sigma}\right)^2 + v_L\left(\partial_x\varphi_{L\alpha\sigma}\right)^2\right]. \tag{4.10}$$

We now introduce the channel decomposition

$$\varphi_{r\alpha\sigma} = \frac{\sqrt{\pi}}{2}\left(\phi_{c+} + r\theta_{c+} + \alpha\phi_{c-} + r\alpha\theta_{c-} + \sigma\phi_{s+} + r\sigma\theta_{s+} + \alpha\sigma\phi_{c-} + r\alpha\sigma\theta_{s-}\right). \tag{4.11}$$

As for the interactions, the dominant contributions also come from quadratic terms reflecting net density-density type interactions which preserve the Fermi-point quantum number α of the electrons. Backscattering processes are irrelevant in the RG sense in the high temperature regime of interest here and suppressed for large tubes [57, 16]. The usual Coulomb 'forward scattering' term involving the net charge density, which in the bosonized representation is given by (cf. Eq. 2.10)

$$H_{\alpha FS,0} = \frac{2}{\pi}\int dx\ \widetilde{V}(k \approx 0)\left(\partial_x\theta_{c+}\right)^2, \tag{4.12}$$

where

$$V \approx \frac{2e^2}{\kappa}\left(|\ln kR| + c_0\right) \tag{4.13}$$

is the Fourier transform of $V(x)$ and c_0 is a function of n (see Eq. C.13).

The presence of either an electric or magnetic field gives rise to additional quadratic terms arising from Eq. 4.4. These terms have their origin in the non-zero angular momentum components of the circumferential wave function $\varphi_{r\alpha}(x,s)$ in Eq. (4.1). A detailed accounting of the radial wave functions (see Appendix C) shows that an electric field contributes a term

$$H_{\alpha FS,E} = \int dx \left(\frac{2e^2}{\kappa}\right)\left(\frac{2}{\pi}\right) h_1 U^2 \left(\partial_x\phi_{c+}\right)^2, \tag{4.14}$$

whereas a magnetic field provides a contribution

$$H_{\alpha FS,B} = \int dx \left(\frac{2e^2}{\kappa}\right)\left(\frac{2}{\pi}\right) h_2 b^2 \left(\partial_x\theta_{c-}\right)^2. \tag{4.15}$$

The $H_{\alpha FS,B}$ thus gives a TLL parameter in the $c-$ sector such that $g_{c-} \neq 1$. In the presence

of mutually perpendicular transverse electric and magnetic fields, there is an additional contribution to the interaction

$$H_{\alpha FS,BE} = \lambda \int dx (\partial_x \theta_{c-})(\partial_x \phi_{c+}), \tag{4.16}$$

where $\lambda = 4e^2 bUh_3/\pi\kappa$ and the values of h_1, h_2, and h_3 are given in Appendix C. The Luttinger liquid Hamiltonian takes into account all these quadratic terms; other terms emerging from the interaction potential are sub-dominant and can be considered perturbatively.

A physical picture of the origin of these field-dependant interaction terms follows from the fact that the (dimensionless) charge density has the spatial profile (Eq. C.9)

$$\rho_{r\alpha} \sim 1 + t_1 ru \sin \frac{s}{R} + t_2 \alpha \cos \frac{s}{R} b. \tag{4.17}$$

The coordinate s is defined in 3.2. The field response described by Eq. 4.17 is broadly consistent with the magnetic field coupling to momentum via $(p - eA/c)^2$ and hence to αk_F, resulting in a term $\sim \alpha b$. The electric potential differs slightly between adjacent A and B sites, and in turn couples to left- and right-movers differently, resulting in a term $\sim rU$. Equation (4.4) thus gives rise to interactions between the charge densities $\partial_x \theta_{c\pm}$ and currents $\partial \phi_{c+}$. We therefore obtain the following nonvanishing terms: $\partial_x \theta_{c+}$, $\partial_x \theta_{c-} \sim b$, and $\partial_x \phi_{c+} \sim u$.

Field effects are more dramatic for larger tubes. In the large tube regime, $h_3 \gg h_1, h_2$ and thus we focus on the interactions $H_{\alpha FS,0}$ and $H_{\alpha FS,BE}$. The Hamiltonian of interest is

$$H_{tot} = H_0 + H_{\alpha FS,0} + H_{\alpha FS,BE}. \tag{4.18}$$

As discussed in previous work on asymmetric bosonization, in diagonalizing H_{tot} care needs to be taken to preserve the algebra of the chiral fields encoded in the commutation relations of Eq. 4.7 (the so-called Kac-Moody algebra). This requires performing Bogoliubov trans-

formations between the R- and L-fields (see 2.4). However, given that this involves 4 fields, such transformations are very cumbersome. Instead, we use the trick of converting left-handed fields to right-handed fields via the transformation $\varphi_{L\alpha\sigma} \to i\varphi_{L\alpha\sigma}$, which then allows the application of standard matrix diagonalization. This is essentially the "*ict*" prescription used in special relativity to convert the Minkowski metric to a Euclidean metric [58].

This method makes it clear that the asymmetric dispersion simply shifts the values of the plasmon velocities but has no effect on the eigenvectors. To see this, note that Eq. 4.10 takes the form

$$H_0 = \frac{1}{4\pi} \int dx \; \partial_x \vec{\varphi}^T \left(\mathcal{H}_0 + \mathcal{H}_{int} \right) \partial_x \vec{\varphi}, \tag{4.19}$$

where $\vec{\varphi}^T = (\varphi_{R,1}, \varphi_{R,2}, ..., \varphi_{L,1}, \varphi_{L,2}, ...)$, $\mathcal{H}_0 = \text{diag}\,(v_R, v_R, ..., v_L, v_L, ...)$, and $\mathcal{H}_{int}$ is a bi-linear of the various densities $\rho_{R/L,a}$ incorporating the interaction terms. Now, after the transformation $\varphi_{L,a} \mapsto i\varphi_{L,a}$ we have $\mathcal{H}_0 \mapsto \mathcal{H}_0'$ with

$$\begin{aligned} \mathcal{H}_0' &= \text{diag}\,(v_R, v_R, ..., -v_L, -v_L) \\ &= \text{diag}\,(v, v, ..., -v, -v, ...) + \epsilon I \end{aligned} \tag{4.20}$$

where $v = (v_R + v_L)/2$, $\epsilon = (v_R - v_L)/2$, and I is the identity matrix. In this form it is clear that the asymmetry ϵ only enters as a constant shift in the eigenvalues and does not affect the eigenvectors. While this fact limits the role that the asymmetry plays in the bulk quantities (such as the tunneling density of states), the asymmetry can still play a crucial role in properties such as boundary and impurity scattering. An illustration of this physics is presented in Appendix D where tunneling into the ends of an asymmetric TLL is considered. Applying this method, we find that the resultant plasmon modes for the coupled charge sectors $c\pm$ move with four different velocities $v_{R/L,1/2} = \pm\epsilon + v_{1/2}$, where

$$v_{1/2} = \frac{v}{\sqrt{2} g_{c+}} \left[1 + g_{c+}^2 \pm \sqrt{\left(1 - g_{c+}^2\right)^2 + \left(\frac{2 g_{c+} \lambda}{\hbar v} \right)^2} \right]^{\frac{1}{2}}, \tag{4.21}$$

and $g_{c+} \equiv 1/\sqrt{1+4V/\pi\hbar v}$ is the standard TLL parameter. The spin sectors $s\pm$ each retain their band structure velocities $v_{R/L}$.

The effects of transverse fields on the low-energy nanotube physics, particularly in the band degree of freedom, are prominently manifested in physical observables. The tunneling density of states, a ubiquitous experimentally accessible quantity, retains its power-law form $\chi(E) \sim E^{\beta}$ with a modified exponent. Using standard procedures [8] that now account for field-dependent effects, we find that the tunneling exponent, to lowest order in λ, is given by

$$\beta_{r\alpha} = \frac{1}{8}\left(\frac{1}{g_{c+}} + g_{c+} - 2\right) - \frac{\lambda}{4\hbar v} r\alpha \left(\frac{1-g_{c+}}{1+g_{c+}}\right). \tag{4.22}$$

The first part of the exponent, also present in the field-free case, reflects the suppression in tunneling due to interactions (where g_{c+} is now tunable). The second part, which depends on the tunable coupling λ of $H_{\alpha FS,BE}$, further suppresses or enhances tunneling depending on the sign of $r\alpha$. As an estimate, for a $d = 6.78$ nm tube in a 6.4 T B-field and 0.02 V/nm E-field with a field-free value of $g_{c+} = 0.23$ (corresponding to a 1 μm-long tube), we have distinctly different exponents $\beta_{R+} = \beta_{L-} = 0.22$ and $\beta_{R-} = \beta_{L+} = 0.53$. The form of Eq. (4.22) reflects band (valley) selection; for example, a right-moving electron would preferentially tunnel into the $\alpha = +$ Fermi point for the field configuration shown in Fig. 5.1.

A physical consequence of transverse fields yielding such band-dependent exponents would be the presence of two different power-law contributions to the non-Ohmic conductance of the nanotube [59]. On a related note, the presence of an impurity would distinguish these exponents; conductance properties would be sensitive to whether or not an electron impinging on the impurity switched band index. Band-dependent effects similar to those in the density-of-states exponent would be manifest in any susceptibilities involving the sublattice degree of freedom.

4.2 Luttinger liquid phases

The Hamiltonian of Eq. 4.18 is a microscopic description of the field-induced physics whereas experiments (viz. transport measurements) probe long distance physics. How do we connect these two different regimes? Perhaps an even thornier theoretical challenge is the incompleteness of Eq. 4.18. There are a myriad of different terms which have been neglected, e.g. next-nearest-neighbor hopping, spin-dependent exchange effects, etc. Even if the coupling constants describing these terms are small, their effect may be important on long length scales.

The RG addresses both of these issues. For concreteness, consider a term in the action (or Hamiltonian) of the system

$$S_O = c \int dx dt \; \hat{O}, \tag{4.23}$$

where $\hat{O}$ is a generic operator with the long-distance correlation function

$$\langle \hat{O}^\dagger(x) \hat{O}(x') \rangle \sim \frac{1}{|x - x'|^{2\Delta}}. \tag{4.24}$$

We say that Δ is the *scaling dimension* of $\hat{O}$. In the bare action, the coupling constant c is a parameter which describes the short distance (or low-energy) physics, for example, at the scale of the lattice spacing a. The RG is a systematic procedure which 'integrates out' short distance physics incrementally, giving information about how $c(L)$ changes as the system is probed at different length scales. Quantitatively,

$$\frac{dc}{dL} = 2(1 - \Delta)c(L), \tag{4.25}$$

which is known as an RG flow equation [15]. If $\frac{dc}{dL} > 0$, then $\hat{O}$ is a *relevant* operator; if $\frac{dc}{dL} < 0$, $\hat{O}$ is said to be *irrelevant*. It is straightforward to read off the scaling dimension of an operator in bosonic form. This procedure parallels the steps used to derive Eq. 2.19. For

example, the intra-sublattice singlet pairing (SC0) operator takes the form

$$\hat{O}_{SDW0} \sim \sum_{p\alpha\sigma} \sigma \psi^{\dagger}_{p\alpha\sigma} \psi_{p-\alpha\sigma}. \tag{4.26}$$

Its bosonic form is given by [57]

$$\hat{O}_{SDW0} \sim \cos\left(\sqrt{\pi}\phi_{c+}\right) \cos\left(\sqrt{\pi}\theta_{c-}\right) \cos\left(\sqrt{\pi}\theta_{s+}\right) \sin\left(\sqrt{\pi}\phi_{s-}\right) - (\sin \leftrightarrow \cos)\,. \tag{4.27}$$

In general, θ_a will contribute a term proportional to g_a to the scaling dimension, whereas ϕ_a will contribute g_a^{-1}. Thus, the appearance of terms ϕ_{c+}, θ_{c-}, θ_{s+}, and ϕ_{s-} leads to a scaling dimension $\left(g_{c+}^{-1} + g_{c-} + 2\right)/4$ for $\hat{O}_{SDW0}$. In the non-interacting limit ($g_{c+} = 1$), this quantity reduces to 1, consistent with naïve dimensional analysis. The scaling dimensions of other operators of interest is given in table 4.1 [57].

According to the Mermin-Wagner theorem, 1D systems can not order [23]. However, the scaling dimension allows us to consider the relative importance of various relevant operators. The field-tuning of the TLL parameters discussed in the previous section offers a viable way of tuning the groundstate of the nanotube through different phases and altering the hierarchy of these ordering tendencies. In the absence of fields, Egger and Gogolin [57] performed an involved analysis using renormalization group arguments, refermionization and considerations of various susceptibilities to predict the ordering tendencies of the nanotube as a function of TLL parameters and temperature. In particular, in the 'TLL regime' which is the easiest to experimentally access, wherein all four sectors $c\pm$ and $s\pm$, remain ungapped, the prediction is that for the range of interaction values $g_{c+} > 1/5$, the system tends to show an inter-sublattice spin-density wave (SDWπ) ordering while for $g_{c+} < 1/5$ it tends to show inter-sublattice charge-density wave (CDWπ) ordering, where the corresponding operators

Table 4.1: Relevant nanotube operators and their scaling dimension for the case of a single electric or magnetic field.

Operator	Definition	Scaling dimension
$\hat{O}_{CDW\pi}$	$\sum_{p\alpha\sigma} \psi^\dagger_{p\alpha\sigma}\psi_{-p\pm\alpha\sigma}$	$(g_{c-}+g_{c+}+2)/4$
$\hat{O}_{SDW\pi}$	$\sum_{p\alpha\sigma} \sigma\psi^\dagger_{p\alpha\sigma}\psi_{-p\pm\alpha\sigma}$	$(g_{c-}+g_{c+}+2)/4$
$\hat{O}_{CDW0}$	$\sum_{p\alpha\sigma} \psi^\dagger_{p\alpha\sigma}\psi_{p-\alpha\sigma}$	$(g_{c-}+g_{c-}^{-1}+2)/4$
$\hat{O}_{SDW0}$	$\sum_{p\alpha\sigma} \sigma\psi^\dagger_{p\alpha\sigma}\psi_{p-\alpha\sigma}$	$(g_{c-}+g_{c-}^{-1}+2)/4$
$\hat{O}_{SC0}$	$\sum_{p\alpha\sigma} \sigma\psi_{p\alpha\sigma}\psi_{p-\alpha-\sigma}$	$(g_{c-}+g_{c+}^{-1}+2)/4$
$\hat{O}^2_{CDW\pi}$	see above	$g_{c-}+g_{c+}$
$\hat{O}^4_{CDW\pi}$	see above	$4g_{c+}$

are defined, respectively, as

$$\begin{aligned} \hat{O}_{CDW\pi} &\sim \sum_{p\alpha\sigma} \psi^\dagger_{p\alpha\sigma}\psi_{-p\pm\alpha\sigma}, \\ \hat{O}_{SDW\pi} &\sim \sum_{p\alpha\sigma} \sigma\psi^\dagger_{p\alpha\sigma}\psi_{-p\pm\alpha\sigma}. \end{aligned} \tag{4.28}$$

These analyses involved considering operators associated with certain orderings and determining the slowest decaying, equivalently, the most relevant operator (i.e., with the smallest scaling dimension). Table 4.1 gives a list of some of the operators that we consider in our analysis.

Here, we discuss the key changes that occur in the TLL regime in the presence of fields. We focus on the TLL liquid regime and consider the manner in which the field-tuned change in TLL parameters affect various susceptibilities. We do not take into account the effect of non-quadratic bosonic terms generated by the fields; even if relevant, we expect that the bare coupling associated with these terms is so small that they only come into play at very low temperatures and not in the TLL liquid regime.

Case of B = 0, E ≠ 0

For the case of only an electric field present, as discussed above, the effect of the field goes purely into changing the value of g_{c+}. Given that experimentally the value of g_{c+} is around and oftentimes higher than 1/5 and that the field tends to reduce the value of g_{c+}, the electric field provides a unique means of tuning from a tendency towards (SDWπ) ordering to that of (CDWπ) ordering.

Case of B ≠ 0, E = 0

The case of only a magnetic field present, as discussed above, presents a slightly more complex situation in which both g_{c+} and g_{c-} deviate from unity. As a result, various susceptibilities acquire a g_{c-} dependance in their scaling behavior. For instance, operators associated with intra-sublattice ordering such as $\hat{O}_{CDW0} \sim \sum_{p\alpha\sigma} \psi^{\dagger}_{p\alpha\sigma}\psi_{p-\alpha\sigma}$ and $\hat{O}_{SDW0} \sim \sum_{p\alpha\sigma} \sigma\psi^{\dagger}_{p\alpha\sigma}\psi_{p-\alpha\sigma}$, which in the absence of fields are marginal, both acquire a scaling dimension $(g_{c-}+g_{c-}^{-1}+2)/4$. Tendencies for superconducting order become weaker in the presence of fields; the singlet pairing operator $\hat{O}_{SC0} \sim \sum_{p\alpha\sigma} \sigma\psi_{p\alpha\sigma}\psi_{p-\alpha-\sigma}$ acquires the scaling dimension $(g_{c-}+g_{c+}^{-1}+2)/4$.

To determine which ordering dominates, we consider the most relevant candidates: the CDWπ and SDWπ operators, both of which have scaling dimension $(g_{c-}+g_{c+}+2)/4$; parts of the second order CDWπ operator denoted by $\hat{O}^2_{CDW\pi}$ that have scaling dimension $g_{c-}+g_{c+}$; and a fourth order CDWπ operator denoted by $\hat{O}^4_{CDW\pi}$ which has scaling dimensions $4g_{c+}$. Comparing these exponents shows that $\hat{O}_{CDW\pi}$ and $\hat{O}_{SDW\pi}$ are more relevant than $\hat{O}^4_{CDW\pi}$ for $15g_{c+} > 2 + g_{c-}$, a condition easier to satisfy in the presence of fields than in the field-free case since K_{c-} can then be less than 1. Now $\hat{O}^2_{CDW\pi}$ is more relevant than $\hat{O}^4_{CDW\pi}$ for $3g_{c+} > g_{c-}$. For $\hat{O}^2_{CDW\pi}$ to be more relevant than $\hat{O}_{CDW\pi}$ and $\hat{O}_{SDW\pi}$ requires $g_{c+} + g_{c-} < 2/3$, a condition requiring inaccessibly strong interactions. Finally, to determine whether $\hat{O}_{CDW\pi}$ or $\hat{O}_{SDW\pi}$ dominates, we appeal to the arguments of Ref. [57]; at lower temperatures where the physics is dominated by certain strong coupling fixed points, pinning of the θ_{s+} mode suppresses $\hat{O}_{CDW\pi}$, making its magnitude in the Luttinger phase smaller than that of

$\hat{O}_{SDW\pi}$. Though the methods of refermionization employed to reach this conclusion are no longer valid for arbitrary values of $g_{c-} \neq 1$, the strong coupling analysis still holds and we believe that a similar conclusion can be reached for the finite magnetic field situation.

Case of B $\neq$ 0, E $\neq$ 0

In the case of mutually orthogonal electric and magnetic fields, band-dependent effects would arise. For instance, charge density waves have contributions from operators $\hat{O}^{\pm}_{CDW\pi} \sim \sum_{r\alpha\sigma} r\psi^{\dagger}_{r\alpha\sigma}\psi_{-r\pm\alpha\sigma}$, reflecting like (+) and staggered (−) band correlations at A and B sublattice sites. While these operators both come on an equal footing in the field-free case, we find that fields render $\hat{O}^{-}_{CDW\pi}$ more relevant. To first order in λ, this operator acquires the scaling dimension

$$\Delta_{CDW\pi-} = \frac{3+g_{c+}}{4} - \frac{2g_{c+}}{1+g_{c+}}\frac{|\lambda|}{v}, \tag{4.29}$$

whereas the $\hat{O}^{+}_{CDW\pi}$ remains unaffected. Fields can thus discriminate between two types of band-dependent ordering at the sublattice level.

4.3 Coulomb Blockade

In the quantum dot limit achieved by high resistance contacts or sufficiently low temperatures, we find that transverse fields enable controlled tuning of Coulomb blockade physics and nanotube quantum states. Here, as in previous treatments [60, 61, 62], we describe the dot as a finite-sized version of the net nanotube Hamiltonian and focus on the topological sectors as relevant for standard quantum dot experiments involving adiabatic tuning. Field-induced interactions give rise to a Coulomb blockade structure in which the charge and band degrees of freedom are coupled. The coupling between the $c+$ and $c-$ sectors arises due to the the interaction $H_{\alpha FS,BE}$ (Eq. (4.16)) and the unusual form of the current operators. In particular, the charge current differs from the naïve form $J_{c+} = v_R\rho_{R,c+} - v_L\rho_{L,c+}$ due to $H_{\alpha FS,BE}$. The form of the current is easily derived by noting that the current J_a for every

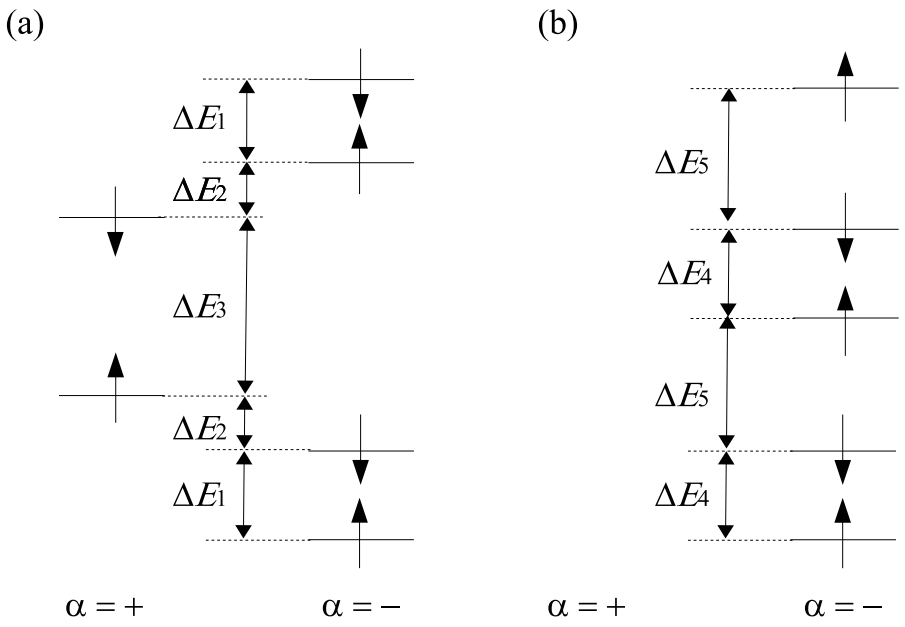

Figure 4.1: Examples of shell-filling. Figure indicates the order, α-point, and spin of tunneled electron with increasing chemical potential μ (not drawn to scale). **(a)** Filling order for a tube in the absence of fields and with $\Delta_b \neq 0$. The energy level spacings are given by $\Delta E_1 = E_{c+} + \Delta_b$, $\Delta E_2 = E_{c+}$, $\Delta E_3 = E_{c+} + \epsilon_0 - \Delta_b$ and exhibit a 4-fold periodicity. **(b)** Shell-filling for $N_{c+} = -N_{c-}$ exhibits 2-fold periodicity and complete polarization into band $\alpha = -$. This condition is approximately met for a 1 μm-tube of diameter 6.78 nm in the presence of magnetic and electric fields 4.93T and 0.0242 V/nm, respectively (see text for specific values of the Coulomb blockade parameters for this case and other details). The energy level spacings are given by $\Delta E_4 = E_{c+} + E_{c-} - 2\lambda_c - 2\Delta_z$ and $\Delta E_5 = E_{c+} + E_{c-} + \epsilon_0 - 2\lambda_c + 2\Delta_z$.

sector obeys a continuity equation $\partial_t \rho_a = -\partial_x J_a$. For the $c+$ sector, we obtain

$$\begin{aligned} \partial_t J_{c+} &= [H, \rho_{R,c+} + \rho_{L,c+}] , \\ &= -\partial_x \left(v_R \rho_{R,c+} - v_R \rho_{L,c-} + \lambda \rho_{c-} \right) , \end{aligned} \tag{4.30}$$

thus giving $J_{c+} = v_R \rho_{R,c+} - v_R \rho_{L,c-} + \lambda \rho_{c-}$. For $a = c-, s\pm$ we have $J_a = v_R \rho_{R,a} - v_L \rho_{L,a}$.

The Coulomb blockade Hamiltonian follows from requiring $\rho_{\alpha\sigma} \equiv \sum_r \rho_{r,\alpha\sigma} = N_{\alpha\sigma}/L$, where the $N_{\alpha\sigma}$'s are integers and the no-current condition $J_a = 0$. The channel occupation numbers are defined $N_{c\pm} = (N_{+\uparrow} + N_{+\downarrow}) \pm (N_{-\uparrow} + N_{-\downarrow})$ and $N_{s\pm} = (N_{+\uparrow} - N_{+\downarrow}) \pm$

$(N_{-\uparrow} - N_{-\downarrow})$. In the presence of a gate voltage V_G, the resulting Hamiltonian characterized by quantum numbers N_a for each channel is given by

$$H_T = \sum_{a=c/s\pm} \frac{\epsilon_a}{8} N_a^2 - \mu N_{c+} - \frac{\pi\lambda}{4L}\left(\frac{v_R - v_L}{v_R + v_L}\right) N_{c+}N_{c-} + \frac{1}{2}\Delta_b N_{c-} - \Delta_Z N_{s+}, \qquad (4.31)$$

where $\epsilon_a = \epsilon_0 + 4E_a$, $\epsilon_0 = \frac{2\pi\hbar v_R v_L}{L(v_R+v_L)}$ and E_a is the interaction strength in a given mode. Here, $E_{c+} = V/L$, $E_{c-} = -\pi\lambda^2/4\hbar v L$ and $E_{s\pm} = 0$. The term μ is proportional to eV_G, and $\Delta_Z = \mu_B B$ accounts for the Zeeman splitting. The band splitting Δ_b will depend on boundary conditions; in the absence of Fermi point mixing at the tube ends, it reduces to the band structure Fermi point mismatch Δ_F [63]. As typical parameter values, for a 1 μm-tube of diameter 6.78 nm, and magnetic and electric field strengths of 4.93 T and 0.0242 V/nm, we find $\epsilon_0 = 1.36$ meV, $E_{c+}/\epsilon_0 = 5.93$, $E_{c-}/\epsilon_0 = -0.23$, $\Delta_Z/\epsilon_0 = 0.21$, and $\lambda/L\epsilon_0 = 0.24$.

By virtue of their field dependence, several parameters in H_T can be varied to access a wide variety of shell filling configurations of the nanotube quantum dot in Coulomb blockade experiments. The configurations correspond to sets of electron occupation numbers which minimize the energy associated with Eq. (4.31) [60, 63]. While the associated parameter space is too extensive for an exhaustive study, a few salient characteristics of shell-filling are as follows. (i) In actual experiments [51, 50], the band degeneracy is often naturally broken due to physical attributes such as the confining potential created by the leads, yielding patterns such as in Fig. 4.1a. Here, the field dependence of Δ_b enables controlled tuning of band degeneracy breaking as well as probing the extent of Fermi point mixing at the tube ends [49, 63]. (ii) A four-fold periodicity has been observed in some experiments reflecting the band and spin degeneracy of the tube [50]. (iii) As a direct demonstration of band tuning, the parameter values quoted above yield the two-fold periodic shell-filling pattern in Fig. 4.1b. In particular, these values are chosen such that Eq. (4.31) is minimized by the condition $N_{c+} = N_{c-}$, entirely restricting the tunneling into a given α-point. We remark that this condition requires a fine-tuning of fields, and also that other field values can even

render ϵ_{c-} negative, resulting in an instability towards complete polarization into one band. (iv) Periodicity can also be entirely obliterated by choosing an irrational ratio between two of the relevant shell-filling parameters. As demonstrated above, transverse fields provide a precise means of preparing and manipulating the electronic spin and band quantum numbers of the nanotube quantum dot.

4.4 Conclusions and outlook

In this chapter we have presented transverse fields as powerful probes to access a rich range of TLL physics in armchair nanotubes. Fields induce novel interaction terms, most notably one which couples the charge and band sectors of the tube. Fields also have been shown to alter the ordering tendencies of electrons on the tube. These effects may be seen through transport properties, measurements of the T-DOS, and shell-filling patterns in Coulomb-blockaded tubes.

Chapter 5

Charge Fractionalization

5.1 Introduction

Charge fractionalization – the phenomenon in which excitations carry units of charge less than the electron – is a spectacular low-dimensional many-body effect. Such excitations may arise from topological considerations; for example, a half-integer charge is localized near a domain wall in chains with a Peierls instability [64]. Fractional charge has also been revealed in shot-noise experiments in the fractional quantum Hall effect (FQHE) [31].

As discussed in 2.5, TLL theory predicts that a momentum-resolved electron injected into the bulk will decompose into right- and left-moving quasiparticles of charge $f_{\pm} = \left(\frac{1\pm g}{2}\right) e$, respectively [65, 66]. Of particular interest is a recent experiment which claims to show evidence for fractionalization in a quantum wire [28]. In this three-terminal setup, the effects of fractionalization are inferred from the current asymmetry out of the wire. While the results are suggestive, the geometry of the setup, the nature of the coupling between the wire and the Fermi liquid leads, and the model-dependent way in which impurity scattering is accounted for raise questions regarding the interpretation of the experiment. For example, objections have been raised in [67] which point out that Andreev-like reflections at the end of the wire will always obscure DC signatures of fractionalization, a result reminiscent of earlier work on transport through TLLs [14, 65].

Such a measurement also raises important conceptual questions. Fractionalization is a consequence of the many-body wavefunction and is fundamentally different from quantum mechanical superpositions or classical stochastic processes. Nevertheless, both of these phe-

nomena may mimic certain aspects of fractionalization. It is thus interesting to ask whether a measurement can distinguish true fractionalization from quantum mechanical or classical probabilistic processes.

The goal of the present chapter is to explore charge fractionalization in a ring geometry. In contrast to electron-in-electron-out experiments, we consider DC measures obtained by weakly coupled probes to the ring, measurements in the so-called *weak continuous linear measurement* (CWLM) regime. In these measurements, the coupling of measuring apparatus to the system is much weaker than the intrinsic energy scale of the system and thus the signal must be acquired for some time [68]. Here, we show that the spatial distribution of such measurements taken at different points around the ring possesses quantitative signatures of electron fractionalization. Specifically, the non-invasive measurements considered are the time average of the field squared which can be measured by a superconducting quantum inteference device (SQUID) and the power induced by the field in a pickup loop (see Fig. 5.1). It is shown that these DC measurements also discern between fractionalization and quantum and classical uncertainties discussed above. We will also use certain characteristic features of the ring geometry – notably persistent currents and Coulomb blockade – to corroborate elements of these measurements.

The organization of this chapter is as follows. Section 5.2 introduces details of the relevant setup; here, the specific single-electron scenarios which are compared with charge fractionalization later in the chapter are also defined. A theoretical discussion of charge fractionalization in 5.3 sets the stage for a detailed analysis of the proposed measurements in 5.4. In 5.5, it is shown that the ground state properties of the ring also provide information on charge fractionalization. Experimentally motivated estimates are provided in 5.6. Finally, 5.7 presents our conclusions.

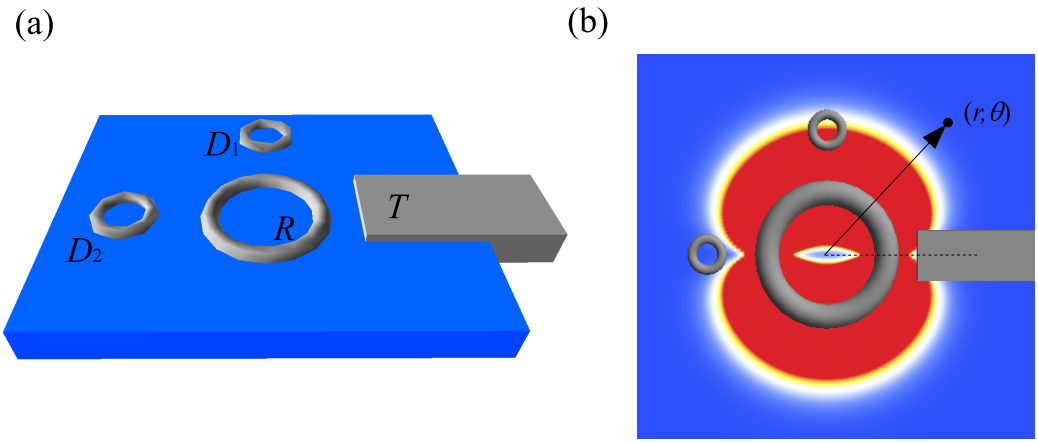

Figure 5.1: (a) Geometry of proposed experiment. A right-moving electron is injected into the ring from the tunnel junction T. According to Luttinger liquid theory, the electron decays into right- and left-moving quasiparticles. Two detectors (D_1 and D_2) probe the effects of the resulting magnetic field and its geometry. (b) A view of the setup and a superimposed plot of $\overline{\langle B^2 \rangle}_F$ (see 5.2 for notation) for a TLL with $g = 0.2$. The anisotropy of this quantity directly reveals the effects of fractionalization.

5.2 Setup and preliminaries

The setup of interest is shown in Fig. 5.1. In this chapter we consider spinless electrons. We use the notation introduced in 2.3 with some necessary modifications for the ring geometry. The index r will be co-opted to designate counterclockwise (CCW, $r = +$) and clockwise (CW, $r = -$ clockwise) directions. Let x denote the circumferential direction and $0 \leq x < 2\pi R$, where R is the radius of the ring. The ring geometry imposes periodic boundary conditions on electron operators such that $\psi(x + 2\pi R) = e^{i2\pi\Phi/\Phi_0}\psi(x)$ where Φ is the flux threading the ring and $\Phi_0 = h/e$. This requires the modification of Eq. 2.20:

$$\phi^0 = \phi_N + \sqrt{\pi}\left(J + \frac{2\Phi}{\Phi_0}\right). \tag{5.1}$$

This alteration has important implications for the ground state properties of the ring.

A momentum resolved electron is injected into a mesoscopic ring via a tunnel junction T. Measurements are made at points proximate to the ring. Effects of fractionalization are

probed by considering the spatial distribution of such quantities relative to the injection point T. In order to quantify the effects of fractionalization and distinguish them from other phenomena, three scenarios are considered in the context of the proposal.

The fractionalized state resulting from the tunneling of a CCW-moving electron having an initial wave function $\chi(x)$ above the TLL ground state, $|G\rangle_{LL}$, is given by

$$|F\rangle = \int \chi(x)\psi^{\dagger}(x)dx|G\rangle_{LL}. \tag{5.2}$$

A quantum superposition state, $|QS\rangle$, that mimics the fractionalized state would consist of superpositions of CW and CCW *electrons* excited above a non-interacting Fermi gas ground state $|G\rangle_0$, i.e.

$$|QS\rangle = \sum_{\pm} f_{\pm} \int \chi(x)\psi^{\dagger}_{\pm}(x)dx|G\rangle_0. \tag{5.3}$$

Third, a classical probabilistic situation of CW and CCW electrons excited in the non-interacting Fermi gas, denoted by the density matrix

$$\mathbf{M}_{\rho} = \sum_{\pm} f^2_{\pm}|\pm\rangle\langle\pm|, \tag{5.4}$$

where $|\pm\rangle = \int \chi(x)\psi^{\dagger}_{\pm}(x)dx|G\rangle_0$.

5.3 Charge Fractionalization

In this section, we consider three complementary ways of viewing charge fractionalization: from the bosonization identity, the Green's function, and the expectation value of the current in the ring.

The basic features of charge fractionalization may be gleaned by rewriting the creation

operator of a single electron in terms of the bosonic fields (via Eq. 2.6)

$$\psi_+^\dagger(x,t) \sim e^{-i\frac{\sqrt{\pi}}{2}[\cosh u\tilde{\varphi}_+(x,t)+\sinh u\tilde{\varphi}_-(x,t)]}. \tag{5.5}$$

Crucially, $\tilde{\varphi}_\pm(x,t) = \tilde{\varphi}_\pm(x\mp ut)$; thus $\tilde{\varphi}$ represents the freely propagating degrees of freedom. The total charge density $\rho = \partial_x\theta(x)/\sqrt{\pi}$; hence a local charge density is represented by a kink in the operator $\theta(x)$. Such kinks may be generated by the field ϕ since θ and $-\partial_x\phi$ are canonically conjugate variables. For instance, a unit charge at position x_0 is created by

$$e^{-i\sqrt{\pi}\int^{x_0} dx\partial_x\phi(x)} \sim e^{-i\sqrt{\pi}\phi(x_0)}, \tag{5.6}$$

which gives $\theta \to \theta - \sqrt{\pi}$ for $x < x_0$, and $\theta \to \theta$ otherwise. The coefficient of ϕ in the exponent thus gives the magnitude of the charge (a unit of charge corresponds to a change of θ by $\sqrt{\pi}$). In order to see what local charge density is created by the two terms in the argument of $\psi_+^\dagger$, we write them as

$$\begin{aligned} \cosh u\ \tilde{\varphi}_+ &= R_+\theta - Q_+\phi, \\ \sinh u\ \tilde{\varphi}_- &= R_-\theta - Q_-\phi. \end{aligned}$$

The coefficients of interest are $Q_+ = \cosh^2 u - \cosh u \sinh u$ and $Q_- = -\sinh^2 u + \cosh u \sinh u$. As argued above, these are the charges of the $r = \pm$ moving quasiparticles. We note that $Q_+ + Q_- = \cosh^2 u - \sinh^2 u = 1$, which is reassuring. For the interactions considered here, Eqs. 2.17 gives $f_\pm = Q_\pm = (1 \pm g)/2$.

The most direct (theorectical) manifestation of electron fractionalization is provided by the Green's function $\mathcal{G}(x,t) = \langle T\psi_+(x,t)\psi_+^\dagger(0,0)\rangle$, given by

$$\mathcal{G}(x,t) \sim \left(\sin\pi\frac{x-ut}{L}\right)^{-\frac{1}{4}(g+1/g)^2} \left(\sin\pi\frac{x+ut}{L}\right)^{-\frac{1}{4}(g-1/g)^2}. \tag{5.7}$$

This quantity is discussed in 2.4 as well as Appendices A and B.

Charge fractionalization is also revealed in certain expectation values. For instance, the expectation value of the current $I(x,t) = \langle \hat{I} \rangle_F \equiv \langle F|\hat{I}(x,t)|F\rangle$ given by

$$I(x,t) = \frac{eu}{4\pi R}\left[(1+g)|\chi(x-ut)|^2 + (1-g)|\chi(x+ut)|^2\right], \tag{5.8}$$

which explicitly shows the decomposition of the electron into two quasiparticles of charge $(1 \pm g)e/2$. This expression is readily obtained from the commutation relation

$$[\psi_+(x'), \partial_x \varphi_\pm(x)] = \pm\left(\frac{1 \pm g}{2}\right)\delta_p(x - x' \mp ut)\psi_+(x'), \tag{5.9}$$

the bosonization identity Eq. 2.6 and the Campbell-Baker-Hausdorf identity [69] (see Appendix A).

5.4 Proposed Measurements

The magnetic field produced by the counter-propagating charges can be evaluated by using the Biot-Savart law to define the magnetic field operator at position $\mathbf{r}$ as

$$\hat{\mathbf{B}} = \frac{\mu_0}{4\pi}\int d\ell\ \hat{\mathbf{I}}(\ell) \times \mathbf{r}/|\mathbf{r}|^3, \tag{5.10}$$

where μ_0 is permeability of free space [41]. At any given point having polar coordinates (r,θ) in the plane of the ring, where the origin is at the ring's center and the electron is inserted at $(R,0)$, the current in Eq. 5.8 produces a field perpendicular to the plane (refer to Fig. 5.1). For the case of χ having a spread much smaller than the ring diameter, the z-component of the field takes the form

$$\langle \hat{B}_z \rangle_F = \frac{\mu_0 e\omega}{2R}\left[f_+ h(t) - f_- h(-t)\right], \tag{5.11}$$

where $\omega = u/R$ and $h(t) = (1 - a(t))/(\frac{r^2}{R^2} - 2a(t) + 1)^{3/2}, a(t) = r\cos(\omega t - \theta)/R$. In principle, a time-resolved measurement of the magnetic field, as with other quantities such as the conductance, would yield information on fractionalization. Of interest here are low-frequency or time averaged signatures. Although the tunneling of the electron picks out a specific point on the ring, signatures are effaced by time-averaging any quantity that is linear in the ring current. For example, $\overline{\langle B_z \rangle}$ shows an isotropic spatial profile (the overline denotes a time average).

We focus on quadratic measures of the current which can be obtained from a CWLM via inductive coupling to the ring [68]. Such measurements are in a regime in which the coupling is small compared to intrinsic energy scales of the ring (weak, linear) and the signal is integrated over a finite time (continuous). It is clear that in such a scheme signal-to-noise considerations are extremely important and limit the accuracy of any such measurement, as we now show (we follow the discussion presented in [70]). Suppose that a quantity $\langle \hat{Q} \rangle$ is averaged over some period of time. This measurement has noise arising both from environmental and internal sources as well as from the quantum mechanical uncertainty associated with $\hat{Q}$. This noise can be characterized by $\mathcal{S}(\omega) = \int dt\ e^{-i\omega t} \langle \hat{Q}(0)\hat{Q}(t) \rangle$. For a measurement of accuracy ΔQ, the quantity $\langle \hat{Q} \rangle$ must be acquired and averaged for a minimum measurement time $\tau_m \sim \mathcal{S}(0)/\left(\Delta Q\right)^2$.

Naturally, quantum fluctuations may be so large as to render a measurement of $\hat{Q}$ vacuous. This is of particular concern in the present context. In particular, the gaplessness of the TLL could lead to dangerously large fluctuations in the quasiparticle charge or current which makes the measurements proposed here useless. Similar questions have been discussed in the literature. For example, in [71] it is argued that fractionally charged quasiparticles in a TLL are 'sharp' and that the magnitude of fluctuations is exactly what it would be in the ground state (vacuum). Translated to our setting, we expect fluctuations in the magnetic field to be induced even by the quiescent TLL ring (having no extra tunneled electron) and identical to those induced by the fractionalized state $|F\rangle$. This fact will be demonstrated

below.

We now turn to a quantitative discussion of the effect of fractionalization on the proposed measurements. We first consider $S(r,\theta) = \overline{\langle \hat{B}_z^2 \rangle}$, which can be accessed by a SQUID-based detector biased to a minimum of its I-V characteristic curve. The second is the average power received by a detector, for example, an ultra-sensitive bolometer. For a small conducting detector (ignoring the local spatial variations in the magnetic field), this is given by $P(r,\theta) = \overline{\langle \partial_t \hat{B}_z \rangle^2}$. Crucially, note that S involves a quantum average of a quadratic operator and that P is related to the quantum mechanical average of a linear operator.

The forms of the moments S and P can be evaluated by taking appropriate quantum expectations ($\langle\rangle$) and time averages (overline). Considering the time-average of equal time correlators, we have

$$\begin{aligned} S = \overline{\langle B^2(t) \rangle}_F &= \int dy\ |\chi(y)|^2 \left[f h(y+ut) - (1-f) h(y-ut) \right]^2 + \overline{\langle B^2(t) \rangle}_G \\ &\approx \overline{\langle B(t) \rangle_F^2} + \overline{\langle B^2(t) \rangle}_G, \end{aligned} \tag{5.12}$$

where the approximation made in the last line is good if χ's spatial extent is much smaller than R. Given that the quantum mechanical expectation obeys $\langle B^2 \rangle_F - \langle B \rangle_F^2 = \langle B^2(t) \rangle_G$, it is clear that the fluctuations in this measurement are due only to vacuum fluctuations in the ground state. In this sense, the fractional charges are sharp [71]. An explicit expression for S is now given by

$$\overline{\langle B^2(t) \rangle_F} = \left(\frac{\mu_0 e \omega}{2R} \right)^2 \left[(1+g^2) \overline{h^2(t)} - (1-g^2) \overline{h(t) h(-t)} \right]. \tag{5.13}$$

A similar form for $\tilde{P} \equiv P/\omega^2$ with $h(t)$ replaced by its time derivative $h'(t)$. The quantities

$$\overline{h^2(t)} = \frac{2R^6 + R^4 r^2}{2(r^2 - R^2)^3}, \tag{5.14}$$

$$\overline{h'^2(t)} = \frac{R^4 r^2 (4r^4 + 25 r^2 R^2 + 16 R^4)}{8(r^2 - R^2)^5}, \tag{5.15}$$

with $r = \sqrt{x^2 + y^2}$ are manifestly isotropic, whereas $\overline{h(t)h(-t)}$ is anisotropic.

Information on fractionalization is best obtained by decomposing S/P as

$$S/\tilde{P}(r,\theta) = \left(\frac{\mu_0 e\omega}{2R}\right)^2 \sum_{m=0}^{\infty} A_m^{S/P}(r)\cos 2m\theta. \tag{5.16}$$

The plots of these quantities (as shown in Fig. 5.2) capture our central result that higher moments of the current and of the magnetic field profile (in our case, S and P) reflect, in their rotational symmetry broken distributions, the concurrent motion of fractionalized charges. From Eq. 5.13 it is clear that $A_{m\neq 0}^{S/P}$ scales as $1-g^2$. This distribution is reflected in the plots of Fig. 5.2 and also agrees with the rotationally symmetric non-interacting limit ($g = 1$). The bilateral symmetry of the plots reflects the two charge components moving away from the injection point and towards the diametrically opposite point. That these two special points exist for any arbitrary closed shape suggests that the features of these plots is robust against small deformations in the shape of ring.

We contrast the behavior of the moments S and P in the fractionalized state to the quantum and classical probabilistic situations. In the quantum state $|\Omega\rangle_{QS}$, a superposition of CW and CCW moving electrons, quantum averages of higher moments mimic charge fractionalization while those of linear operators do not. To see this, note

$$\langle B(t)B(t')\rangle_{QS} = \int dy|\chi(y)|^2\left[f'h^2(y+ut) - (1-f')h^2(y-ut)\right] + \langle B(t)B(t')\rangle_G. \tag{5.17}$$

In contrast, the quantity P cannot differentiate between $|F\rangle$ and $|QS\rangle$ because $\langle\partial_t B(t)\rangle_F = \langle\partial_t B(t)\rangle_{QS}$. Thus, $S = \overline{\langle B_z^2\rangle}$ shows an anisotropic profile similar to that of Fig. 5.2a but $P = \overline{\langle\partial_t B_z\rangle^2}$ is isotropic. For the classical situation described by the density matrix $\mathbf{M}_\rho$, the moments are evaluated by separately considering CW and CCW electrons and adding their appropriately weighted contributions. Since these contributions are isotropic, both S and P yield isotropic profiles (see Table 5.1).

5.5 Ground state properties

As will be discussed in 5.6, the plasmons which encode the fractionalized charge have a finite lifetime. The groundstate sector is attained after sufficiently long times and and corresponds to complete delocalization of the electron around the ring and to the Coulomb blockade regime: only the zero modes of $\varphi_\pm$ play a role. These modes, taken to be c-numbers, are given by $N = \sum_r n_r$ (number of excess electrons) and $J = \sum_r r n_r$, where J is proportional to the persistent current in the ring, where we define $n_r = -r\Phi/\Phi_0 + \int dx\ \rho_r$. The ground state Hamiltonian is obtained by considering the zero mode contribution to H_{LL} and is given by

$$H_{NJ} = \frac{\pi\hbar u}{4\pi R}\left[\frac{1}{g}N^2 + g\left(J + \frac{2\Phi}{\Phi_0}\right)^2\right] - \mu N. \tag{5.18}$$

This expression includes a tunable chemical potential μ and external flux Φ. As a function of these two quantities, the ring exhibits Coulomb blockade peaks depending on the favored values of N and J. As shown in the diagram of Fig. 5.3 derived by finding energy minima for H_{NJ}, in the non-interacting case ($g = 1$), the favored regions form diamonds in μ-Φ parameter space while with interactions the regions form hexagons with horizontal sides of length $1-g^2$ [25]. We highlight this diagram in that it provides an easily accessible, alternate means of extraction of the TLL parameter.

A highlight of this slow-time regime is that it offers another route to distinguishing the fractionalized state $|F\rangle$ by way of persistent current analysis. Ultimately this state is associated with a CW electron and hence has the fixed current value $J = +1$ while the quantum and classical states characterized by $|QS\rangle$ and $\mathbf{M}_\rho$ involve CW and CCW electrons, thus showing values $J = \pm 1$ which vary between measurements. In Table 5.1, we have summarized the measurements and their ability to distinguish fractionalization from the other scenarios presented. In particular, if P is measured, the state $|QS\rangle$ and $|F\rangle$ cannot be distinguished without also performing a measurement of the persistent current in the

Table 5.1: Summary of measurements which allow 'true' fractionalization to be distinguished from quantum superpositions and probalistic tunneling. S and P can have isotropic (I) or anisotropic (AI) distributions. Persistent current measurements can be variable (V) meaning that the results vary over repeated injection events, or not variable (NV).

	$\|F\rangle$	$\|QS\rangle$	M_ρ
$S(r,\theta) = \langle B_z^2 \rangle$	AI	I	I
$P(r,\theta) = \langle \partial_t B_z \rangle^2$	AI	AI	I
persistent current	NV	V	V

ring.

5.6 Experimental Considerations

Due to coupling to the environment (including the back action of the detector), the plasmonic modes have a finite lifetime. Employing a Caldeira-Leggett calculation (for example), we can (in principle) estimate the decoherence time τ_d within which measurements need to be performed [72]. This quantity must satisfy $\tau_d \gtrsim \tau_m$ (see 5.4).

Finally, to provide relevant estimates for experiments, for $R \approx 1$ μm and $\omega \approx 10^{11}$ Hz, we have $(\mu_0 e\omega/2R)^2 \approx (0.1 \text{ milligauss})^2$ and $(\mu_0 e\omega^2/2R)^2 \approx (80 \text{ T/sec})^2$. Momentum-resolved injection of electrons into the ring can be accomplished by a magnetic field perpendicular B_{ext} to the ring such that $\hbar k_F = eB_{ext}d$. An important requirement is that the injection of an electron must be made on a timescale $\tau_T \ll 1/\omega$ in order for the injection to be 'clean' (crucial to the contrast of the signals in S/P). For a ring, we have $\tau_T = R_T C$ where R_T is the tunnel junction resistance and C is the ring capacitance (which we estimate to be $C \sim \epsilon_0 R \sim 10^{-17}$ F for a micron-sized ring). This gives the requirement that $R_T \ll 1$ MΩ. On the other hand, the Coulomb blockade limit holds only if $R_T \gg \frac{h}{e^2} = 26$ kΩ. Thus, we need a $R_T \sim 100$ kΩ. These estimates are very much within the reach of current nanotechnology.

5.7 Summary

We have presented an alternative to the electron-in electron-out type of experiment to test charge fractionalization in a mesoscopic ring. We find that weak measurements of a mesoscopic ring via inductively coupled detectors provides quantitative evidence for charge fractionalization. The setup envisioned here allows for a clear demonstration of charge fractionalization and allows it to be distinguished from qualitatively similar phenomena such as quantum superpositions and classical noise. An important extension of this work would be to consider the role that spin plays.

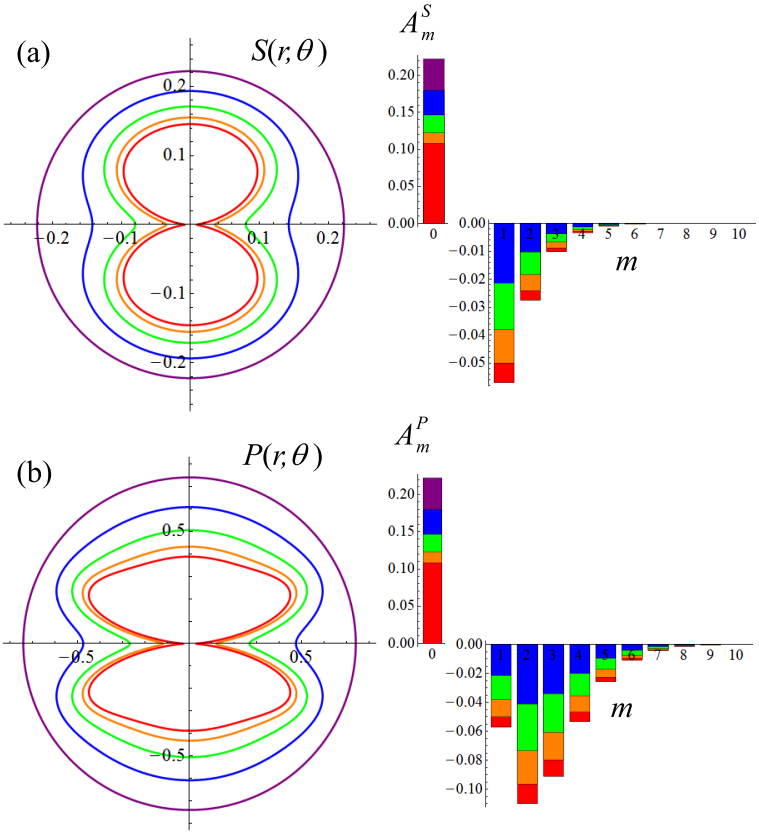

Figure 5.2: Polar plot showing the angular dependence of the quantities (a) $\overline{\langle B^2(t)\rangle}$ and (b) $\overline{\langle \partial_t B(t)\rangle^2}$ at a distance $r = 2R$ for values of the Luttinger parameter ($g = 1.0,\ 0.8,\ 0.6,\ 0.4,$ and 0.2 from the outside in) as a function of θ. The scale of the graph has no dimensions; it is a plot of the dimensionless part of Eq. 5.16. The right-hand sides of (a) and (b) are graphs of the spectral weight of the corresponding maps showing the even Fourier coefficients (i.e., the height of the columns 0, 1, 2 show the weight of the coefficient of the zeroth, $\cos 2\theta$, and $\cos 4\theta$). Note that while the zero mode decreases with increased fractionalization (decreasing g), (the non-zero modes are enhanced exhibiting the $1-g^2$ behavior illustrated in the notes). Also, note that the zero and non-zero modes are shown on a different scale.

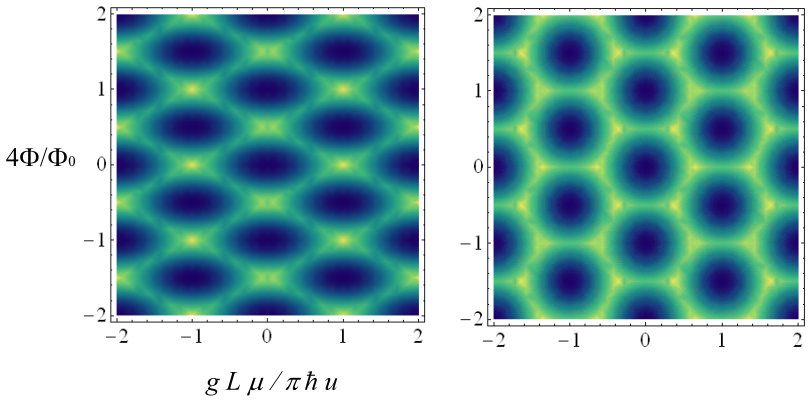

Figure 5.3: Ground state structure of H_{NJ}, Eq. 5.18. Each cell corresponds to a given electron number (N) and persistent current (J) which optimizes H_{NJ} as a function of chemical potential (horizontal axis) and magnetic flux (vertical) for (a) $g = 1$ (non-interacting system) and (b) $g = 1/2$. Bright lines indicate a transition in which J or J and N change by 1.

Chapter 6

Spin Chains, Topological Phases and Majorana Fermions

6.1 Introduction

The notion of *topological order* has emerged as a powerful paradigm for the classification and discovery of novel phases of matter. A flurry of interest in topological insulators and superconductors has recently emerged. Although these materials possess a bulk gap, they are characterized by 'protected' end or gapless edge modes . In pioneering work, Kitaev proposed a model of a 1D spinless p-wave superconductor which exhibits Majorana modes at its ends [73]. Any Dirac fermion f may be written in terms of Majorana fermions a and b, with $f = a + ib$. Thus, a Majorana is a fermion which is its own antiparticle, i.e. $a^\dagger = a$.

The topologically non-trivial phase of the p-wave superconductor is characterized by the presence of (an odd number of) of zero energy Majorana modes at the ends of an infinitely long system having open boundary conditions; kinetic energy and superconducting pairing conspire to split a Dirac fermion into its 'real' and 'imaginary' parts. Once only a speculative candidate for the neutrino, Majorana fermions are currently the focus of intense study in condensed matter physics [5]. Such interest is motivated, in part, by the realization that Majorana particles encode nonlocal quantum information which may be to immune to certain types of environmental noise [3]. A robust means of preserving quantum states is an essential ingredient for a quantum computer.

It has long been appreciated that 1D fermionic systems can be mapped to spin chain systems [43]. The study of spin systems thus provides a different window into topological order in fermionic systems. In this chapter we show that topologically non-trivial phases in

the fermionic system may be associated with a symmetry-broken phases in the spin systems, and the trivial phases with paramagnetic phases. As observed in [74, 75], we find that the presence of isolated Majorana modes at the ends of a long system with open boundary conditions is intimately related to spontaneous breaking of a global $\mathbb{Z}_2$ symmetry. This observation leads to a general demonstration of the relationship between spontaneous broken symmetry in a spin system and Majorana modes in the corresponding fermion system.

This short chapter serves as an introduction for the remainder of the thesis in which we focus on models of fermionic systems that exhibit non-trivial topology. In 6.2, the model of a 1D p-wave superconductor is introduced. The mapping between the XY chain and the 1D p-wave superconductor is presented in 6.3. The connection between the topological phase (in the fermionic system) and spontaneous symmetry breaking (in the spin chain) is established in 6.4. Finally, a brief summary of this discussion is given 6.5.

6.2 The 1D p-wave superconductor

The 1D p-wave superconducting system of spinless fermions explored by Kitaev [73] is described by the tight-binding Hamiltonian

$$H = \sum_n \left[-w \left(f_n^\dagger f_{n+1} + f_{n+1}^\dagger f_n \right) + \Delta \left(f_n f_{n+1} + f_{n+1}^\dagger f_n^\dagger \right) - \mu \left(f_n^\dagger f_n - 1/2 \right) \right], \tag{6.1}$$

where w is the nearest-neighbor hopping amplitude, Δ the superconducting gap function (assumed real), and μ the on-site chemical potential. Here, "p-wave" means that in k-space, the superconductivity term goes like $\sin k$.

The translationally invariant system can be diagonalized in the momentum basis, $f_k = \frac{1}{\sqrt{N}} \sum_n f_n e^{-ikn}$ and can be shown to have the particle-hole symmetric dispersion

$$\omega_k = \pm \sqrt{(2w \cos k + \mu)^2 + 4\Delta^2 \sin^2 k}. \tag{6.2}$$

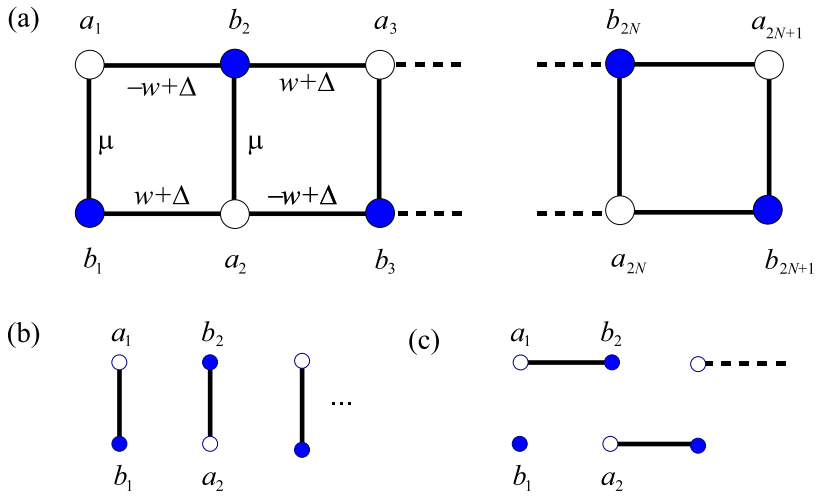

Figure 6.1: Cartoon showing the couplings between Majorana fermions described by the Hamiltonian in equation (6.3) for the cases of (a) general couplings, (b) the strong (intra-site) pairing limit $\Delta = w = 0$, $\mu \neq 0$ which does not possess Majorana modes (topologically trivial), and (c) the weak pairing limit $\Delta = -w$, $\mu = 0$ which hosts Majorana modes at the ends (topologically non-trivial).

As shown in Fig. 6.2, the system hosts distinct phases depending on the parameter $|\mu|/2w$; the system is gapped save for the regions demarcating the phase boundaries. The weak (*intra*-site) pairing phase $|\mu|/2w < 1$ (phases I and II in Fig. 6.2) is topologically non-trivial while the strong pairing phase (phases III and IV) is topologically trivial.

Topologically trivial versus non-trivial phases are distinguished by the absence versus presence of boundary Majorana modes, which can be visualized in a simple fashion in the extreme strong and weak pairing limits as follows. Consider decomposing the Dirac f-fermion above in terms of two Majorana fermions $f_n = (a_n + ib_n)/2$, where the Majorana fermions respect the relations $a_n^2 = b_n^2 = 1$, $\{a_n, a_m\} = \{b_n, b_m\} = 2\delta_{m,n}$, $\{a_n, b_m\} = 0$. In terms of the Majorana fermions, the Hamiltonian in Eq. (6.1) becomes

$$H = \frac{i}{2} \sum_n \left[(-w + \Delta)\, a_n b_{n+1} + (w + \Delta)\, b_n a_{n+1} - \mu a_n b_n \right], \tag{6.3}$$

as represented in Fig. 6.1a.

In the extreme weak pairing limit $\Delta = w > 0$, $\mu = 0$, Majorana fermions at adjacent sites are coupled leading to the staggered pattern shown in Fig. 6.1c. A change in sign of Δ corresponds to shifting the staggered pattern by a lattice site, thus exchanging the roles of the a and b fermions. The superconductivity induced anomalous term and the normal hopping term conspire to separate a Dirac fermion into its Majorana components, leaving an isolated Majorana mode at each end. In this limit, Eq. 6.1 decouples into the form $\sum_{n=1}^{N-1}(w+\Delta)(\tilde{f}_n^\dagger \tilde{f}_n - 1/2)$, where $\tilde{f}_n = (a_n + ib_{n+1})/2$ corresponds to Dirac fermions composed of the pairs of linked Majorana fermions depicted in Fig. 6.1c. Conspicuously absent from this Hamiltonian are the Majorana fermions b_1 and a_N. They thus form a zero energy Dirac state [73]. In the extreme strong pairing limit $\Delta = w = 0$, $\mu \neq 0$, the Majorana fermions a_n and b_n are pairwise connected as shown in Fig. 6.1b; thus no Majorana fermions are isolated.

The presence of an energy gap in each phase ensures that slightly changing the couplings from these extreme limits does not alter these topological aspects. In the weak pairing phase, it is thus still possible to define appropriate linear combinations $Q_L = \sum \alpha_n a_n$ and $Q_R = \sum \beta_n b_n$ (with α_n and β_n real) that are Majorana modes bound to the two ends of the system and that become isolated in the thermodynamic limit.

It is worthwhile at this point to emphasize that the isolation of Majorana modes requires effectively spinless electrons. If spinful electrons were considered, then the above analysis would hold for both spin up and spin down electrons. The zero energy states considered here would thus consist of two Majorana fermions and the corresponding state would be topologically trivial.

6.3 Mapping spin chains to a p-wave superconductor

The concepts discussed above can be investigated in the context of spin chain physics. As an example, consider the extensively studied spin-1/2 XY chain subject to a transverse

magnetic field [76, 77, 78]. The Hamiltonian is given by

$$H = -\sum_{n=1}^{N-1} \left(J_x \sigma_n^x \sigma_{n+1}^x + J_y \sigma_n^y \sigma_{n+1}^y \right) - h \sum_{n=1}^{N} \sigma_n^z, \tag{6.4}$$

where σ_n^α denote the Pauli matrices. The spin-1/2 operators can be mapped to Majorana fermions using the Jordan-Wigner transformation [76, 79] (see 2.4): $a_n = \prod_{j=1}^{n-1} \sigma_j^z \ \sigma_n^x, b_n = \prod_{j=1}^{n-1} \sigma_j^z \ \sigma_n^y$, for $2 \leq n \leq N$, $a_1 = \sigma_1^x$ and $b_1 = \sigma_1^y$. The resultant Hamiltonian exactly maps to the 1D p-wave superconductor Majorana Hamiltonian of equation (6.3) with the identification $w \leftrightarrow J_x + J_y, \Delta \leftrightarrow J_y - J_x, \ \mu \leftrightarrow 2h$, and with the interchange of a_n and b_n on even sites. Hence, Fig. 6.2 also represents the phase diagram for the spin system. Phases I and II are ferromagnetic and have non-zero ground state expectation values of σ_n^x and σ_n^y, respectively. Phases III and IV are paramagnetic with both σ_n^x and σ_n^y having zero expectation values in the ground state. The extreme limits shown in Fig. 6.1 can be understood in terms of spin physics. The case of Fig. 6.1c corresponds to the values of the couplings $J_x \neq 0, J_y = 0, h = 0$ and thus to an Ising-type ferromagnetic (or antiferromagnetic) ground state along the x-axis. The case of Fig. 6.1b corresponds to $J_x = 0, J_y = 0, h \neq 0$ and thus to spins polarized along the z direction.

6.4 Spontaneous symmetry breaking and isolated Majorana modes

As discussed above, the topologically non-trivial phases in the p-wave superconductor map onto the ferromagnetic phases in the spin chain. Here we demonstrate that the presence of these isolated fermions corresponds to a spontaneously broken $\mathbb{Z}_2$ symmetry phase in the spin system. As is obvious in the extreme limit of figure 6.1c, the energetics in phases I and II provides $N - 1$ constraints for a system of N spins. Hence, the ground state is constrained to two degenerate states reflecting a $\mathbb{Z}_2$ symmetry (reduced from the full $SU(2)$

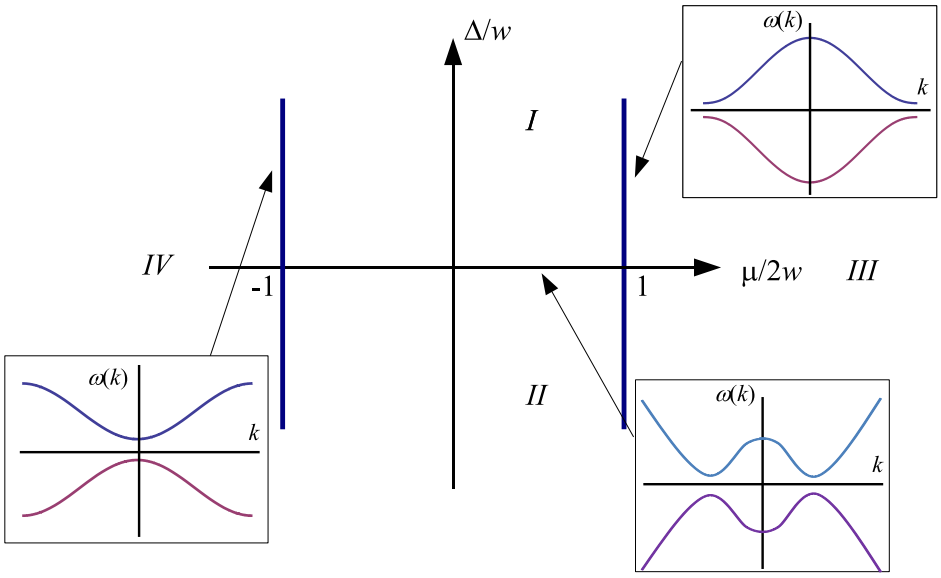

Figure 6.2: Zero temperature phase diagram of the 1D p-wave superconducting fermionic system as well as the spin-1/2 XY chain in a transverse magnetic field. Phases I and II denote topologically non-trivial/ferromagnetic phases while phases III and IV denote topological trivial/paramagnetic phases. Inset: Dispersion relations near various gap closures at phase boundaries.

symmetry since we have chosen Δ to be real). In the fermionic language, the degeneracy is associated with the isolated modes $Q_A = \sum \alpha_n a_n$ and $Q_B = \sum \beta_n b_n$ which do not participate in the energetics. Explicitly, the Dirac fermion formed by the two boundary Majorana fermions, $\Psi = (Q_A + iQ_B)/2$ can have occupation number 0 or 1. Thus, picking one of the corresponding degenerate states $|0\rangle_\Psi$ or $|1\rangle_\Psi$ (or any linear combination $u|0\rangle_\Psi + v|1\rangle_\Psi$) amounts to breaking the $\mathbb{Z}_2$ symmetry of the ground state and picking one of the two energetically available spin configurations. In phases III and IV, however, energetics poses N constraints and the system is confined to a unique ground state.

To explore the spin physics in the symmetry broken phase in terms of the isolated Majorana modes, consider the spin-1/2 algebra formed by $\{Q_A, Q_B, -iQ_AQ_B\} \to \{\sigma_x, \sigma_y, \sigma_z\}$, where $iQ_AQ_B = 2\Psi^\dagger\Psi - 1$. The two eigenstates of any of these operators (those of the $-iQ_AQ_B$ being $|0\rangle_\Psi$ and $|1\rangle_\Psi$) are orthogonal to one another and are each equally valid configurations of the ground state. The particular symmetry broken choice immediately

determines the expectation values of these operators and their corresponding Majorana and spin operators. Specifically, if we consider the two eigenstates of Q_A, $|\psi_\pm\rangle_A$, we can use the relationship $\{Q_A, a_n\} = 2\alpha_n$ to show that $\langle\psi_+|a_n|\psi_+\rangle_A = \alpha_n$ and $\langle\psi_-|a_n|\psi_-\rangle_A = -\alpha_n$ for all n. Furthermore, since $\{Q_A, b_n\} = 0$, we see that $\langle\psi_\pm|b_n|\psi_\pm\rangle_A = 0$ for all n. For instance, in the limiting case $J_x > |J_y|$ and $h = 0$ the system is in the Ising-type phase whose possible degenerate ground states correspond to spins that are aligned in either $\pm\hat{x}$ directions. In fact, $|\psi_\pm\rangle_A$ are these two states. Given that σ_1^x is identically a_1, we can easily evaluate its expectation value in one of the states to get $\langle\psi_+|\sigma_1^x|\psi_+\rangle_A = \sqrt{1-(J_y/J_x)^2}$, as ought to be true for the system pointing primarily along $\hat{x}$. This result can be compared to that of Lieb, Schultz and Mattis [76]. It is shown in reference [76] that, for an open chain with N sites (where N is even and $\to \infty$) in a case which is effectively that of the Ising limit above, the end-to-end two-point correlation functions are given by $\langle\psi_+|\sigma_1^x\sigma_N^x|\psi_+\rangle = 1-(J_y/J_x)^2$ and $\langle\psi_+|\sigma_1^y\sigma_N^y|\psi_+\rangle = 0$. In the limit $N \to \infty$, we expect clustering to hold, so that $|\langle\psi_+|\sigma_1^x|\psi_+\rangle| = |\langle\psi_+|\sigma_1^x\sigma_N^x|\psi_+\rangle|^{1/2}$. We therefore find complete agreement with the results in [76]. We note that our derivation is much simpler than the one in [76], purely making use of the end Majorana modes.

The expectation value $|\langle\psi_+|\sigma_1^x|\psi_+\rangle|$ may be obtained for the case of non-zero h by the methods developed in the next chapter (see 7.3.1, in particular). One obtains the exact result

$$\langle\sigma_1^x\rangle = \alpha_1 = \pm\sqrt{\frac{\left(1-\frac{J_y}{J_x}\right)\left(\left(1+\frac{J_y}{J_x}\right)^2-\frac{h^2}{J_x^2}\right)}{\left(1+\frac{J_y}{J_x}\right)\left(1-h^2\left(2-\frac{J_y}{J_x}-\frac{J_y^2}{J_x^2}\right)\right)}}. \tag{6.5}$$

This expression vanishes at the phase boundaries $J_x \to J_y$ and $J_x + J_y \to h$. It is instructive to compare this result to the corresponding bulk quantitiy derived in [78]:

$$\langle\sigma_{bulk}^x\rangle = \left[\left(1-\left(\frac{J_y}{J_x}\right)^2\right)^2 - \left(1-\frac{J_y}{J_x}\right)^2\left(\frac{h}{J_x}\right)^2\right]^{1/4}. \tag{6.6}$$

A little algebra reveals that $|\langle\sigma_{bulk}^x\rangle| \geq |\langle\sigma_1^x\rangle|$. In this sense, bulk spins are more 'resistant'

to the effects of a perpendicular magnetic field in the symmetry broken phase. This is not surprising given that these spins are energetically more constrained by their neighbors than spins at the end of the system.

6.5 Summary and Outlook

In this section we discussed a model of a 1D p-wave superconductor which admits topologically non-trivial phases characterized by Majorana fermions. It was found that the corresponding spin-chain system gave a new way of looking at the topological phase. In particular, the topological phase corresponds to a spontaneously broken symmetry phase in the spin system. This intuition will be invaluable in the next chapter in which we consider this physics in a more general setting.

Chapter 7

Kitaev Ladder

7.1 Introduction

In the previous chapter we found that the mapping between fermionic and spin systems provides a powerful way to explore topological phases. In this chapter, we consider a spin ladder whose couplings form a two-legged version of Kitaev's celebrated honeycomb model [80]. This model has been the focus of intense research for its topological properties [74, 75, 81, 37, 82, 83, 84, 85]. Of particular interest here is the fact that it exhibits a non-Abelian phase characterized by Majorana modes localized near vortex excitations [80].

By design, the Kitaev ladder shares two crucial features with its parent: 1) it maps to a simple superconducting system of fermions which can support Majorana fermions in certain parameter regimes and 2) it exhibits a rich variety of sectors based on a $\mathbb{Z}_2$ 'vortex' degree of freedom which inhabits each plaquette. This model is used to study the conditions for the existence of Majorana modes in the various sectors as well as the effects of tuning from a phase without a Majorana mode to a phase with one. Like many spin systems, the Kitaev ladder exhibits both ferromagnetic and paramagnetic phases, depending on the strength of this magnetic field. As discussed in the previous chapter, there is a direct correspondence between ferromagnetism (in spin system) and Majorana modes (in fermionic system). Using this correspondence as a guide, we find that the various sectors (defined above) exhibit a rich variety of physics. Each sector displays unique conditions for the presence of Majorana modes – some require a critical amount of kinetic energy while others require a critical amount of superconductivity.

Motivated by applications to topological quantum computational schemes [3], there has been a surge of interest in seeking out systems and geometries that can realize and manipulate isolated Majorana modes [75, 86, 46]. Some analogous studies in the Kitaev honeycomb system have identified Majorana modes bound to vortices and schemes for their manipulation [87]. In the ladder system, the isolated modes, as opposed to being present at vortices, completely parallel the 1D p-wave superconducting system in being present at the interface between topologically trivial and non-trivial segments. Moreover, we find that the periodic patterns mentioned above provide a new route for finding phases and configurations that support these modes. In principle, for translationally invariant systems, such phases can be characterized by a $\mathbb{Z}_2$ topological invariant (TI) based on a Chern number. In practice, we find that for complex periodic patterns, such a treatment proves to be rather involved, and can be replaced by the evaluation of a much more direct topological invariant derived from the equations of motion. Our method generalizes the identification of zero energy plane waves by Wen and Zee [88] to the case of evanescent modes. We use this scheme to pinpoint several different configurations of periodic patterns that yield localized Majorana modes in the bulk or at the ends of the Kitaev ladder, somewhat reminiscent of those found in the presence of electrostatic defects [89]. Our analysis provides an alternate route for isolating Majorana modes in 1D p-wave superconductors by applying appropriate periodic potentials.

The organization of this chapter is as follows. In 7.2 we introduce the Kitaev ladder model. A method of identifying topological phases in the corresponding fermionic system is given in 7.3. Section 7.4 presents of several simple vortex sectors and the conditions under which they display non-trivial topology. Finally, conclusions are presented in 7.5.

7.2 The 'Kitaev Ladder'

The Kitaev ladder consists of a single (modified) strip of Kitaev's original two-dimensional honeycomb system except that each plaquette is a square instead of a hexagon. As shown

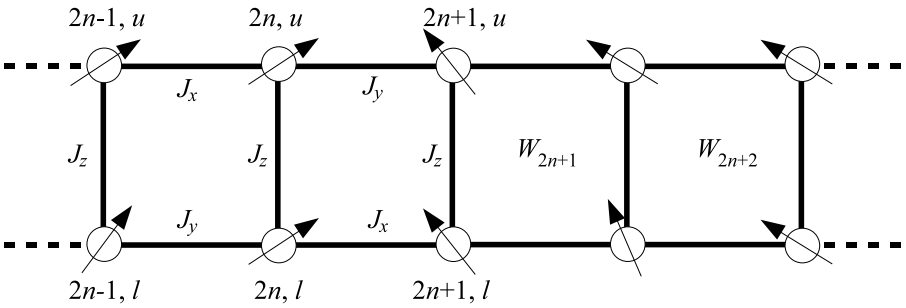

Figure 7.1: The Kitaev ladder, the associated couplings J_x, J_y and J_z, and the vortex operators, W_n.

in Fig. 7.1, spin-1/2 degrees of freedom reside at sites (n,u) and (n,l), where u, l denote the upper and lower legs, respectively. The Hamiltonian is given by

$$\begin{aligned} H &= \sum_{n=1}^{(N-1)/2} \left[J_x \left(\sigma^x_{2n-1,u}\sigma^x_{2n,u} + \sigma^x_{2n,l}\sigma^x_{2n+1,l} \right) + J_y \left(\sigma^y_{2n,u}\sigma^y_{2n+1,u} + \sigma^y_{2n-1,l}\sigma^y_{2n,l} \right) \right] \\ &+ \sum_{n=1}^{N} J_z \sigma^z_{n,u}\sigma^z_{n,l}, \end{aligned} \tag{7.1}$$

where $\sigma^i_{n,u/l}$ denote the Pauli matrices respecting the usual commutation rules, $\left[\sigma^i_{n,s}\sigma^j_{m,s'}\right] = 2i\delta_{m,n}\delta_{s,s'}\epsilon_{ijk}\sigma^k_{n,s}$.

Associated with each plaquette is a vortex operator W_n which commutes with the Hamiltonian and is of the form $\sigma^x_{n,u}\sigma^x_{n+1,u}\sigma^y_{n+1,l}\sigma^y_{n+1,l}$ for n even and $\sigma^y_{n,u}\sigma^y_{n+1,u}\sigma^x_{n,l}\sigma^x_{n+1,l}$ for n odd. Since $W_n^2 = 1$, the eigenvalues of W_n are ± 1; hence these invariants provide a set of $\mathbb{Z}_2$ quantum numbers characterizing different sectors of the Hamiltonian.

As we will see, the fact that the rungs of the Kitaev ladder have ZZ spin couplings (rather than XX, YY, etc.) ensures that the corresponding fermionic Hamiltonian is *local* [74, 83]. The Jordan-Wigner mapping relates spin operators to Majorana fermionic operators:

$$\begin{aligned} a_n &= S_{n,l/u}\sigma^{x/y}_{n,l/u},\ b_n = \pm S_{n,u/l}\sigma^{x/y}_{n,u/l},\ \text{for } n \text{ odd/even}, \\ c_n &= S_{n,l/u}\sigma^{y/x}_{n,l/u},\ d_n = \pm S_{n,u/l}\sigma^{y/x}_{n,u/l},\ \text{for } n \text{ odd/even}. \end{aligned} \tag{7.2}$$

Here, assuming that each leg contains N sites with open (rather than periodic) boundary conditions, the string operator $S_{n,u} = \prod_{m=1}^{n-1} \sigma^z_{m,u}$ runs from the left to the right along the top leg in Fig. 7.1 to the $(n-1)$-th site, while $S_{n,l} = \prod_{m=1}^{N} \sigma^z_{m,u} \prod_{m=n+1}^{N} \sigma^z_{m,l}$ runs completely along the top leg left to right and then back along the bottom leg to the $(n+1)$-th site.

In terms of these Majorana operators, the Hamiltonian is of the form

$$H = \sum_n \left(-iJ_x a_n b_{n+1} + iJ_y b_n a_{n+1} - J_z a_n b_n c_n d_n\right). \tag{7.3}$$

The vortex degree of freedom is encoded in the J_z term. This can be seen by noting that $W_n = -(ic_n d_n)(ic_{n+1}d_{n+1})$ and defining $s_n = ic_n d_n = \prod_{m=n}^{N} W_m c_N d_N$. The Hamiltonian (Fig. 7.1) thus takes the form

$$H = i\sum_n \left(-J_x a_n b_{n+1} + J_y b_n a_{n+1} + J_z s_n a_n b_n\right), \tag{7.4}$$

where $s_n = \pm 1$ depending on the configuration of vortices, namely $W_n = -s_n s_{n+1}$. Now, to make a connection with the p-wave system, one can once more define Dirac fermions $f_n = (a_n + ib_n)/2$ as in the XY spin chain. The vorticity can be captured by another set of Dirac fermions, $g_n = (c_n + id_n)/2$; s_n, which we coin 'site-polarity', reflects the occupancy of these fermions via $s_n = 2g_n^\dagger g_n - 1$ and determines the sign of the chemical potential for the f-fermions

In terms of the Dirac fermions, the Kitaev ladder also maps onto the 1D p-wave superconductor,

$$H = -\sum_n [w\left(f_n^\dagger f_{n+1} + f_{n+1}^\dagger f_n\right) + \Delta\left(f_n f_{n+1} + f_{n+1}^\dagger f_n^\dagger\right) - \mu_n\left(f_n^\dagger f_n - 1/2\right)], \tag{7.5}$$

where

$$w \leftrightarrow J_x + J_y, \quad \Delta \leftrightarrow J_y - J_x, \quad \text{and} \quad \mu_n \leftrightarrow 2s_n J_z. \tag{7.6}$$

Thus, the f-fermions, as in the XY spin chain, participate in the dynamics, while the g-fermions encode the vortex configurations. Each set of fermions spans a Hilbert space of size 2^N, together comprising the Hilbert space of size 2^{2N} thus accounting for all the degrees of freedom of the original $2N$ spins of the ladder system.

Compared to the XY spin chain of the previous section, one main difference in the mapping to the p-wave superconductor is that the sign of the chemical potential is position dependent. Here, we restrict our studies to periodic patterns. For s_n with period p, we can employ the decomposition

$$s_n \;=\; \sum_{q=0}^{p-1} \left(s_q e^{i2\pi qn/p} \;+\; s_q^* e^{-i2\pi qn/p} \right). \tag{7.7}$$

In the momentum basis ($f_k = \frac{1}{\sqrt{N}} \sum_n f_n e^{-ikn}$), the Dirac Hamiltonian describing the Kitaev ladder then takes the form (up to an overall constant)

$$\begin{aligned} H \;=\; & \sum_{0\le k<\pi} \left[-2w \cos k \left(f_k^\dagger f_k + f_{-k}^\dagger f_{-k} \right) + \Delta \left(e^{ik} f_k^\dagger f_{-k}^\dagger + e^{-ik} f_{-k} f_k \right) \right] \\ & -2J_z \sum_{0\le k<2\pi} \sum_{q=0}^{p-1} \left(s_q f_{k+2\pi q/p}^\dagger f_k + s_q^* f_{k-2\pi q/p}^\dagger f_k \right). \end{aligned} \tag{7.8}$$

7.3 Identifying isolated Majorana modes

The fermionic Hamiltonian in Eq. 7.5 provides a starting point for exploring various conditions under which bulk or boundary Majorana modes may appear. In this section, we develop a formalism which enables us to identify these modes in a range of vortex sectors. We employ the transfer matrix method which has been used extensively in 1D systems [90, 91] and is well suited to study bound states. The presence of bound Majorana states is governed by the growth or decay of the eigenfunctions of the transfer matrix. As a way of discerning the existence of these states, we employ an invariant which is constructed by analytically continuing plane wave states.

7.3.1 Transfer matrix approach

The transfer matrix can be constructed by employing the Heisenberg representation and deriving the equations of motion from the Hamiltonian of Eq. 7.4 for the time dependent Majorana modes $a_n = \alpha_n e^{-i\omega t}$ and $b_n = \beta_n e^{-i\omega t}$. These equations are of the form

$$\begin{aligned} (w-\Delta)\,\alpha_{n-1} + (w+\Delta)\,\alpha_{n+1} - \mu_n \alpha_n &= -i\omega\beta_n, \\ -(w+\Delta)\,\beta_{n-1} - (w-\Delta)\,\beta_{n+1} + \mu_n \beta_n &= -i\omega\alpha_n, \end{aligned} \tag{7.9}$$

where we have invoked Eq. 7.6.

To identify Majorana modes, we focus on $\omega = 0$ which allows a decoupling between the a and b Majorana modes. Equations for α_n and β_n can be written in the transfer matrix form

$$\begin{pmatrix} \alpha_{n+1} \\ \alpha_n \end{pmatrix} = A_n \begin{pmatrix} \alpha_n \\ \alpha_{n-1} \end{pmatrix}, \quad \text{where} \quad A_n = \begin{pmatrix} \frac{\mu_n}{\Delta+w} & \frac{\Delta-w}{\Delta+w} \\ 1 & 0 \end{pmatrix}. \tag{7.10}$$

Similar expressions hold for the β_n's since the respective transfer matrices are related by $B_n = A_n^{-1}$. Knowing the behavior of the a-modes thus completely determines that of the b-modes.

This transfer matrix formulation enables us to study the growth versus decay of modes at the boundary of a finite piece of the ladder or at the interface between two parts of the ladder in different phases. In particular, for a homogeneous system having all couplings and s_n constant, this behavior is determined by the eigenvalues of any A_n, while for a region having periodicity p in the s_n's, it is determined by the eigenvalues of the matrix

$$\mathcal{A}_P = A_p\, A_{p-1}\, \cdots\, A_2\, A_1. \tag{7.11}$$

Majorana modes bound to the ends of a finite chain require that both eigenvalues of $\mathcal{A}_P$ be either smaller or greater than unity in magnitude. We will denote the number of eigenvalues

of $\mathcal{A}_P$ with magnitude less than 1 by n_f. The case of $n_f = 2$ corresponds to an a-mode localized at the left end and a b-mode at the right end. The conditions on the eigenvalues ensure that the localized modes can simultaneously respect constraints at the boundary and normalizability. For instance, in the case of open boundary conditions (with a chain which goes from $n = 1$ to ∞), the boundary conditions derive from the equation of motion for a_1: $(w + \Delta)\alpha_2 = \mu_1\alpha_1$. The corresponding vector

$$\begin{pmatrix} \alpha_2 \\ \alpha_1 \end{pmatrix} = c \begin{pmatrix} \mu_1 \\ w + \Delta \end{pmatrix} \tag{7.12}$$

can be written as a linear superposition of the two eigenvectors of $\mathcal{A}_P$. We then see from Eq. 7.10 that $\alpha_n \to 0$ as $n \to \infty$ if both the eigenvalues of $\mathcal{A}_P$ are smaller than unity. These cases are illustrated in Fig. 7.2.

It is instructive to verify that these conditions do in fact reproduce the results of the previous chapter (6.2, in particular). For $\mu_n = \mu$, it is appropriate to consider a single matrix A_n which has eigenvalues

$$\lambda_\pm = -\frac{\mu}{2(\Delta + w)} \pm \frac{1}{2}\sqrt{\left(\frac{\mu}{\Delta + w}\right)^2 + 4\left(\frac{\Delta - w}{\Delta + w}\right)}. \tag{7.13}$$

A straightforward analysis of $\lambda_\pm$ reveals that the that $|\lambda_\pm| < 1$ or $|\lambda_\pm| > 1$ if and only if $2|w| > |\mu|$. This is in agreement with 6.2. Specifically,

1. if $2|w| > |\mu|$ and $w\Delta > 0$, then $|\lambda_\pm| < 1$,

2. if $2|w| > |\mu|$ and $w\Delta < 0$, then $|\lambda_\pm| > 1$,

3. and if $2|w| < |\mu|$, then $|\lambda_1| > 1$ and $|\lambda_2| < 1$.

Bound Majorana states in the bulk of the chain can be realized by juxtaposing two regions corresponding to different phases. The highlighting feature of this system is its ability to dial

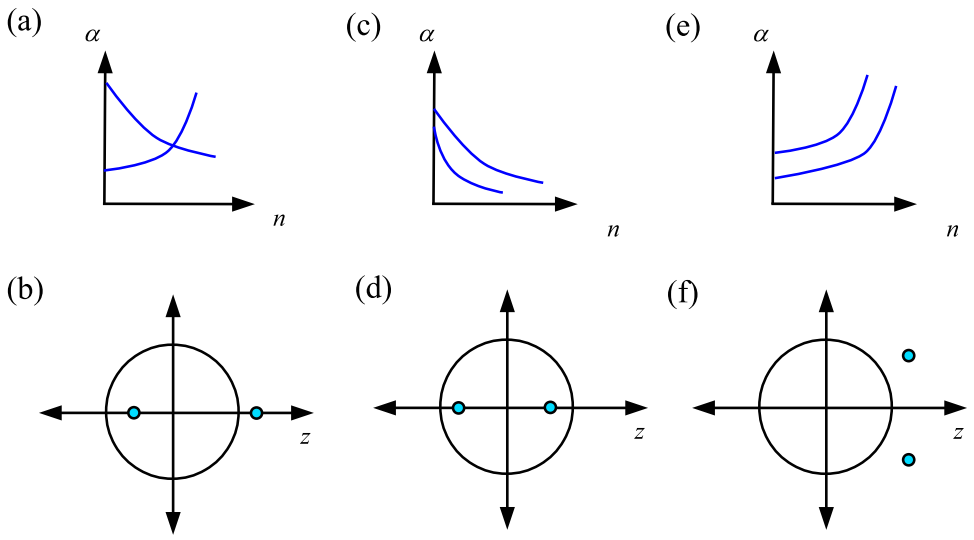

Figure 7.2: (a,c,e) Plots of α (two curves correspond to the eigenvectors of the transfer matrix) as a function of n for the cases $n_f = 1, 2, 0$, respectively. (b,d,f) Zeros of f and the unit circle plotted in the complex plane for the cases $n_f = 1, 2, 0$, respectively. The case in which exactly one eigenvalue lies inside the unit disk (a,b) corresponds to the topologically trivial phase whereas (c-f) indicate non-trivial topology. In (c,d) both eigenvalues are less than one in magnitude, indicating that the wave function of the a Majorana mode decays to the right. This case thus reflects an a Majorana mode localized on the left hand side of the system and a b Majorana mode localized on the right. In (e,f), both eigenvalues are greater than 1 in magnitude and thus the a and b modes are exchanged.

in to different phases by changing the vortex patterns. We thus consider the interface of two semi-infinite patterns P ($n < 0$) and Q ($n \geq 0$) having periodicities p and q, respectively, but with the same values of the couplings w, Δ, and μ. Considerations similar to those above enable us to identify two situations in which there exists exactly one normalizable Majorana mode for n tending to both ∞ and $-\infty$. These correspond to (i) $\mathcal{A}_P$ having both eigenvalues larger than 1 in magnitude or both smaller than 1 and $\mathcal{A}_Q$ having exactly one eigenvalue less than 1 in magnitude, or (ii) $\mathcal{A}_P$ having exactly one eigenvalue larger than 1 in magnitude and $\mathcal{A}_Q$ having both eigenvalues less than 1 or both greater than 1 in magnitude. Other situations yield either no bound mode or a pair of concurrent Majorana modes.

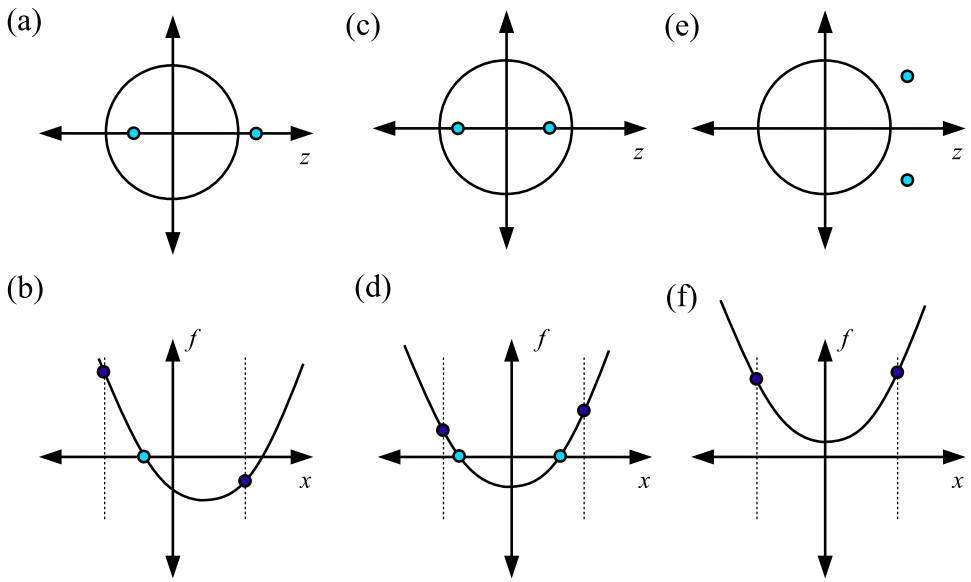

Figure 7.3: (a,c,e) Zeros of f and the unit circle plotted in the complex plane for the cases $n_f = 1, 2, 0$, respectively. (b,d,f) Corresponding plots of $f(x, y = 0)$ where $z = x + iy$ for the cases $n_f = 1, 2, 0$, respectively. The vertical lines are at $x = \pm 1$, and the dark blue points indicate the values of $f(\pm 1)$, whereas the light blue points indicate zeros of f which lie in the range $-1 < x < 1$. The case in which exactly one eigenvalue lies inside the unit disk (a,b) corresponds to the topologically trivial phase. Note that in (b) we have $\nu = 1$ (see Eq. 7.14). (c-f) correspond to topologically nontrivial phases. In (d) and (f) $\nu = -1$. Also, see Fig. 7.2.

7.3.2 Topological invariant

The relevant features of the transfer matrix structure can be gleaned by a simple consideration of its analytic properties. This analysis extends the application of the TI introduced by Wen and Zee [88] to the study of evanescent modes. Our construction of the existential invariant is derived from $f(z)$, the characteristic polynomial of $\mathcal{A}_P$. Given that $\mathcal{A}_P$ is a real 2×2 matrix, a single root inside the unit disk must lie on the real axis. Thus the index

$$\nu = -\operatorname{sgn}\left(f(1)f(-1)\right), \quad \text{where} \quad f(z) = \det(\mathcal{A}_P - Iz), \tag{7.14}$$

is equal to 1 if and only if $\mathcal{A}_P$ has exactly one eigenvalue with a magnitude less than 1 (see Fig. 7.3). This case of $\nu = 1$ indicates a topologically trivial state, i.e., one with no end

Majorana modes. However, $\nu = -1$ indicates the existence of end Majorana modes reflected by $\mathcal{A}_P$ having both eigenvalues less than or both greater than 1 in magnitude. The marginal case $\nu = 0$ would imply the closure of the bulk gap. In fact, ν can only change sign if a bulk gap closes. The invariant ν is topological in the sense that it was derived by invoking the continuity of $f(z)$ in the interior of the unit circle. This invariant provides a physically transparent example of the so-called bulk-boundary correspondence. The bulk properties of the system are given by $f(z)$ on the unit circle since these correspond to plane wave states, whereas boundary properties correspond to $|z| \neq 1$.

The TI ν can be related to that of Wen and Zee [88] by noting $n = (-1)^{n_f+1}$. They employ the principle of the argument in the form

$$n_f = \frac{1}{2\pi i} \oint_{|z|=1} dz \, \frac{f'(z)}{f(z)} \tag{7.15}$$

to identify plane wave zero modes. Furthermore, $f(z)$ was replaced by the dispersion which can also be done in our case but makes the analysis more involved.

Given that ν can only change if a bulk gap closes, it seems that the quantity n_f is topologically protected. This result is at odds with the general classification scheme of topological insulators: a 1D time-reversal invariant superconductor has topologically protection only at the level of $\mathbb{Z}_2$ [92] (rather than $\mathbb{Z}$). However, here the fermionic Hamiltonian arises from a spin system and thus the parameters w and Δ must be real. Consider relaxing this condition and taking $\Delta \to \Delta e^{i\varphi}$. As φ goes from 0 to π, the a and b Majoranas are exchanged; therefore n_f goes from 0 to 2 or vice versa, while $n_f = 1$ remains unchanged. Thus, only the parity of n_f is protected in this case. On the other hand, if Δ were real, changing the sign of Δ would require closing the gap. All that said, we will focus on the parity of n_f given that this controls the salient features of the system and the physics of interest.

7.3.3 Generalization of topological invariant

The methods presented here and the form of ν are easily generalized to any (non-interacting) fermionic system. For concreteness, we consider a Hamiltonian of the form

$$H = \sum_{n\geq 1}\sum_{m=1}^{r}\left(w_m f_{n+m}^\dagger f_n - \Delta_m f_{n+m}^\dagger f_n^\dagger + \text{H.c.}\right) + \sum_{n\geq 1}\mu_n f_n^\dagger f_n \tag{7.16}$$

The equations of motion for this system can be described by a $d \times d$ transfer matrix, where $d = 2r$. Below, it is demonstrated that the appropriate generalization of Eq. 7.14 is given by

$$\nu = (-1)^r \text{sgn}\left(f(1)f(-1)\right). \tag{7.17}$$

We emphasize that we are considering open boundary conditions. We focus on the a_n Majorana modes; each site n gives rise to an equation linking α_n to α's at neighboring sites. Information can be propagated along the chain by a transfer matrix with 'initial conditions' which take the form of a vector of dimension d. The components of this vector are not independent: they are constrained by equations of motion *not* taken into account by the transfer matrix. The first equation which connects $2r + 1$ sites (and thus, the first site for which the transfer matrix can be employed) is the $(r + 1)^{th}$. Hence, there are $r = d/2$ constraints among the initial conditions or, equivalently, $d - d/2 = d/2$ unconstrained degrees of freedom. The boundary conditions are homogeneous and thus normalization does not introduce an additional constraint. Without loss of generality (as we argue below), take $n_f \geq r$. Because the system is gapped, there must be $d - n_f$ eigenvalues with magnitude greater than 1. Now, the $d/2$ free conditions may be used to ensure that the initial eigenvector is orthogonal to those eigenvectors with eigenvalues of magnitude greater than 1. This leaves $d/2 - (d - n_f) = n_f - d/2 = n_f - r$. Each of these eigenvalues will lead to a normalizable Marajona mode. Hence, the parity of the number of Majorana modes at the end of the chain is given by $\nu = (-1)^{n_f - r}$. Given that $(-1)^{n_f} = \text{sgn}\left(f(1)f(-1)\right)$, Eq. 7.17 immediately

follows. If, contrary to the assumption above, $n_f < r$, then it is impossible to localize an a Majorana near $n = 1$. Instead, we must consider b Majorana modes and the same conclusion is obtained (i.e. Eq. 7.17). Although this result seems to depend on the specific boundary conditions we've assumed, its generality is easily seen: if we imagine adiabatically changing the boundary conditions but not changing the bulk Hamiltonian, then the parity of the Majorana modes at the end must be conserved.

There is an intimate connection between the topology of a system and its normal state dispersion $\omega(k)$ [73]. This relationship will be of considerable importance in the following chapter. Let ξ denote the number of zeros of $\omega(k)$ with $0 < k < \pi$. Now, take $z = e^{ik}$. Since the zeros of f are also the zeros of $\omega(k)$, this implies that there are ξ zeros of f on the upper half of the unit circle (i.e., for $|z| = 1$ and Im $z > 0$). Continuity then implies that $\text{sgn}\,(f(1)f(-1)) = (-1)^{\xi}$. Now, in the normal state (since it satisfies time-reversal symmetry), if z_i is a root of f, then so is $1/z_i$. Thus, if there are n_f roots inside the unit circle, then there are n_f roots outside the unit circle. The total number of roots is thus

$$2n_f + 2\xi = d. \tag{7.18}$$

If we turn on very weak superconductivity (i.e. $\Delta_m \ll \omega(k = 0), \omega(\pi)$), then the sign of $f(1)f(-1)$ can not change. Thus, since we have in general that $\nu = (-1)^{d/2+n_f}$, using Eq. 7.18 gives

$$\nu = (-1)^{\xi}. \tag{7.19}$$

In the next chapter, we will quantify how large the superconductivity has to be for this relation to fail.

7.3.4 Relation to Other Topological Invariants

There are two topological invariants commonly employed in the study of topological insulators and superconductors: the Pfaffian and the Chern number. We now argue that these invariants are equivalent to ν.

In [73], Kitaev used a TI based on the Pfaffian of a matrix related to the Hamiltonian. We will not introduce this quantity, however we do demonstrate that our ν and Kitaev's TI always agree. We begin by noting that in the limit of weak superconductivity, our general result for ν (Eq. 7.17) and Kitaev's TI coincide (see Eq. 28 of [73]). However, this correspondence must always hold since as the Hamiltonian is continuously deformed, the Pfaffian and ν pass through zero precisely when the bulk gap closes.

The topological invariant based on Chern number technology for a 1D particle-hole symmetric superconductor is intimately related to the sum of the Berry's phases of the filled bands as k is taken from 0 to 2π [92]. The relationship between this quantity and zero modes enclosed by a general path follows from [93]. There, it is shown that this Berry's phase is related to the parity of the number of degenerate points in the interior of the path. Now, since the model we consider has particle-hole symmetry, any degeneracy between bands at non-zero energy must occur twice, once at E and once at $-E$. Thus, only degeneracies at $E = 0$ contribute to the overall parity.

The relationship between zero modes and topological invariants is described by an *index theorem* [92]. In cases in which the Hamiltonian has a symmetry (for example time-reversal or particle-hole), the presence of an edge state may be gleaned from the existence of boundary zero modes. This state of affairs does not hold for cases in which there is no symmetry, as in the case of the quantum Hall effect. Although the invariant derived in [1] based on the Berry's phase is also sensitive to zero modes (because of the relation described above), in that case these are plane wave states and (ostensibly) have nothing to do with any edge modes present.

7.4 Topology of various vortex sectors

We employ the transfer matrix approach and the invariant ν to show that a diverse set of patterns in the site-polarities s_n can give rise to end Majorana modes. The conditions for non-trivial topology are diverse and the general properties of these conditions is the subject of the next chapter.

7.4.1 Full vortex sector: $s_n = 1$

The full vortex sector is equivalent to the uniform case (or the XY spin chain) studied in Section 6.2 and thus this is a good test of the formalism. Specifically, we claimed that the condition for a phase to be topological is given by $\nu = -1$, where ν is the topological invariant of Eq. 7.14. The corresponding site-independent transfer matrix is

$$\mathcal{A} = \begin{pmatrix} \frac{\mu}{\Delta+w} & \frac{\Delta-w}{\Delta+w} \\ 1 & 0 \end{pmatrix}, \tag{7.20}$$

which yields

$$f(z) \;=\; \det(\mathcal{A} - Iz) \;=\; z^2 - \left(\frac{\mu}{\Delta+w}\right) z \;-\; \left(\frac{\Delta-w}{\Delta+w}\right). \tag{7.21}$$

Hence,

$$\nu \;=\; -\;\operatorname{sgn}\left(f(1)f(-1)\right) \;=\; \operatorname{sgn}\left(|\mu| - 2\,|w|\right), \tag{7.22}$$

for $\Delta + w \neq 0$. A consideration of the location of the zeros of $f(z)$ shows that an a (b) Majorana mode is localized to the right (left) side of the system if $2w > |\mu|$ and $\Delta > 0$. If $2w < -|\mu|$ the positions of the a and b Majoranas are switched. Switching the sign of Δ also interchanges the Majorana modes (see Fig. 7.4).

Consider the bound modes obtained by juxtaposing two regions in phases I and III on the left and right, respectively, in the phase diagram of Fig. 6.2. The bound state structure

at the interface can be derived by considering the closing of the gap at the phase boundary. Close to this region, the dispersion in equation (6.2) takes the form $\omega_k = \pm 2\sqrt{\Delta^2(\delta k)^2 + m^2}$ at $k \approx \pi$, where $m(x) = \mu/2 - w$. Here, the continuum version of the equations of motion, Eq. (7.9), is given by $\partial_x a(x) = m(x)a(x)$ and $\partial_x b(x) = -m(x)b(x)$. In this case, the Majorana mode takes the form $b(x) \propto e^{-\int_0^x dx' m(x')}$. In fact, this solution corresponds to that of the celebrated Jackiw and Rebbi model [94] as applied to Majorana fermions.

7.4.2 Vortex-free sector: $s_n = (-1)^n$

In the 2D honeycomb system, the vortex-free sector is special in that it corresponds to the ground state sector for all values of spin couplings. This condition, however, holds only for a range of parameters in the Kitaev ladder. To show this, we consider the limit of J_z large compared to J_x and J_y. In the language of a p-wave superconductor, let us assume that μ is large and positive. We then find that the perturbative change in the ground state energy compared to the $w = \Delta = 0$ limit is given by the second order expression

$$\Delta E_0 \;=\; -\;\frac{1}{2\mu}\;\sum_n\;\left[w^2(1 - s_n s_{n+1})\;+\;\Delta^2(1 + s_n s_{n+1})\right]. \tag{7.23}$$

If $w^2 > \Delta^2$, the ground state energy is lowest if $s_n s_{n+1} = -1$ for all n, i.e., if $s_n = (-1)^n$; this is the sector with no vortices. If $w^2 < \Delta^2$, however, the ground state energy is lowest if $s_n s_{n+1} = 1$ for all n, i.e., if $s_n = \pm 1$ for all n; this is the full vortex sector. Another difference is that unlike in the 2D system, reduced dimensionality renders the Kitaev ladder system to be gapped everywhere except along phase boundaries.

For the vortex free sector, we can identify the range of parameter space which yields topologically non-trivial phases. Towards this end, we identify the period 2 transfer matrix

$$\mathcal{A} = \begin{pmatrix} -\frac{\mu}{\Delta+w} & \frac{\Delta-w}{\Delta+w} \\ 1 & 0 \end{pmatrix} \begin{pmatrix} \frac{\mu}{\Delta+w} & \frac{\Delta-w}{\Delta+w} \\ 1 & 0 \end{pmatrix}, \tag{7.24}$$

and the characteristic polynomial

$$f(z) = \det(\mathcal{A} - Iz) = z^2 + \left(\frac{2w^2 - 2\Delta^2 + \mu^2}{(w+\Delta)^2}\right) z + \left(\frac{\Delta - w}{\Delta + w}\right)^2 . \tag{7.25}$$

The topological invariant ν (for $w + \Delta \neq 0$) takes the form

$$\nu \;=\; -\;\mathrm{sgn}\left(f(1)f(-1)\right) \;=\; \mathrm{sgn}\left(|\mu| - 2\,|\Delta|\right). \tag{7.26}$$

In this case, the topological nature of the phase depends on the relative magnitude of the superconducting order parameter and the chemical potential, as opposed to the hopping integral and the chemical potential as in the uniform case, cf. Eq. (7.22) and Eq. (7.26). It may be verified that the boundary separating topologically trivial and non-trivial regions derived from $f(1)f(-1) = 0$ is equivalent to gap closure. The dispersion for the present case is given by

$$\omega_k^2 \;=\; 2\,\left[w^2 \;+\; \Delta^2 \;+\; \frac{\mu^2}{2} \;+\; \left(w^2 \;-\; \Delta^2\right)\cos(2k) \;\pm\; \Delta\mu \sin k\right]. \tag{7.27}$$

This is consistent with Eq. (7.26): the gap closes at $k = \pm\pi/2$ for $2|\Delta| = |\mu|$.

Notably, a periodic pattern can give rise to qualitatively different physics. In contrast to the uniform case, the topology of the alternating sector depends on the magnitude of Δ.

7.4.3 Higher period sectors

For a general periodic structure P characterized by the transfer matrix $\mathcal{A}_P$ of Eq. (7.11), we have

$$\begin{aligned} \nu_P \;&=\; -\prod_{m=\pm} \mathrm{sgn}\left(\det \mathcal{A}_P + 1 + m\mathrm{Tr}\mathcal{A}_P\right) \\ &=\; \mathrm{sgn}\left(|\mathrm{Tr}\mathcal{A}_P| - |\det \mathcal{A}_P + 1|\right). \end{aligned} \tag{7.28}$$

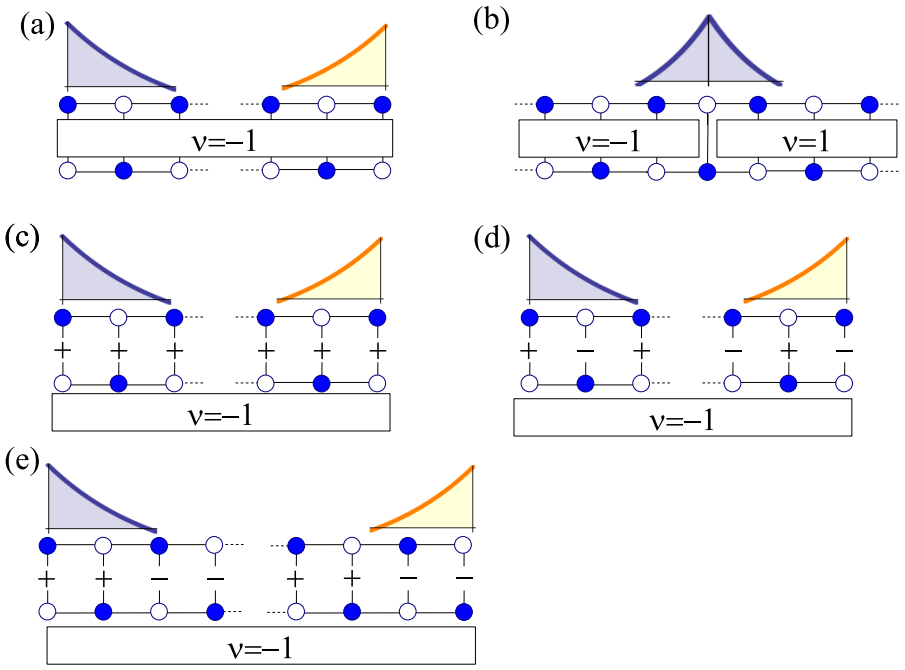

Figure 7.4: Examples of isolated Majorana modes for the Kitaev ladder system. Generically, Majorana modes are hosted at (a) the ends of ladders with nontrivial topology ($\nu = -1$) or at (b) the interface between regions with $\nu = -1$ and $\nu = 1$. In the case of the uniform sector (P_1) $s_n = 1$ with $2|w| > |\mu|$, individual Majorana modes are hosted at (c) each end of a ladder. Other examples of end Majorana modes include (d) the alternating sector (P_2) $s_n = (-1)^n$ with $2|\Delta| > |\mu|$ and (e) the sector $Q_4 = ++--$ with $2\sqrt{|w\Delta|} > |\mu|$.

It follows from these expressions that any two chains which are cyclic permutations of each other must have the same topology, as we would expect physically. It is also straightforward to show that the transformation $s_n \to -s_n$ for all n will not change the topology of the chain. Although giving a full analytic expression is not practical, it may be noted that the detailed features of a pattern of the site polarities s_n that control its topology enter Eq. 7.28 through the quantity Tr $\mathcal{A}_P$.

We now consider an expansion of Tr $\mathcal{A}_P$ in certain limits. For example, if $|\mu| < 2|w \pm \Delta|$, Tr $\mathcal{A}_P$ can be expanded in powers of $\mu^2/(w^2 - \Delta^2)$: for p even this yields

$$\text{Tr } \mathcal{A}_P = \left(\frac{\Delta - w}{\Delta + w}\right)^{p/2} \left[2 + \frac{\mu^2}{2(w^2 - \Delta^2)} \left(\sum_{m=1}^{p/2} s_{2m}\right) \left(\sum_{n=1}^{p/2} s_{2n-1}\right) + \mathcal{O}\left(\mu^4\right)\right]. \qquad (7.29)$$

Table 7.1: Criteria for non-trivial topology for sectors up to period 4

period	examples	non-trivial topology for
1	$P_1 = +\ldots$	$2\lvert w\rvert > \lvert\mu\rvert$
2	$P_2 = +-\ldots$	$2\lvert\Delta\rvert > \lvert\mu\rvert$
4	$P_4 = +---\ldots$	$2\left(w^2+\Delta^2\right) > \mu^2$
4	$Q_4 = ++--\ldots$	$4\lvert w\Delta\rvert > \mu^2$

Thus, in this case the quantity $\left(\sum_{m=1}^{p/2} s_{2m}\right)\left(\sum_{n=1}^{p/2} s_{2n-1}\right)$ is pivotal in determining the topology of P. As a specific example, taking $\mathcal{A}_P = A_1A_2A_3A_4$ for a generic period 4 pattern (s_1, s_2, s_3, s_4), we get an expression for ν which is a function of $(s_1+s_3)(s_2+s_4)$, $s_1s_2s_3s_4$, and the couplings constants w, Δ, and μ. Thus from the standpoint of topologically non-trivial phases, there are two distinct period 4 patterns, namely $+++-$ and $++--$. For instance, the application of Eq. 7.28 to the pattern $Q_4 = ++--$ yields

$$\nu_{Q_4} \;=\; \mathrm{sgn}\left(\mu^2 - 4|w\Delta|\right), \tag{7.30}$$

as illustrated in Fig. 7.4e. Similar constraints are also obtained for the other patterns, demonstrating that patterns of higher periodicity can have phase boundaries involving more intricate dependencies on the values of μ, w, and Δ. Thus, we have shown that the topology and existence of isolated Majorana modes can be controlled by configurations of vortices in the Kitaev spin ladder. Table 7.1 summarizes the conditions for non-trivial topology for a few sectors.

7.5 Conclusions

In this chapter we presented the Kitaev ladder, a model of interacting spin whose fermionic counterpart admits topological phases characterized by Majornana fermions. It was found that the various vortex sectors give rise to a rich set of conditions for non-trivial topol-

ogy which, in terms of fermions, corresponds to the sign of the local chemical potential. We argued that periodic potentials represent an interesting way to manipulate and study Majorana fermions.

Chapter 8

Topological phase diagram of p-wave superconductors with disordered and quasiperiodic potentials

Recent claims of the detection of Majorana states in a semiconducting/superconducting heterostructure are particularly exciting. The experiment described in [5, 4] endeavors to seek signatures of Majorana fermions from the properties of the low-lying Andreev spectrum which has been demonstrated to be sensitive to the topological phase transition associated with their formation. Given that Majorana fermions are required to live exactly at zero energy, a crucial element in theoretically validating these results is an understanding of the role disorder, present in any real system, plays in the topological phase transition.

Previous studies of the effect of disorder on Majorana modes have focused on cases of weak and slowly varying disorder (compared with the inverse superconducting gap) [95, 96] and the special point of the phase diagram corresponding to the quantum Ising chain [97]. The present chapter investigates the topological phase diagram in a more general way. We wed Anderson's model of on-site disorder to Kitaev's model of a 1D p-wave superconductor. Given the work of the previous chapter, it is natural to expect that disorder which varies on the length scale of the lattice will yield interesting physics. Indeed, the topological phase diagrams exhibited by simple periodic potentials (see 7.4) provides a natural introduction to the work presented in this chapter. The properties of the uniform case were found to be, vis-à-vis other periodic sectors, anomalous. In general, the topological phase diagram was found to depend on the magnitude of the superconducting pairing unlike the uniform case, a fact which may have important experimental consequences.

A natural strategy for studying this model is to develop methods which leverage the considerable scholarship on disorder and localization physics in 1D. It was observed in [95]

that the transfer matrix structure for the superconducting problem is strongly reminiscent of that of the normal state. We extend this observation by providing an explicit mapping between the superconducting and normal cases. That such a connection may be made is suggested by the results of 7.3.3. In particular, the topology of the system for (vanishingly) weak superconductivity is intimately related to its band structure: $\nu = (-1)^{\xi}$, where ξ is the number of Fermi points between 0 and π. On the other hand, a consideration of periodic systems reveals that for systems which are gapped at $E = 0$ a finite amount of superconductivity is required to drive the system into the topological phase. Here we quantify these observations and apply them to cases of disordered and quasiperiodic potentials.

Disordered 1D systems exhibit Griffiths-McCoy singularities in which the density of states near zero energy decays as a power law; these systems thus do not possess a sharp gap. However, isolated Majorana modes can still be characterized by their localization length. Our central result links the normal state localization length (at zero energy) and the strength of the superconducting pairing required to engender an end zero energy mode. The physical picture which this mathematical analysis provides is revealing; the topological phase diagrams of disordered systems arise as a result of the competition between the localizing effects of disorder and superconducting pairing which tends to spatially separate the Majorana fermions composing a Dirac state.

The analysis is applied to several situations. We consider the case of weak disorder and find results similar to those found in continuum models based on the Dirac equation [96]. The case of uniform disorder is examined both numerically and analytically and highlights some very general properties of disordered phase diagrams. The case of Lorentzian-distributed disorder has a phase diagram which can be solved completely and thus provides a nice confirmation of the methods presented here. Quasiperiodic patterns (i.e., patterns of incommensurate period with respect to the lattice) provide a natural interpolation between periodic and disordered system. We thus investigate periodic potentials of the form $\mu_n = \alpha + \beta \cos(2\pi p n/q + \phi)$, where p, q are relatively prime whole numbers with q

large. Interestingly, this potential is intimately related to the fractal known as *Hofstadter's butterfly* [98]

The organization of this chapter is as follows. In 8.1 we introduce a general method for studying the topological phase diagram of any inhomogeneous 1D p-wave superconductor and find a connection to its normal state properties. In 8.2, we compare numerical simulations with our theory, finding excellent agreement. Finally, in 8.4 we present our conclusions.

8.1 Analysis of topological phase diagram

The methods developed in 7.3 may be used to study, both analytically and numerically, the topological phase diagram in terms of μ and Δ. Although the transfer matrix method of 7.3 is well-suited to the study of the topological phases of this system, the particular form of ν given in Eq. 7.14 becomes unwieldy for a product of a large number of transfer matrices. We thus reformulate these methods.

8.1.1 Model

We consider Kitaev's model of a p-wave superconductor subject to a non-uniform on-site chemical potential. The Hamiltonian describing this system is given by Eq. 7.5 which we now repeat

$$H = -\sum_{n=1}^{N} \left[w \left(f_n^\dagger f_{n+1} + f_{n+1}^\dagger f_n \right) - \Delta \left(f_n f_{n+1} + f_{n+1}^\dagger f_n^\dagger \right) \right] - \sum_{n=1}^{N} \mu_n \left(f_n^\dagger f_n - 1/2 \right). \quad (8.1)$$

N is the length of the system. In the case of disordered potentials, W will serve as a (linear) measure of the strength of the potential (i.e., if $\mu_n \to 2\mu_n$, then $W \to 2W$).

8.1.2 Topological phase diagram and normal state properties

In the 1D superconducting system of interest here, non-trivial topology is characterized by isolated zero energy Majorana fermions at the ends of an infinitely long system. In this chapter, we consider the topological phase diagram in the parameter space of W (or some other measure of the strength of the potential) and Δ. As found in [95], there is generally a nonzero Δ required to reach the topological phase in the case of an inhomogeneous potential. Typically, this critical value of Δ is larger for stronger potentials.

The (zero energy) equations derived from Eq. 8.1 are given by Eq. 7.10. Since A_n can be considered a function of μ_n/w and Δ/w, we take $w = 1$. As in the previous chapter, we define $\mathcal{A} = \prod_n A_n$, whose eigenvalues we call $\lambda_{1/2}$ with $|\lambda_2| \geq |\lambda_1|$. Since the topology of the system depends only on the magnitude of Δ, we take Δ to be positive. For $\Delta > 0$, $\det\ \mathcal{A} < 1$ since $\det A_n = (1-\Delta)/(1+\Delta)$. Then, $\lambda_1\lambda_2 < 1$, and therefore $|\lambda_1| < 1$. Thus, n_f is completely determined by λ_2. We thus may rewrite Eq. 7.14 as

$$\nu = -(-1)^{n_f} = \mathrm{sgn}\left(\ln|\lambda_2|\right). \tag{8.2}$$

Eq. 7.19 expresses a relationship between the normal state properties of the system and its topology for weak superconductivity. We now extend this relationship to the case of finite Δ. We begin by writing the transfer matrix A_n in the form $A_n = \sqrt{\zeta} S \tilde{A}_n S^{-1}$ where $S = \mathrm{diag}(1/\zeta^{1/4}, \zeta^{1/4})$ and $\zeta = (1+\Delta)/(1-\Delta)$, where

$$\tilde{A}_n \ = \ \begin{pmatrix} \frac{\mu_n}{\sqrt{1-\Delta^2}} & -1 \\ 1 & 0 \end{pmatrix}. \tag{8.3}$$

This transformation may be used to reexpress $\mathcal{A}(W,\Delta)$ as

$$\mathcal{A}(W,\Delta) = \left(\sqrt{\frac{1+\Delta}{1-\Delta}}\right)^N S\mathcal{A}\left(W/\sqrt{1-\Delta^2}, 0\right) S^{-1}, \tag{8.4}$$

valid for $\Delta < 1$. This expression gives the relationship between the transfer matrices at (W, Δ) to those of a normal state system.

We focus on the phase boundary separating topological and trivial regions of the phase diagram. Using Eq. 8.4, on the phase boundary (where $|\lambda_2| = 1$) Eq. 8.2 leads to the expression

$$\gamma\left(\frac{W}{\sqrt{1-\Delta^2}}\right) = \frac{1}{2}\ln\left(\frac{1+\Delta}{1-\Delta}\right), \tag{8.5}$$

where we have defined the Lyapunov exponent of the normal state

$$\gamma_P(W) \equiv \frac{1}{N}\ln|\lambda_2(W,0)|. \tag{8.6}$$

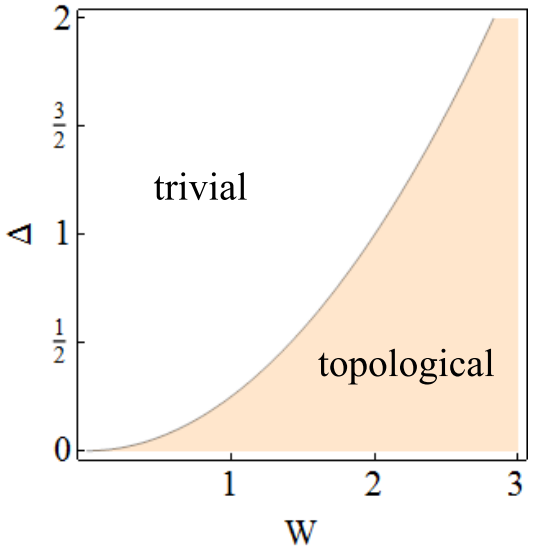

Figure 8.1: Phase diagram for the case of the periodic potential Q_4 whose phase boundary is described by Eq. 8.7.

As an illustration of Eq. 8.5, consider the case of the periodic potential Q_4 defined by $\mu_n = \{W, W, -W, -W, ...\}$. From 7.1, we have that the phase boundary obeys

$$\Delta = \frac{1}{4}W^2. \tag{8.7}$$

The topological phase diagram of Q_4 is shown in Fig. 8.1 Alternatively, we may derive this result from Eq. 8.5. First, the normal state Lyapunov exponent $\gamma_{Q_4}(\mu)$ may be calculated from $\mathcal{A}(\mu, 0) = \prod_{n=1}^{4} A_n$ giving

$$\gamma_{Q_4}(W) = \frac{1}{4} \ln \left(1 + \frac{1}{2} W^4 + \frac{1}{2} W^2 \sqrt{4 + W^4} \right). \tag{8.8}$$

Applying Eq. 8.5 which, for $0 \leq \Delta < 1$, reproduces Eq. 8.7.

8.1.3 Duality linking Δ and $1/\Delta$

The $\Delta > 1$ region of the phase diagram may be obtained by invoking the following duality. If we consider configuration with $P = \{\mu_n\}$, then the transformation

$$\begin{aligned} \mu_n &\rightarrow \frac{\mu_n}{\Delta}, \\ \Delta &\rightarrow \frac{1}{\Delta}, \\ P \rightarrow D(P) \quad &: \quad \{\mu_n\} \rightarrow \{(-1)^n \mu_n\}, \end{aligned} \tag{8.9}$$

leaves the product

$$A_{2n+2} A_{2n+1} A_{2n} A_{2n-1} \tag{8.10}$$

unchanged. Thus, if a point $(W_0, \Delta_0 < 1)$ lies on the phase boundary of P, then $(W_0/\Delta_0, 1/\Delta_0)$ lies on the phase boundary of $D(P)$. Conversely, the knowledge of $D(P)$ in the region $\Delta < 1$ may be used to obtain the phase diagram of P for $\Delta > 1$.

This duality strongly constrains the properties of the phase diagram for cases in which P is self-dual; i.e. $D(P) = P$. For instance, the periodic structure $Q_4 = \{W, W, -W, -W, ...\}$ is self-dual. The equation satisfied by the phase boundary $\Delta = W^2/4$ is invariant under the transformation $W \rightarrow W/\Delta$, $\Delta \rightarrow 1/\Delta$; a property obeyed by any phase boundary of a self-dual potential.

8.1.4 Line $\Delta = 1$

Finally, we turn to the singular point $\Delta = 1$. In this case, $\mathcal{A}$ is readily calculated yielding

$$\mathcal{A} = \prod_{n=1}^{N} \begin{pmatrix} \frac{\mu_n}{2} & 0 \\ 1 & 0 \end{pmatrix} = \frac{1}{2^N} \left(\prod_{n=1}^{N} \mu_n \right) \begin{pmatrix} 1 & 0 \\ 2w/\mu_1 & 0 \end{pmatrix}. \tag{8.11}$$

Thus, $\mathcal{A}(W, 1)$ has the eigenvalues $\frac{1}{2^N} \prod_{n=1}^{N} \mu_n$ and 0. Taken with Eq. 8.2, this expression immediately reveals that the phase boundary passes through the point for which

$$\langle \ln |\mu_n| \rangle = \ln 2, \tag{8.12}$$

where

$$\langle x_n \rangle = \frac{1}{N} \sum_{n=1} x_n. \tag{8.13}$$

At this special point[1], the Hamiltonian Eq. 8.1 is equivalent to the disordered quantum Ising model

$$H = \sum_{n} \left(2\sigma_n^x \sigma_{n+1}^x + \mu_n \sigma_n^x \right), \tag{8.14}$$

which has been intensely studied. We note that the transfer matrix approach described here provides a simple (alternative) derivation of the critical point [43].

8.2 Examples of disordered topological phase diagrams

We now investigate the topological phase diagram for a variety of potentials. We perform numerical simulations and find excellent agreement with theory. Our approach relies on

[1] An interesting application of the methods of this section is to the development of a general asymptotic expansion for the Lyapunov exponent for strong disorder. Consistency of Eqs. 8.5 and 8.12 requires that $\gamma(\mu) \sim \ln \mu$ for $\mu \to \infty$. This is a generalization of results given elsewhere (see [99]).

finding the eigenvalues of $\mathcal{A}$ for N large (typically taken to be $N \sim 10^4$). As is characteristic of 1D disordered and quasiperiodic systems, we find that our numerical results are 'self-averaging' [95]. That is, the properties of a given of a ultra-large system converge to the ensemble average. This effect is particularly easy to see in Eq. 8.12. We begin with an overview of some generic features of topological phase diagrams.

8.2.1 General Features of Disordered Phase Diagrams

Weak, uncorrelated disorder – Consider the case of disorder satisfying $\langle \mu_n \mu_{n'} \rangle = V \delta_{n,n'}$, $\langle \mu_n \rangle = 0$. Using Eq. 8.5 and the form of the Lyapunov exponent for the normal state system [99], we find that the condition for topological non-triviality is given by

$$\Delta > \left(\frac{\Gamma(3/4)}{\Gamma(1/4)} \right)^2 V \approx 0.114V. \tag{8.15}$$

This result may be compared to the continuum case of the Dirac equation, which gives a topologically non-trivial phase for

$$\Delta > \frac{1}{8} V = 0.125V, \tag{8.16}$$

(see [96]).

Strong, uncorrelated disorder – Again, consider the case $\langle \mu_n \mu_{n'} \rangle = V \delta_{n,n'}$, $\langle \mu_n \rangle = 0$. We observe that the duality $D(\cdot)$ does not alter the form of the potential. It immediately follows that Eq. 8.15 describes the phase boundary in the strong disorder regime.

Behavior near $\Delta = 1$ – It is clear from Eq. 8.12 that the behavior of the phase boundary as Δ approaches 1 is extremely sensitive to those values of μ_n which are close to zero. For example, as any $\mu_n \to 0$, $\langle \ln |\mu_n| \rangle \to \infty$. For disordered systems, we thus expect that the behavior of the phase boundary near $\Delta = 1$ to be extremely sensitive to distribution of the μ_n near zero. Indeed, in the cases of uniform and Lorentizian disorder, even though $\langle \ln |\mu_n| \rangle$

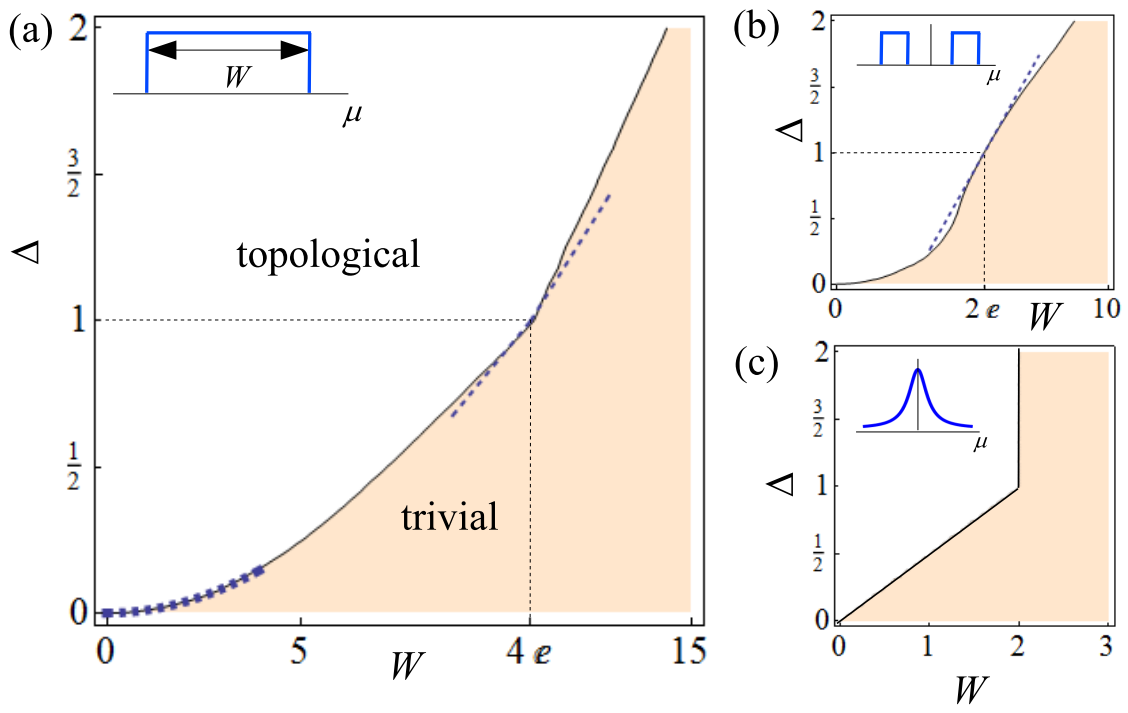

Figure 8.2: Topological phase diagrams for (a) box, (b) double box, and (c) Lorentzian-distributed disorder. Each phase diagram has an inset with a sketch of the corresponding disorder distribution.

remains finite, numerical data suggests that the phase boundary is discontinuous across the line $\Delta = 1$ (see Fig. 8.2). Perturbation theory around $\Delta = 1$ leads to a series which depends on $\langle 1/\mu^n \rangle$ at n^{th} order. Thus, the discontinuity likely stems from the fact that $\langle 1/\mu \rangle$ is badly behaved for these potentials. Indeed, we consider a 'double box' disorder profile (with $\langle 1/\mu \rangle$ finite) which exhibits a continuous slope in the vicinity of $\Delta = 1$, thus bolstering this claim.

8.2.2 Uniform Disorder

The case of box disorder represents the keystone of our survey: it is readily simulated and has been well-studied in both the numerical and theoretical literature. We take the probability

distribution for each μ_n to be

$$f_B(x;W) = \begin{cases} \frac{1}{W} & \text{for } |x| \leq W/2, \\ 0 & \text{otherwise.} \end{cases} \tag{8.17}$$

Fig. 8.2a shows the results of a numerical calculation of the phase diagram. For this distribution, we have

$$V = \langle \mu_n^2 \rangle = \frac{1}{W} \int_{-W/2}^{W/2} \mu^2 d\mu = \frac{W^2}{12}, \tag{8.18}$$

and

$$\langle \ln |\mu_n| \rangle = \ln (W/2) - 1. \tag{8.19}$$

Eq. 8.15 yiels that the system is topological provided

$$\Delta > \frac{1}{12} \left(\frac{\Gamma\left(\frac{3}{4}\right)}{\Gamma\left(\frac{1}{4}\right)} \right)^2 W^2 \approx \frac{1}{105.045} W^2. \tag{8.20}$$

Because the distribution should be approximately self-dual, we have that this is also the behavior of the phase boundary for $W \gg 1$.

Eq. 8.12 gives that the phase diagram intersects the point $(W_c, 1)$ with

$$W_c = 4e \approx 10.873, \tag{8.21}$$

Given that $\langle 1/\mu \rangle$ does not converge, we expect that the phase boundary may be discontinuous across $\Delta = 1$. Indeed, we find numerical evidence for this discontinuity. We may estimate this behavior from the following approximation for the Lyapunov exponent for $W \ll 1$

$$\begin{aligned} \gamma(W) &\sim \ln\left(W/2 + \sqrt{W^2/4 - 4}\right) - \sqrt{W^2/4 - 4} - \ln 2, \\ &\sim \ln (W/2) - 1 + 4/W^2 + \mathcal{O}\left(1/W^4\right), \end{aligned} \tag{8.22}$$

[99] (there is a factor of 2 error in [99]). Invoking this result and the self-duality of f_U, we obtain to linear order around $(W_c, \Delta) = (4e, 1)$

$$\Delta \approx \begin{cases} \frac{e}{2e^2+2} W - \frac{e^2-1}{e^2+1} & \text{for } \Delta < 1, \\ \frac{e}{2e^2-2} W - \frac{e^2+1}{e^2-1} & \text{for } \Delta \geq 1. \end{cases} \tag{8.23}$$

Eq. 8.22 is not exact, and indeed we find that Eq. 8.23 tends to underestimate the strength of the discontinuity found numerically, as shown in Fig. 8.2a. We should note however that the self-duality condition is well obeyed by the numerically determined phase boundary.

8.2.3 Double Box

An example of a phase boundary which we expect to be analytic near $\Delta = 1$ is given by system with disorder drawn from

$$f_{DB}(x; W) = \begin{cases} \frac{2}{W} & \text{for } W/4 \leq |x| \leq W/2, \\ 0 & \text{otherwise.} \end{cases} \tag{8.24}$$

Here, $W_c = 2e \approx 5.437$.

Note that all the $\langle 1/\mu^n \rangle$ exist. We can find calculate the behavior of the phase diagram near $\Delta = 1$ using Eq. 8.12. More directly however, we note that to linear order near $\Delta = 1$, the only expression which is invariant under Eq. 8.9 is

$$\Delta = \alpha W - 1. \tag{8.25}$$

This expression well describes the phase boundary for $\alpha = 1/e$. This phase diagram is shown in Fig. 8.2b.

8.2.4 Lorentzian distributed disorder

The case of Lorentzian disorder, described by

$$f_L(x;W) = \frac{1}{\pi}\frac{W}{x^2+W^2}, \tag{8.26}$$

provides an invaluable test of these methods. The model is exactly soluble, and the normal state Lyapunov exponent is given by

$$\gamma_L(W) = \ln\left(\frac{W}{2} + \sqrt{1+W^2/4}\right). \tag{8.27}$$

This expression was first obtained by Thouless [100] as an application of his celebrated formula connecting the Green's function (and thus localization length) and the density of states for a 1D system. The density of states was obtained by Lloyd via an exact solution of the model [101].

Once again invoking Eq. 8.6 and self-duality yields a phase boundary

$$W = \begin{cases} 2\Delta & \text{for } \Delta < 1, \\ 2 & \text{for } \Delta \geq 1. \end{cases} \tag{8.28}$$

This result is in good agreement with numerical results (see Fig. 8.2c). We note that Eq. 8.15 fails to apply in this case since $V \to \infty$.

8.3 Quasiperiodic Potential

We now consider potentials of the form

$$\mu_n = V + 2\cos 2\pi\omega n. \tag{8.29}$$

We will be interested in cases for which which $\omega = p/q$ with q large. The normal state problem has been well studied in the context of metal-insulator transitions and Anderson localization. This potential also describes an electron hopping on a two-dimensional square lattice in the presence of a perpendicular magnetic field (the parameter ω is related to the flux through each square of the lattice). The spectrum of this operator leads to a fractal object known as *Hofstadter's butterfly* [98]. Superconductivity allows us to consider a new facet to this fascinating system.

Here, we focus on various rational $\omega = p/q$ with q large. We begin by describing the properties of the normal state system. It suffices to take $N = q$. Then, Tr $\mathcal{A}(V)$ is a q^{th} order polynomial in V. The spectrum of the operator (giving rise to plane wave states) corresponds to values of V for which Tr $\mathcal{A}(V) < 2$. It is a particular feature of Eq. 8.29 that every band is present and distinct (see Chapter 13 of [102]). That is, there are q bands separated by $q - 1$ non-zero gaps.

For a sufficiently small Δ, there will exist q distinct regions of non-trivial topology as a function of V; these regions originate from the q bands of the normal state. As Δ is increased, the distinct zones of non-trivial topology will merge. The precise value of Δ for which two bands merge is determined by the the strength of the Lyapunov exponent between the gaps. Since this quantity tends to be larger for larger $|V|$, the gaps closer to $V = 0$ tend to merge before those with $|V|$ large. See Fig. 8.3. Now turning to the full phase $\omega - V$ phase diagram, we see that as superconductivity is increased, Hofstadter's butterfly is 'filled in' by regions of non-trivial topology.

8.4 Discussion and Outlook

In this chapter, the question of the existence of zero energy modes at the end of a disordered semi-infinite p-wave superconductor was considered. These results are expected to be qual-

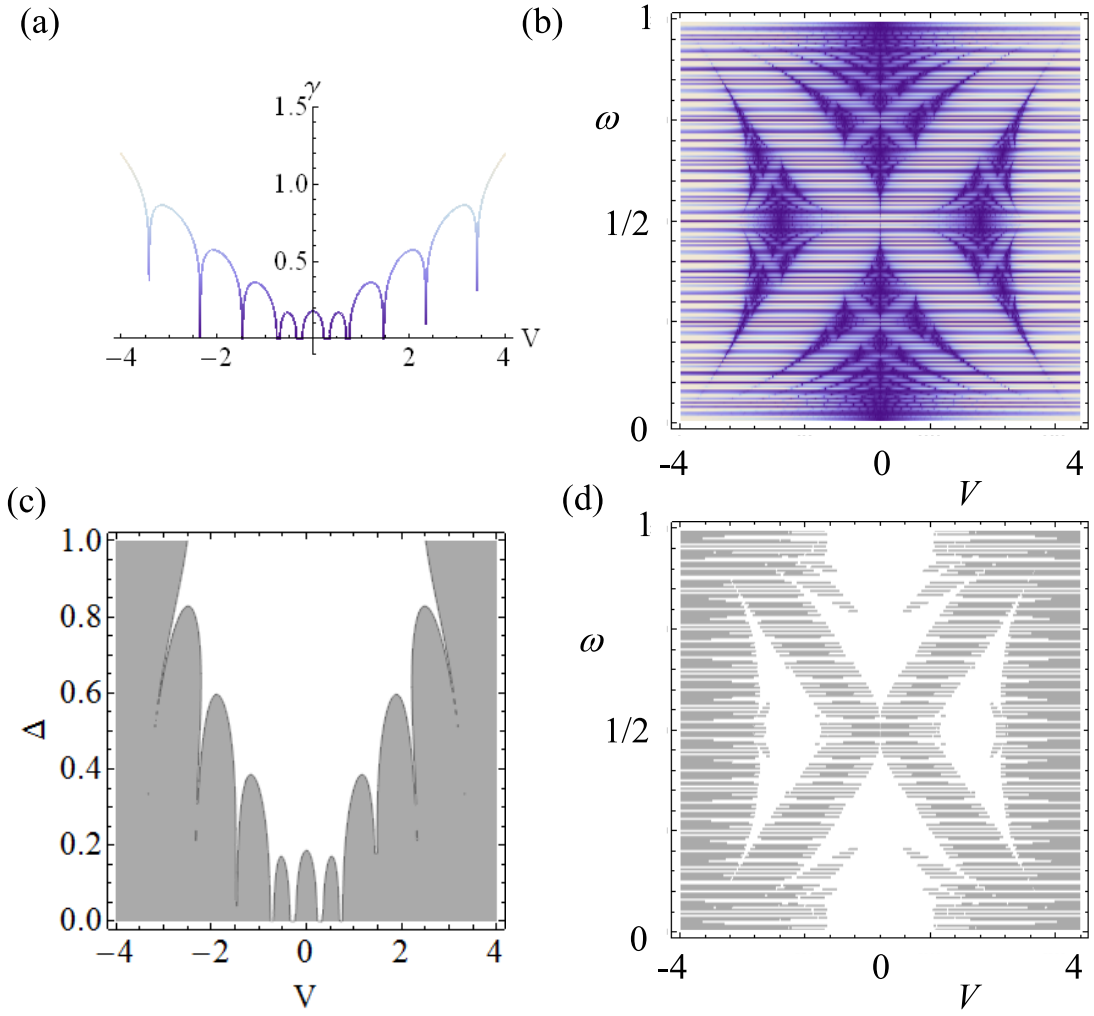

Figure 8.3: (a) The normal state Lyapunov exponent of a system with $\omega = 1/10$ and $W = 2$. Note that there are 10 bands (for which $\eta = 0$), however the figure has insufficient resolution to show all the bands. (b) Topological phase boundary showing the merging of the topological regions as described in the text. For $\Delta \ll 1$, there are are 10 distinct regions of non-trivial topology. At $\Delta = 0.2$, the four central regions have merged to form a single region. (c) A plot (color online) of the Lyapunov exponent of the normal state for $W = 2$ as a function V and ω. The darker (bluer) regions correspond to low values of γ_{AM}, lighter regions correspond to relatively high values. (d) The darkened regions are topologically trivial regions for a value of $\Delta = 0.1$.

itatively similar to those of a finite system of length L, although in this case the Majorana modes in such a system have a coupling which goes as $\sim e^{-L}$. Deep in either phase, we expect that the results obtained here apply to the finite size case.

We found that, in most cases studied, disorder effects may be surmounted: a topologically non-trivial regime will arise for sufficiently strong superconductivity. The case of Lorentzian disorder is an exception. Above a critical disorder strength, the phase is always topologically trivial. A next step in this analysis would be to consider the spectral and spatial distribution of other (low-lying) Majorana modes. The analysis presented in this chapter focuses only on the *lowest*-lying modes. Although the gaplessness of the disordered system presents no *prima facie* obstacles to the use of these Majorana modes as quantum memory, understanding the occurence of these other low-energy modes is a crucial consideration in addressing Majorana modes in an experimental setting.

Appendix A

Many-body Formalism

A.1 Green's functions

While this thesis does not make extensive use of many-body formalism or Green's function technology, the following elements are required in order to make the discussion self-contained. Relevant references are [7, 10, 103].

The Green's function can best be motivated by considering a gedanken experiment in which an electron is injected into a many-body system. After a time t, we then measure whether the particle remains in this state. This notion may be formalized by introducing electron creation (annihilation) operators $c_k^\dagger$ (c_k) which create (destroy) an electron of momentum k (for the time being, we ignore spin). The *retarded one-particle Green's function* is then defined by

$$G_k^R(t) = -i\Theta(t)\langle\{c_{k\alpha}(t), c_{k'\beta}^\dagger(0)\}\rangle. \tag{A.1}$$

The Heaviside step function Θ plays the crucial role of building causality into the theory. It is also possible to show that G_k^R obeys Schrödinger equation with a delta function source [10]. That this is the case stems from the fact that the $c_k(t)$ obey equal-time anti-commutation relations.

We may express this quantity in terms of its Fourier transform $G^R(t) = \int \frac{d\omega}{2\pi} e^{-i\omega t} G^R(\omega)$. For example, a non-interacting system has

$$G_0^R(\mathbf{k}, \omega) = \frac{1}{\omega - \xi_\mathbf{k} + i\delta}, \tag{A.2}$$

where $\xi = \epsilon_{\mathbf{k}} - \mu$ is the excitation energy above the Fermi sea and $\delta \to 0^+$. Performing an inverse Fourier transform yields $G_0^R(t) = e^{-i\xi_{\mathbf{k}} t}$ for $t > 0$. This is a useful check. We expect that a particle which is never perturbed from a state of energy ξ would evolve with this phase factor. Although the retarded Green's function is the physically relevant quantity, calculations (for example those performed in the path-integral formalism) typically yield *time-ordered* Green's functions which have the form

$$G_0^T(\mathbf{k}, \omega) = \langle T c_k(t) c_{k'}^\dagger(0) \rangle, \tag{A.3}$$

where T is the time-ordered operator defined as

$$T c_A(t_1) c_B(t_2) = \begin{cases} c_A(t_1) c_B(t_2) & \text{if } t_1 > t_2 \\ -c_B(t_2) c_A(t_1) & \text{if } t_2 > t_1. \end{cases} \tag{A.4}$$

For example, the time-ordered Green's function may be obtained by the pole prescription

$$G_0^T(\mathbf{k}, \omega) = \frac{1}{\omega - \xi_{\mathbf{k}} + i \mathrm{sgn}(\omega)\delta}. \tag{A.5}$$

In an interacting system, we expect $G^{R/T}$ to reflect the fact that the electron will now experience fluctuations in energy, or more dramatically, will be scattered out of the state. These effects can be captured by the self-energy Σ, defined implicitly by

$$G^R(\mathbf{k}, \omega) = \frac{1}{\omega - \xi_{\mathbf{k}} + \Sigma_{\mathbf{k}\omega} + i\delta}. \tag{A.6}$$

If $\Sigma_{\mathbf{k}\omega}$ has an imaginary part, this leads to a decay in the real-time Green's function

$$G^R(t, \mathbf{k}) = \int \frac{d\omega}{2\pi} \frac{e^{-i\omega t}}{\omega - \xi + \Sigma_{\mathbf{k}} + i\delta} = \Theta(t) e^{i\tilde{\xi}_{\mathbf{k}}} e^{-\left|\Gamma_{\mathbf{k}\tilde{\xi}_{\mathbf{k}}}\right| t}, \tag{A.7}$$

where $\Gamma_{\mathbf{k}\tilde{\xi}_{\mathbf{k}}} = \text{Im } \Sigma_{\mathbf{k}\tilde{\xi}_{\mathbf{k}}}$ and $\tilde{\xi}_{\mathbf{k}} = \xi_{\mathbf{k}} + \text{Re } \Sigma_{\mathbf{k}}$. Thus, in addition to a finite life, interactions

lead to a renormalization of the energy the state.

A quantity which plays a central role in connecting theory to experiment is the spectral function [10]. Because it obeys precise sum rules, is crucial for understanding how spectral weight is redistributed in an interacting system.

$$A(\mathbf{k},\omega) = -\frac{1}{\pi}\mathrm{Im}G^R(\mathbf{k},\omega) \tag{A.8}$$

For example, for the case of a non-interacting system (Eq. A.2) we have

$$A(\mathbf{k},\omega) = \frac{1}{\pi}\frac{\delta}{(\omega-\xi_{\mathbf{k}})^2+\delta^2}. \tag{A.9}$$

A closely related quantity is the occupation factor $n(k)$ and is given by

$$n(k) = \langle c_{\mathbf{k}} c_{\mathbf{k}}^\dagger \rangle = \int dx e^{-ikx}\, G_R(x, t=0). \tag{A.10}$$

With this formalism in place, we now turn to several examples.

Example: Fermi liquid

An explicit calculation near the Fermi surface, shows that

$$\Sigma_{\mathbf{k}\omega} = (1-1/Z)\,\omega + (\tilde{v}_F/Z - v_F)\,(k-k_F) + i|V_{\mathbf{k}}|^2\xi_{\mathbf{k}}^2, \tag{A.11}$$

where $0 < Z \leq 1$, $\tilde{v}_F$ is the altered form the the Fermi energy [103]. The spectral density now acquires the form

$$A(\mathbf{k},\omega) = \frac{1}{\pi}\frac{\Gamma_{\mathbf{k}\tilde{\xi}_{\mathbf{k}}}}{(\omega-\tilde{\xi}_{\mathbf{k}})^2+(\Gamma_{\mathbf{k}\tilde{\xi}_{\mathbf{k}}})^2}. \tag{A.12}$$

In contrast with the free case, interactions and the resultant finite lifetime give a finite width to the spectral density, reminiscent of the Breit-Wigner form of atomic and particle physics.

For the occupation factor, we have

$$n(k) = Z\Theta(k - k_F) + ..., \tag{A.13}$$

where the ellipsis indicates continuous functions (see [103]).

Example: TLL

For the case of a spinful TLL, an involved diagramtic approach [14] reveals that for intra-branch interactions, the self-energy is of the form

$$\Sigma = \frac{\xi_{\mathbf{k}}^2}{\xi_{\mathbf{k}} - v_F k + i\delta}. \tag{A.14}$$

The pole in Σ is an indication that electrons are extremely unstable in 1D and is intimately related to spin-charge separation (see Chapter 2).

The occupation factor $n(k)$ also signals the breakdown of Fermi liquid theory in 1D. Using the Green's function derived in 2.4 and Eq. A.10, we have

$$n(k) = \frac{1}{2\pi} \int dx \frac{e^{i(k-k_F)x}}{(x - v_F t + i\mathrm{sgn}(t)\delta)^{\frac{1}{2}(g+1/g)}}. \tag{A.15}$$

Power counting reveals that this integral goes as

$$n(k) \propto |k - k_F|^{\frac{1}{2}(g+1/g)-1}. \tag{A.16}$$

In the limit $g \to 1$, we recover the non-interacting case.

A.2 Miscellaneous Useful Identities

A tremendously useful identity which will be used repeatedly is the famous Campbell-Baker-Hausdorff which we use in the form

$$\left[e^{A}, B\right] = [A, B]e^{A} + \frac{1}{2!}[A, [A, B]]e^{A} + \frac{1}{3!}[A, [A, [A, B]]]e^{A} + ... \tag{A.17}$$

This equation may be obtained by Taylor expanding the term e^{A}. A more elegant and efficient derivation is given (as an exercise) in [104].

Appendix B

Correlation Functions

In this section we present a minimal background on field theoretical concepts that are used in this thesis, with a focus on correlation functions.

B.1 Dirac Fermions in 1D

B.1.1 Massive Case

In field theory, it is standard to begin with a Lagrangian. The Dirac Lagrangian (density) is given by

$$\mathcal{L} = \overline{\Psi}\left(i\gamma^{\mu}\partial_{\mu} - m\right)\Psi. \tag{B.1}$$

The Dirac spinor Ψ annihilates an electron at x, t and obeys the anticommutation relations

$$\left\{\Psi^{\dagger}(x,t), \Psi(x',t)\right\} = \delta(x - x') \tag{B.2}$$

Written in terms of its components,

$$\Psi = \begin{pmatrix} \psi_R \\ \psi_L \end{pmatrix}. \tag{B.3}$$

A standard representation of the γ matrices in $1+1$ dimensions is ([9])

$$\gamma^0 = \sigma^x \text{ and } \gamma^1 = \sigma^y, \tag{B.4}$$

where 0 is rescaled Matsubara time ($\tau = iv_F t$), 1 is space (x). As usual, $\overline{\Psi} = \Psi^\dagger \gamma^0$. The quantity $\overline{\Psi}\gamma^0\Psi = \rho = \sum_{r=\pm} \rho_r$ is the sum of charge densities $\rho_r = \psi_r^\dagger \psi_r$, and $j = -i\overline{\Psi}\gamma^1\Psi = \sum_r r\rho_r$.

Explicitly, the Dirac action has the form

$$\begin{aligned} S_D &= \int dtdx\ \mathcal{L} \\ &= \int dtdx\ \overline{\Psi}\left(i\partial_\tau \sigma^x + \partial_x \sigma^y - m\right)\Psi \\ &= \int d\tau dx\ (\psi_R\ \psi_L) \begin{pmatrix} -2\partial_z & -m \\ -m & 2\partial_{\bar{z}} \end{pmatrix} \begin{pmatrix} \psi_R \\ \psi_L \end{pmatrix}, \end{aligned} \tag{B.5}$$

where we have introduced the complex coordinates $z = x + iv_F t$ (we will also use $z = (x, v_F t)$). Sensibly, we have that $\partial_z z = 1$ and $\partial_{\bar{z}} \bar{z} = 1$.

An important quantity are the correlation functions, of the fermion fields. For example, the time-ordered Green's function is given by

$$G^T_{rr'}(z_1, z_2) = \langle 0 | T\psi_r(z_1)\psi^\dagger_{r'}(z_2)|0\rangle. \tag{B.6}$$

Other quantities of interest are the retarded and advanced Green's function. These quantities are easily calculated using path integrals [23]. In order to motivate the result, consider the following expectation value

$$\langle u_i^* u_j \rangle = \frac{\int \left(\prod_i \frac{du_i\ du_i^*}{2\pi i}\right) u_i^* u_j e^{-\sum_{ij} u_i^* A_{ij} u_j}}{\int \left(\prod_i \frac{du_i\ du_i^*}{2i\pi}\right) e^{-\sum_{ij} u_i^* A_{ij} u_j}} = A^{-1}_{ij}, \tag{B.7}$$

where the u_i are real-valued functions [8]. Although there are many subtleties in formulating a fermionic coherent state path integral, the resultant expectation values are analogous to A^{-1}_{ij}: they are given by the 'inverse' of the 'matrix element' linking $\psi_r(z_1)$ to $\psi^\dagger_{r'}(z_2)$ in the

action S. Given the translational invariance of Eq. B.1, we go to Fourier space:

$$\psi_r(k) = \int_{-\infty}^{\infty} \psi_r(x) e^{-ikx} dx. \tag{B.8}$$

Letting, $z = (t, x)$ and $k = (k_t, k_x)$, we have (setting v_F back to 1)

$$\begin{aligned} G_{rr'}(z_1, z_2) &= \int \frac{d^2k}{(2\pi)^2} \frac{e^{ik\cdot z}}{k_\mu \gamma^\mu - m} && \text{(B.9)} \\ &= \int \frac{d^2k}{(2\pi)^2} e^{ik\cdot z} \begin{pmatrix} -k_t + ik_x & -m \\ -m & -k_t - ik_x \end{pmatrix}^{-1} && \text{(B.10)} \\ &= \int \frac{d^2k}{(2\pi)^2} \frac{e^{ik\cdot z}}{k_t^2 + k_x^2 + m^2} \begin{pmatrix} m & ik_t - k_x \\ ik_t + k_x & m \end{pmatrix}. && \text{(B.11)} \end{aligned}$$

The resultant integral may be expressed in terms of the zeroth Bessel function of imaginary argument

$$K_0(m|x|) = \int \frac{d^2k}{(2\pi)^2} \frac{e^{ik\cdot x}}{k_t^2 + k_x^2 + m^2}. \tag{B.12}$$

From Eq. B.11, we obtain

$$G_{rr'}(z_1, z_2) = -\frac{1}{2\pi} \begin{pmatrix} -m & 2\partial_z \\ 2\partial_{\bar{z}} & -m \end{pmatrix} K_0(|m||z_{12}|), \tag{B.13}$$

where $z_{12} = z_1 - z_2$ and $|z| = \sqrt{z\bar{z}}$ [15].

Finally, it is useful to give the Hamiltonian corresponding to Eq. B.1. The conjugate momentum to Ψ is

$$\Pi_\Psi = \frac{\partial \mathcal{L}}{\partial (\partial_t \Psi)} = i\overline{\Psi}\gamma^0 = i\Psi^\dagger \tag{B.14}$$

Using the definition of the Hamiltonian density

$$\mathcal{H} = \Pi_\Psi \partial_t \Psi - \mathcal{L}, \tag{B.15}$$

we get

$$
\begin{aligned}
H &= \Psi^\dagger \partial_t \Psi - \mathcal{L} && \text{(B.16)} \\
&= \int dx \overline{\Psi} \begin{pmatrix} -iv_F\partial_x & m \\ m & iv_F\partial_x \end{pmatrix} \Psi && \text{(B.17)} \\
&= \int dx \left[-iv_F \left(\psi_R^\dagger \partial_x \psi_R - \psi_L^\dagger \partial_x \psi_L \right) + m \left(\psi_L^\dagger \psi_R + \psi_R^\dagger \psi_L \right) \right].
\end{aligned}
$$

B.1.2 Massless case

Of central importance in our work here will be the massless limit. Employing the expansion $K_0(z) \sim -\ln z$ valid for $z \ll 1$ [27], Eq. B.13 becomes

$$
G_{rr'}(z_1, z_2) = \frac{1}{2\pi} \begin{pmatrix} 0 & 1/z_{12} \\ 1/\bar{z}_{12} & 0 \end{pmatrix}. \tag{B.18}
$$

For example, we have that

$$
\langle \psi_R(z_2) \psi_R^\dagger(z_1) \rangle = \frac{1}{2\pi z_{12}}. \tag{B.19}
$$

This quantity has dimensions of an inverse length, as is to be expected given that the action of Eq. B.6 is dimensionless. This correlation function plays a crucial role in linking TLL theory to its experimental prediction.

It is instructive to check that $1/2\pi\bar{z}$ is indeed the Green's of the operator ∂_z. First, we note that for $z \neq 0$, we have (setting $v_F = 1$)

$$
\partial_z \left(\frac{1}{\bar{z}} \right) = \frac{1}{2} \left(\partial_x - i\partial_t \right) \left(\frac{1}{x - it} \right) = 0. \tag{B.20}
$$

However, we also have that for any region A

$$\int\int_A dxdy\ \partial_z\left(\frac{1}{\bar{z}}\right) = -\frac{i}{2}\oint_{\partial A}\frac{dz}{z} = \begin{cases}\pi & \text{if } \partial\text{A encloses the origin,}\\ 0 & \text{otherwise.}\end{cases}$$

This follows from Stokes' and Cauchy's theorems [9]. Putting these two results together, we have

$$\partial_z\left(\frac{1}{\bar{z}}\right) = 2\pi\delta^2(x,y). \tag{B.21}$$

Thus, $1/2\pi\bar{z}$ is the Green's function of the operator ∂_z.

B.2 Bosons in 1+1 dimensions

The key to the method of bosonization is to express fermionic operators in terms of bosonic operators. It will be seen that correlation functions which are hard in one language become easy in another. For comparison, it is thus helpful to consider the massive bosonic theory given by

$$S_B = \frac{1}{2}\int dtdx\left[(\partial_t\theta)^2 - (\partial_x\theta)^2 - m\theta^2\right] \tag{B.22}$$

where $r = \pm$ refers to right- and left-movers, respectively. We see that the propagator will have the same form as Eq. B.11. Indeed, we find the correlation function

$$\langle\theta(z_2)\theta(z_1)\rangle = \frac{1}{\pi}K_0\left(m|z_{12}|\right). \tag{B.23}$$

The massless limit of Eq. B.23 may be obtained from the asymptotic expression for $K_0(z)$ given above and is given by

$$\langle\theta(z_2)\theta(z_1)\rangle = \frac{1}{2\pi}\ln\left(|z_{12}|^2 + a^2\right), \tag{B.24}$$

where we have regularized the theory with a small distance cutoff a. This result is familiar from 2D electrostatics.

Finally, we derive the Hamiltonian corresponding to Eq. B.22. By definition,

$$\Pi_\theta = \frac{\partial \mathcal{L}}{\partial(\partial_t \theta)} = \partial_t \theta. \tag{B.25}$$

Hence,

$$\begin{aligned} H_B &= \int dx \ (\Pi_\theta \partial_t \theta - \mathcal{L}) \\ &= \frac{1}{2} \int dx \left[(\partial_t \theta)^2 + (\partial_x \theta)^2 + m^2 \theta^2 \right]. \end{aligned} \tag{B.26}$$

Appendix C

Details of band structure calculation for SWNT in transverse fields

In the absence of any fields, the eigenstates of an infinitely long armchair nanotube are superpositions of the states $|\Phi^{\ell}_{A/B}\rangle$ defined in Chapter 3. For the particular case of an armchair nanotube we have

$$\begin{aligned} \langle \Phi^{\ell'}_A | H | \Phi^{\ell}_B \rangle &= -\frac{t}{2n} \sum_{\vec{R}\in B, \vec{R}'\in A} e^{i(k\cdot R - k'\cdot R') + \frac{ie}{\hbar}(G_R - G'_R)} \\ &= -\frac{t}{N} \sum_s e^{i2\pi \frac{(\ell-\ell')s}{L}} \left(e^{\frac{i2\pi\ell a}{\sqrt{3}L}} + F(k_y, s) \right). \end{aligned} \tag{C.1}$$

where

$$F(k_y, s) = 2e^{-\frac{i2\pi\ell a}{2\sqrt{3}L}} \cos\left(\frac{k_y a}{2} + \sqrt{3} B \frac{|e|}{\hbar} \left(\frac{L}{2\pi} \right)^2 \left[\cos\frac{2\pi}{L} s - \cos\frac{2\pi}{L}\left(s - \frac{a}{2\sqrt{3}} \right) \right] \right), \tag{C.2}$$

and $b = \frac{\sqrt{3}B|e|L^2}{4\pi^2\hbar}$. For small magnetic fields ($b \ll 1$) we have

$$\langle \Phi^{\ell'}_A | H_B | \Phi^{\ell}_B \rangle = tb \sin\frac{ka}{2} e^{\frac{i\pi\ell}{3n}} \left(1 - e^{\pm\frac{i\pi}{3n}} \right), \tag{C.3}$$

for $\ell - \ell' = \pm 1 \bmod n$ and

$$\langle \Phi^{0}_A | H_B | \Phi^{0}_B \rangle = tb^2 \cos\frac{ka}{2} \left(1 - \cos\frac{\pi}{3n} \right). \tag{C.4}$$

For the gapless case, the low energy spectrum near half-filling is

$$\epsilon_{r\alpha}(k) = \hbar r \tilde{v}_{F,r}\left(k - \alpha\tilde{k}_F\right) + \alpha t\Delta s + \mathcal{O}(k^2), \tag{C.5}$$

The renormalized Fermi velocity is given by

$$v_r = v_F\left(1 - \Delta v_1 b^2 - \Delta v_2 U_y^2 \pm \Delta v_3 b U_y\right), \tag{C.6a}$$

where

$$\Delta v_1 = \frac{5 + 4\cos\frac{\pi}{n}}{3\left(1 + 2\cos\frac{\pi}{3n}\right)^2}, \tag{C.6b}$$

$$\Delta v_2 = \frac{3 + \cos\frac{\pi}{3n} + 2\cos\frac{2\pi}{3n}}{12\left(1 - \cos\frac{\pi}{n}\right)} \tag{C.6c}$$

$$\Delta v_3 = \frac{\left(\cos\frac{\pi}{6n} + \cos\frac{5\pi}{6n}\right)\csc\frac{\pi}{6n}}{\sqrt{3}\left(1 + 2\cos\frac{\pi}{3n}\right)^2}. \tag{C.6d}$$

and

$$\tilde{k}_F = \left[\frac{4\pi}{3a} + \frac{U_y^2}{2\sqrt{3}\left(1 + 2\cos\frac{\pi}{3n}\right)} + \frac{8}{\sqrt{3}}\sin^2\left(\frac{\pi}{6n}\right)b^2\right] \tag{C.7}$$

The shift between the two Fermi points (see Eq. (10)) is given by

$$\Delta s = \frac{\sqrt{3}\sin\frac{\pi}{3n}}{1 + 2\cos\frac{\pi}{3n}} b U_y. \tag{C.8}$$

For the case of mutually perpendicular fields discussed in section 3.4.3, the electronic densities are given by the vector

$$\rho_{r\alpha}(s) = \frac{1}{2}\begin{pmatrix} 1 + g_1 r u\cos\left(\frac{s}{R} + \frac{\pi}{6n}\right) - g_2 b\alpha\cos\left(\frac{s}{R} + \frac{\pi}{3n}\right) \\ 1 - g_1 r u\cos\left(\frac{s}{R} - \frac{\pi}{6n}\right) + g_2 b\alpha\cos\left(\frac{s}{R} - \frac{\pi}{3n}\right) \end{pmatrix}, \tag{C.9}$$

where the upper and lower components are the electronic densities over the A and B sub-

lattices respectively. The constants g_1 and g_2 are given by

$$g_1 = \frac{1}{2}\csc\frac{\pi}{2n} \tag{C.10}$$

$$g_2 = \sqrt{3}\csc\frac{\pi}{2n}. \tag{C.11}$$

C.1 Interaction terms

In order to find the form of the effective interaction $V^{rr'}_{\alpha\alpha'}$ we need account for not only the radial dependence of the wave functions but also for the physical separation between the sublattices. Although the factorization performed in Eq. 4.1 is an approximation, we may still account for the physical separation of the sublattices. We follow the approach introduced in [57]. Let

$$V^{rr'}_{\alpha\alpha'}(x-x') = \int_0^{2\pi R}\int_0^{2\pi R}\frac{ds\ ds'}{(2\pi R)^2}\rho^T_{r\alpha}(s)\begin{pmatrix} U(0) & U(a_c) \\ U(-a_c) & U(0)\end{pmatrix}\rho_{r'\alpha'}(s'),$$

where $U(d)$ is a shorthand for the Coulomb interaction with an offset d, that is

$$U(d) = U(x-x', s-s'+d) \tag{C.12}$$

where the right hand side of this equation is given by Eq (4.5). The constant c_0 which appears in Eq. (4.13) is given by

$$c_0(n) = -\gamma - \frac{1}{4\pi}\int_0^{2\pi} d\varphi\ \ln\left[\cos^2\frac{\varphi}{2} + \left(\frac{\pi}{\sqrt{3}n}\right)^2\right].$$

Similarly we find that the values of h_1 and h_2 defined in section 3 are given by

$$h_1(n) = \left(c_2^2 - c_1^2\right) f_1(n) + 2c_1c_2 f_2(n) + 2\left(c_1^2 + c_2^2\right) f_3(n),$$

$$h_2(n) = \left(c_4^2 - c_3^2\right) f_1(n) + 2c_3c_4 f_2(n) + 2\left(c_3^2 + c_4^2\right) f_3(n),$$

and

$$h_3(n) = 2[(c_1c_3 + c_2c_4)\, f_1(n) + (c_1c_4 + c_2c_3)\, f_2(n) + 2(c_1c_3 + c_2c_4) f_3(n)],$$

where

$$f_1(n) = \int_{-\pi R}^{\pi R} \frac{dz}{2\pi R} \left\{ \ln \left[\cos^2 \frac{z - a_c}{2R} + \left(\frac{a_z}{2R}\right)^2 \right] + \ln \left[\cos^2 \frac{z + a_c}{2R} + \left(\frac{a_z}{2R}\right)^2 \right] \right\} \cos \frac{z}{R},$$

$$f_2(n) = \int_{-\pi R}^{\pi R} \frac{dz}{2\pi R} \left\{ \ln \left[\cos^2 \frac{z - a_c}{2R} + \left(\frac{a_z}{2R}\right)^2 \right] - \ln \left[\cos^2 \frac{z + a_c}{2R} + \left(\frac{a_z}{2R}\right)^2 \right] \right\} \sin \frac{z}{R},$$

$$f_3(n) = \int_{-\pi R}^{\pi R} \frac{dz}{2\pi R} \ln \left[\cos^2 \frac{z}{2R} + \left(\frac{a_z}{2R}\right)^2 \right]$$

and

$$\begin{aligned}
c_1 &= \frac{1}{2} \csc \frac{\pi}{2n} \cos \frac{\pi}{6n} \\
c_2 &= \frac{1}{2} \csc \frac{\pi}{2n} \sin \frac{\pi}{6n} \\
c_3 &= \sqrt{3} \csc \frac{\pi}{2n} \sin \frac{\pi}{6n} \cos \frac{\pi}{3n} \\
c_4 &= \sqrt{3} \csc \frac{\pi}{2n} \sin \frac{\pi}{6n} \sin \frac{\pi}{3n}.
\end{aligned}$$

The values of c_0, h_1, h_2 and h_3 have been tabulated for various tube sizes and are displayed below.

Finally, we obtain Eq. 4.13 assuming equal charge densities over the two sublattices

Table C.1: Values of c_0, h_1, h_2 and h_3.

n	c_0	h_1	h_2	h_3
15	-0.005	0.786	0.020	17.417
20	0.025	0.834	0.122	24.605
25	0.043	0.865	0.008	31.855
40	0.071	0.913	0.003	53.751
60	0.086	0.941	0.002	83.066

giving an averaged

$$V(x-x') = \int_0^{2\pi R} dy \int_0^{2\pi R} dy' \; \frac{1}{4}(2U(x-x', s-s') \;+\; U(x-x', s-s'+d) \\ +\; U(x-x', s-s'-d)). \quad \text{(C.13)}$$

Now, letting

$$\begin{aligned} V(x-x') &= \frac{e^2}{(2\pi R)^2 \kappa} \int_0^{2\pi R} dy \int_0^{2\pi R} dy' \; U(x-x', y-y') \qquad \text{(C.14)} \\ &= \frac{e^2}{(2\pi R)^2 \kappa} \left[\int_{-2\pi R}^{0} dr \int_{-r/2}^{r/2+2\pi R} dY + \int_0^{2\pi R} dr \int_{r/2}^{2\pi R - r/2} dY \right] U(r, Y), \end{aligned}$$

where the change of variables is given by $y = Y + r/2$ and $y' = Y - r/2$. Taking the Fourier transform of this equation gives (in the long wavelength limit $kR \ll 1$) Eq. 4.13.

References

[1] Thouless, D. J., Kohmoto, M., Nightingale, M. P., and den Nijs, M. *Phys. Rev. Lett.* **49**, 405–408 Aug (1982).

[2] Hasan, M. Z. and Kane, C. L. *Rev. Mod. Phys.* **82**, 3045–3067 Nov (2010).

[3] Nayak, C., Simon, S. H., Stern, A., Freedman, M., and Sarma, S. D. *Rev. Mod. Phys.* **80**, 1083 (2008).

[4] Lutchyn, R. M., Sau, J. D., and Das Sarma, S. *Phys. Rev. Lett.* **105**, 077001 Aug (2010).

[5] Reich, E. S. *Nature* **483**, 132 (2012).

[6] Anderson, P. W. *Phys. Rev.* **109**, 1492–1505 Mar (1958).

[7] Pines, D. *The Many-Body Problem.* Addison Wesley Longman, (1961).

[8] Giamarchi, T. *Quantum Physics in One Dimension.* Oxford Science Publications, (2004).

[9] Stone, M. *Bosonization.* World Scientific, (1994).

[10] Phillips, P. *Advanced Solid State Physics.* Cambridge University Press, (2012).

[11] Huang, K. *Statistical Mechanics.* John Wiley and Sons, (1963).

[12] Shankar, R. *Rev. Mod. Phys.* **66**, 129–192 Jan (1994).

[13] Ashcroft, N. W. and Mermin, N. D. *Solid State Physcis.* Harcourt, (1976).

[14] Maslov, D. L. In *Lecture notes for the LXXXI Les Houches Summer School "Nanoscopic Quantum Transport"*, (2004).

[15] Gogolin, A. O., Nersesyan, A. A., and Tsvelik, A. M. *Bosonization and Strongly Correlated Systems.* Cambridge University Press, (1998).

[16] Kane, C. L. and Fisher, M. P. A. *Phys. Rev. Lett.* **68**, 1220 (1992).

[17] Hou, C.-Y., Kim, E.-A., and Chamon, C. *Phys. Rev. Lett.* **102**, 076602 Feb (2009).

[18] Kollath, C., Schollwöck, U., and Zwerger, W. *Phys. Rev. Lett.* **95**, 176401 Oct (2005).

[19] Angelakis, D. G., Huo, M., Kyoseva, E., and Kwek, L. C. *Phys. Rev. Lett.* **106**, 153601 Apr (2011).

[20] Yao, Z., Postma, H. W. C., Balents, L., and Dekker, C. *Nature* **402**, 273 (1999).

[21] Braunecker, B., Bena, C., and Simon, P. *Phys. Rev. B* **85**, 035136 Jan (2012).

[22] Braunecker, B., Simon, P., and Loss, D. *Phys. Rev. Lett.* **102**, 116403 Mar (2009).

[23] Atland, A. and Simons, B. *Condensed Matter Field Theory*. Cambridge, (2006).

[24] Ferry, D. K. and Goodnick, S. M. *Transport in Nanostructures*. Cambridge University Press, (1997).

[25] Kinaret, Jonson, Shekhter, and Eggert. *Phys. Rev. B* **57**, 3777–81 (1998).

[26] Aigner, M. and Ziegler, G. M. *Proofs from the Book*. Springer-Verlag, Berlin, (2003).

[27] Abromowitz, M. and Stegun, I. A., editors. *Handbook of Mathematical Functions with Formulas, Graphs, and Mathematical Tables*. National Bureau of Standards Applied Mathematics Series, (1964).

[28] Steinberg, H., Barak, G., Yacoby, A., Pfeiffer, L. N., West, K. W., Halperin, B. I., and Hur, K. L. *Nature Physics* **4**, 116 (2008).

[29] Blumenstein, C., Schfer, J., Mietke, S., Meyer, S., Dollinger, A., Lochner, M., Cui, X. Y., Patthey, L., Matzdorf, R., and Claessen, R. *Nature Physics* **7**, 776–780 (2011).

[30] Kim, C., Shen, Z.-X., Motoyama, N., Eisaki, H., Uchida, S., Tohyama, T., and Maekawa, S. *Phys. Rev. B* **56**, 15589–15595 Dec (1997).

[31] Grayson, M., Tsui, D. C., Pfeiffer, L. N., West, K. W., and Chang, A. M. *Phys. Rev. Lett.* **80**, 1062–1065 Feb (1998).

[32] Auslaender, O., Yacoby, A., de Picciotto, R., Baldwin, K. W., Pfeiffer, L. N., and West, K. W. *Science* **295**, 825 (2002).

[33] Saito, S., Dresselhaus, M., and Dresselhaus, G. *Phys. Rev. B* **50**, 14698 (1994).

[34] Iijima, S. *Nature* **354**, 56 (1991).

[35] Ajiki, H. and Ando, T. *J. Phys. Soc. Japan* **62**, 1255 (1993).

[36] Novikov, D. S. and Levitov, L. S. *Phys. Rev. Lett.* **68**, 155402 (2003).

[37] Lee, H.-W. and Novikov, D. S. *Phys. Rev. B* **68**, 155402 (2003).

[38] Bellucci, S. and Onorato, P. *Eur. Phys. J. B* **47**, 385 (2005).

[39] Bellucci, S. and Onorato, P. *Eur. Phys. J. B* **52**, 469 (2006).

[40] Castro Neto, A. H., Guinea, F., Peres, N. M. R., Novoselov, K. S., and Geim, A. K. *Rev. Mod. Phys.* **81**, 109–162 Jan (2009).

[41] Feynman, R. P., Leighton, R. B., and Sands, M. *The Feynman Lectures on Physics Vol. II.* Addison Wesley, (1964).

[42] Saito, S., Dresselhaus, M., and Dresselhaus, G. *Physical Properties of Carbon Nanotubes.* Imperial College Press, (1998).

[43] Sachdev, S. *Quantum Phase Transitions.* Cambridge University Press, (2011).

[44] Winkler, R. *Spin-orbit Coupling Effects in Two-Dimensional Electron and Hole Systems.* Springer-Verlag, Berlin, (2010).

[45] Cheung, C. L., Kurtz, A., Park, H., and Lieber, C. M. *J. Phys. Chem. B* **106**, 2429 (2002).

[46] Stone, M. and Chung, S.-B. *Phys. Rev. B* **73**, 014505 (2006).

[47] Fernandez, V. I. PhD thesis, Universidad Nacional de La Plata, (2002).

[48] Fernandez, V., Iucci, A., and Naon, C. *Eur. Phys. J. B* **30**, 53–56 (2002).

[49] McCann, E. and Fal'ko, V. *J. Phys. Cond. Matt.* **16**, 2371 (2004).

[50] Liang, W., Bockrath, M., and Park, H. *Phys. Rev. Lett.* **88**, 126801 (2002).

[51] Makarovski, A., An, L., Liu, J., and Finkelstein, G. *Phys. Rev. B* **74**, 155431 (2006).

[52] Oreg, Y., Byczuk, K., and Halperin, B. *Phys. Rev. Lett.* **85**, 365 (2000).

[53] Srivastava, D., Menon, M., and Cho, K. *Computing in Science and Engineering* **3**, 42–55 (2001).

[54] Odom, T. W., Huang, J.-L., Cheung, C. L., and Leiber, C. M. *Science* **290**, 1549 (2008).

[55] Deshpande, V. V., Chandra, B., Caldwell, R., Novikov, D. S., Hone, J., and Bockrath, M. *Science* **323**, 106 (2009).

[56] Mason, N. private communication.

[57] Egger, R. and Gogolin, A. O. *Phys. J. B.* **3**, 281 (1998).

[58] Misner, C., Thorne, K., and Wheeler, J. *Gravitation.* W. H. Freeman, (1973).

[59] Postma, H. W. C., de Jonge, M., Yao, Z., and Dekker, C. *Phys. Rev. B* **62**, 653 (2000).

[60] Kane, C., Balents, L., and Fisher, M. P. A. *Phys. Rev. Lett.* **79**, 5086 (1999).

[61] Fabrizio, M. and Gogolin, A. O. *Phys. Rev. B* **51**, 17827 (1995).

[62] Eggert, S., Johannesson, H., and Mattsson, A. *Phys. Rev. Lett.* **76**, 1505 (1996).

[63] DeGottard, W., Wei, T.-C., and Visheshwara, S. *Phys. Rev. B* **79**, 205421 May (2009).

[64] Su, W. P., Schrieffer, J. R., and Heeger, A. J. *Phys. Rev. B* **22**, 2099–2111 Aug (1980).

[65] Safi, I. and Schulz, H. J. *Phys. Rev. B* **52**, R14265–R14268 (1996).

[66] Pham, K.-V., Gabay, M., and Lederer, P. *Phys. Rev. B* **61**, 16397 (2000).

[67] Pugnetti, S., Dolcini, F., Bercioux, D., and Grabert, H. *Phys. Rev. B* **79**, 035121 Jan (2009).

[68] Averin, D. V. *Physica C* **352**, 120–124 (2001).

[69] Hur, K. L., Halperin, B., and Yacoby, A. *Ann. Phys. (N.Y.)* **323**, 3037 (2008).

[70] Nazarov, Y. V. and Blanter, Y. M. *Quantum Transport*. Cambridge University Press, (2009).

[71] Leinaas, J. M., Horsdal, M., and Hansson, T. H. *arXiv:0906.0811v2* .

[72] Castro-Neto, A. H., de C. Chamon, C., and Nayak, C. *Phys. Rev. Lett.* **79**, 4729–4733 (1997).

[73] Kitaev, A. *arXiv:cond-mat/0010440v2* (2000).

[74] Feng, X.-Y., Zhang, G.-M., and Xiang, T. *Phys. Rev. Lett.* **98**, 087204 (2007).

[75] Chen, H.-D. and Hu, J. *Phys. Rev. B* **76**, 193101 (2007).

[76] Lieb, E., Schultz, T., and Mattis, D. *Ann. Phys. (N.Y.)* **16**, 407 (1961).

[77] Barouch, E., McCoy, B. M., and Dresden, M. *Phys. Rev. A* **2**, 1075 (1970).

[78] Bunder, J. E. and McKenzie, R. H. *Phys. Rev. B* **60**, 344 (1999).

[79] Kogut, J. B. *Rev. Mod. Phys.* **51**, 659 (1979).

[80] Kitaev, A. *Ann. Phys. (N.Y.)* **321**, 2 (2006).

[81] Baskaran, G., Mandal, S., and Shankar, R. *Phys. Rev. Lett.* **99**, 196805 (2007).

[82] Yao, H. and Kivelson, S. A. *Phys. Rev. Lett.* **99**, 247203 (2007).

[83] Chen, H.-D. and Nussinov, Z. *J. Phys. A* **41**, 075001 (2008).

[84] Nussinov, Z. and Ortiz, G. *Phys. Rev. B* **77**, 064302 (2008).

[85] Schmidt, K. P., Dusuel, S., and Vidal, J. *Phys. Rev. Lett.* **100**, 057208 (2008).

[86] Ivanov, D. A. *Phys. Rev. Lett.* **86**, 268 (2001).

[87] Kells, G., Bolukbasi, A. T., Lahtinen, V., Slingerland, J. K., Pachos, J. K., and Vala, J. *Phys. Rev. Lett.* **101**, 240404 (2008).

[88] Wen, X.-G. and Zee, A. *Nucl. Phys. B* **316**, 641 (1989).

[89] Wimmer, M., Akhmerov, A. R., Medvedyeva, M. V., Tworzydlo, J., and Beenakker, C. W. J. *Phys. Rev. Lett.* **105**, 046803 (2010).

[90] Ostlund, S. and Pandit, R. *Phys. Rev. B* **29**, 1394 (1984).

[91] Sen, D. and Lal, S. *Europhys. Lett.* **52**, 337 (2000).

[92] Teo, J. C. Y. and Kane, C. L. *Phys. Rev. B* **82**, 115120 (2012).

[93] Simon, B. *Phys. Rev. Lett.* **51**, 2167–2170 Dec (1983).

[94] Jackiw, R. and Rebbi, C. *J. Phys. A* **1387**, 3398 (1976).

[95] Motrunich, O., Damle, K., and Huse, D. A. *Phys. Rev. B* **63**, 224204 (2001).

[96] Bouwer, P. W., Duckheim, M., Romita, A., and von Oppen, F. *arXiv:1103.27646v2* (2012).

[97] Shivamoggi, V., Refael, G., and Moore, J. E. *arXiv:1004.4585* , check ((2010)).

[98] Hofstadter, D. R. *Phys. Rev. B* **14**, 2239–2249 (1976).

[99] Izrailev, F. M., Krokhin, A. A., and Makarov, N. M. *arXiv:1110.1762v1* (2011).

[100] Thouless, D. J. *J. Phys. C:Solid State Phys.* **5**, 77 (1972).

[101] Lloyd, P. *J. Phys. C: Solid St. Phys.* **2**, 1717 (1969).

[102] Reed, M. and Simon, B. *Methods of Modern Mathematical Physics IV: Analysis of Operators*. Academic Press, (1978).

[103] Abrikosov, A. A., Gorkov, L. P., and Dzyaloshinski, I. E. *Methods of Quantum Field Theory in Statistical Physics*. Dover, (1963).

[104] Greiner, W. and Reinhardt, J. *Field Quantization*. Springer, (1996).